

Experimental demonstration of quantum effects in the operation of microscopic heat engines



James Klatzow
St Cross
University of Oxford

A thesis submitted for the degree of
Doctor of Philosophy
Trinity 2018

To my parents.

Abstract

This thesis is an account of experimental investigations into quantum effects in the operation of heat engines on the atomic scale. It begins with a description and justification for the idea of implementing a heat engine using the negative nitrogen vacancy centre in diamond. Following this, the development and final version of the experimental setup and processes are described. Theoretical results extending the idealised theory of quantum heat engines to account for experimental conditions are derived, along with results relating to the limit cycles of cyclic quantum heat engines. Finally the central results of the thesis, showing the experimental existence of quantum thermodynamic signatures in the operation of microscopic heat engines, are presented.

Acknowledgements

I cannot but begin by acknowledging the huge debt of gratitude I owe to my parents, Shelona and David, and sister Cathryn, for their unwavering support over the years; undertaking a doctorate would have been inconceivable without the upbringing and encouragement I received from them. In particular, I can clearly trace the origin of my interest in science to the many hours spent conducting experiments with my father during my formative years, and my continued learning from him ever since.

Next I would like to thank my supervisors Prof. Ian Walmsley, Dr. Josh Nunn, and Dr Patrick Ledingham for the guidance and help provided throughout this DPhil – I have the distinction of having had three supervisors during my time here, each with their own unique style of supervision, each of which I have benefited from greatly. Every bit as important was the input from my postdocs: Dr Eilon Poem, who originally conceived the project and has been actively involved throughout, despite returning to Israel part way through; Dr Dylan Saunders (who has since departed for sunnier climes) and Dr Patrick Ledingham (prior to supervisor status) who both gave frequent and substantial help and advice to a theoretist woefully out of his depth in a quantum optics lab; and finally, and more recently, Dr Jonas Becker, who brought his immense knowledge of diamond physics and contributed to an extent quite out of proportion to the his time involved in the project.

I was very fortunate to be provided funding by the Commonwealth Scholarship Commission, which allowed me to undertake close to 4 years of dedicated study, for which I am very grateful.

Contents

1	Introduction	7
1.1	Motivation	7
2	Background Theory	16
2.1	Quantum Thermodynamics	16
2.1.1	Dynamical Quantum Thermodynamics	17
2.1.2	Liouville space	21
2.1.3	First Law	22
2.1.4	Entropy and the Second Law	24
2.1.5	Dynamical analysis of Quantum Heat Engines	26
2.1.6	Quantum Thermodynamic Signatures	35
2.1.7	Equivalence of quantum heat machines	41
2.2	The Nitrogen Vacancy Centre in Diamond	44
2.2.1	Introduction to the NV centre	46
2.2.2	Electronic structure	47
2.2.3	Ground state fine structure	49
2.2.4	Excited state fine structure	51
2.2.5	Optical Dynamics	53

2.2.6	Optical spin pumping	56
2.2.7	Optically detected magnetic resonance	58
2.2.8	Optical dynamics in a magnetic field	60
2.2.9	Ground state spin dynamics of the NV centre	62
3	Experiment	64
3.1	Heat Engines with NV centres	64
3.2	Emulation of the thermal action	65
3.3	Converting Fluorescence Change into Power	79
3.4	Putting it together	83
3.5	Experimental setup	85
3.5.1	Diamond sample preparation	85
3.5.2	Microwave Waveguide	85
3.5.3	Setup	89
3.5.4	Spectroscopy	94
3.5.5	Thermalisation	101
4	Results	107
4.1	Theory results	107
4.1.1	Inhomogeneous broadening	107
4.1.2	Homogeneous dephasing	118
4.1.3	Theoretical predictions	122
4.2	Experimental Results	126
4.2.1	Stochastic Bound	126
4.2.2	Equivalence	127
4.2.3	Dephasing	130
4.2.4	Error analysis	132

5	Limit Cycles in Quantum Heat Engines	133
6	Conclusion	145
6.1	Summary	145
6.2	Outlook	146
	Bibliography	149

Chapter 1

Introduction

1.1 Motivation

As we go about our daily lives, we are surrounded by countless thermodynamic processes. These happen to govern much our existence, whether it be through the warming effect of the sun which sustains all life on earth, or the ever continuing, and losing, fight against entropy, which will result in everything between ones tea going cold and the ultimate heat death of the universe. Much of our modern industrialised world is driven by our ability to harness and control thermodynamic processes, including the mundane steam turbine in a power station, or more spectacularly, the Flying Scotsman thundering past in a cloud of steam and smoke, or the roar of a Rolls-Royce Merlin in a Spitfire. All of these processes, and far more, are governed and understood through the laws of thermodynamics, which has proved to be one of the most successful and enduring of the classical physical theories, surviving two revolutions in physics at the beginning of the 20th century.

One of these revolutions was the beginning of the Quantum era of physics, ushered in by Max Planck, who presented what subsequently became known as the Planck postulate in 1900. The half a century that followed was a period of rapid progress, in

which many of the ideas and foundations of quantum mechanics were thrashed out and formalised. Once a better understanding of quantum mechanics had been gained, it was applied to gain greater understanding in other subject areas, and even lead to the establishment of completely new subjects. These include anything from the development of physical chemistry and condensed matter physics, to quantum computing and metrology. During the last three decades there has been a boom in subjects such as quantum computing [1], which seek to exploit the unusual properties of quantum mechanics for technological advantage; in addition to quantum computation, this includes the related areas of quantum information theory, quantum communications, quantum cryptography [2], quantum metrology [3] and quantum simulations [4]. The thread commonly linking these various topics is that they consist of the amalgamation of a pre-existing field with quantum mechanics, often with the hope that interesting new phenomena may arise, and that quantum properties such as superposition and entanglement can be utilised to provide enhanced new technological capabilities.

Although thermodynamics played a pivotal role in the initial development of quantum mechanics, the field itself had been left largely untouched by the advances in quantum physics. The emergence of quantum thermodynamics as a field in its own right is a comparatively recent development [5, 6]. Its study is concerned with determining how a theory of thermodynamics arises from a theory of statistical quantum mechanics. Since classical thermodynamics has proved to be so remarkably successful a theory, and because quantum mechanics is the most accurate description of the microscopic world we have, we expect such a theory to replicate the results of the classical theory as the system size approaches macroscopic scales. Working with ensemble sizes which lie within the quantum limit raises the intriguing possibility of quantum thermodynamics deviating from the classical theory, or even resulting in the emergence of new thermodynamic phenomena.

The history of thermodynamics is intimately intertwined with the study of heat engines, originating with the need to understand the principles governing power output and efficiency of steam engines in the 19th century. Not only did the study of heat engines give rise to thermodynamics, but they continue to be one of its important practical applications. Additionally it can be shown that fundamental laws of thermodynamics can be recast entirely in terms of limitations on the performance of heat engines. In particular, after Carnot determined a remarkably general limit to the efficiency of a heat engine, early versions of the second law of thermodynamics were formulated in terms of performance limitations on the function of heat engines.

Because the study of heat engines form a foundational part of thermodynamics, it seems reasonable to use them as a system in which to look for quantum effects. Moreover, interest in their study need not be purely academic – with the rate at which devices are being miniaturised and with the effort being put into developing nanotechnology, it is not beyond the realms of possibility that we might eventually need to consider quantum mechanical effects in the functioning of future miniature machines [7, 8]. Should we eventually create machines which are sufficiently small for quantum effects to become noticeable, then not only might we wish to understand how they might influence the performance of the machine, but also determine whether they might be utilised to our advantage. Feynman was one of the first to consider the possibility of machines working in the microscopic world, which he detailed in his talk ‘There’s plenty of room at the bottom’ [9].

The notion of a quantum heat engine was first formally introduced in the seminal paper by Scovil and Schultz-DuBois considering a 3-level MASER as a heat engine [10]. They were not only able to show that the MASER is a form of heat engine, but further that the efficiency of such an engine is still bound by the Carnot limit. Whilst there has been a substantial amount of theoretical research conducted into quantum heat

engines over the last few years, progress on experimental implementations has lagged considerably behind. However, in recent years there have been several experiments which have begun to test heat engines in the quantum realm [11]. There is also a growing list of proposals for potential experimental quantum heat engines [12, 13, 14, 15].

An early experiment pushing into the microscopic realm was described in the paper by Blickle and Bechinger [16]. In this experiment the working fluid consisted of a single colloidal particle suspended in a volume of water and confined using an optical laser trap. With this setup, the authors were able to implement a four step Stirling cycle. The work strokes consisted of isothermal compression and expansions, which were implemented by changing the width of the trapping potential. The amount of work done during the compression/expansion steps was dependent on the spatial width of the particle probability distribution. The heating and cooling were done via the surrounding water, which was heated using a laser matched to a water absorption peak, and cooled using standard thermalisation. The engine cycle consisted of isochoric heating, followed by an isothermal expansion, then isochoric cooling, and finally isothermal compression. They were able to study the effect of thermal fluctuations on the engine, as well as the conditions for maximal power output and efficiency, and their dependence of dissipation effects in the engine. These dissipative effects were magnified at short cycle times, which resulted in the machine producing negative net power (extracting energy from the work reservoir) for sufficiently short cycle times.

J. Roßnagel et al. demonstrated the first single atom heat engine [11], whose working fluid consisted of a single Calcium ion ($^{40}\text{Ca}^+$) confined using a Paul trap with tapered geometry. The hot and cold reservoirs were provided by electric noise and laser cooling respectively, with the laser cooling being kept on continuously. They were able to study the thermal cycles as a function of the temperature difference

between the reservoirs and the thermalisation of the ion under continuous coupling to each of the reservoirs individually. The effect of changing the temperature of the ion was to produce an axial force, resulting in it moving it axially along the trap and changing its potential energy, which constituted the work produced by the engine. Continued periodic application of the heating and cooling steps resulted in the ions oscillating back and forth in the trap. Work was stored in the oscillations of the ion, and done against an additional axial laser which was used to provide friction. They were able to measure the power output measuring the amplitude of the oscillations. The significance of this experiment lies in the fact that it demonstrates that heat engines can be scaled all the way down to the single atom limit. Although the working substance did consist of a single atom, the performance characteristics of the engine were still classical, demonstrating that the engine being a quantum entity need not imply that the thermodynamics be non-classical.

There have also been an experimental proposals to make use of superconducting circuits [15, 14]. Niskanen et al. describe a microscopic refrigerator to lower the temperature of a thin-film resistor by transferring heat to another thin-film resistor at a higher temperature by the use of a single superconducting flux qubit. The qubit is sandwiched between two LC circuits, with different resonance frequencies. By modulating the qubit using an external energy source, energy is transferred from one circuit to the other, lowering the temperature of the cooler resistor from 400mK to 3mK. Campisi et al. also propose using two such superconducting circuits, but now as a heat engine in order to study the role of thermal fluctuations in the operation of microscopic heat engines.

There are others who have proposed to make use of the recent advances in optomechanics to implement quantum heat engines. The conventional goal for optomechanical experiments is to cool the macroscopic oscillator down to its phonon

ground state. This is done by coupling cavity photons and oscillator phonons through radiation pressure acting on one of the cavity mirrors, which enables the conversion from one mode to the other. By contrast, the heat engine form uses the thermal energy in the phonon bath to produce work, with the remaining heat being dumped into the optical vacuum coupled to the cavity mode, which assumes the role of the cold reservoir. Finally, the cavity mode is taken to be the work reservoir. Here the coupling rates are given by the cavity decay rate and the mechanical damping. Such an engine is described in the paper by Zhang et al. [12], where it is cycled by varying the detuning between the phonon and cavity modes, so that the engine undergoes an Otto cycle. Alternatively, they also show that this can be reversed and work extracted from background radiation if working in the microwave rather than optical domain.

When we restrict ourselves to thermal baths [17], both quantum and classical engines operating at optimal efficiency are quasi-static and so close to equilibrium at each point of the cycle [6]; in this realm there is little to tell apart the performance of quantum and classical engines. Limits on the efficiency such as the Carnot ($\eta_{Carnot} = 1 - T_c/T_h$) and Curzon-Ahlborn (Eq. 2.13) bounds are derived without reference to a specific engine, and so continue to apply to quantum heat engines. For this reason, in order to observe any nonclassical behaviour we need to either deviate from this equilibrium condition, or relax the condition on the reservoirs being thermal.

One instance of quantum effects arising in non-equilibrium heat engine cycles is a friction-like term, the presence of which was determined by a detailed analysis of the dynamics of Otto cycles by Kosloff et al. in [18, 19, 20]. It was shown that this term derives from the non-commutivity of quantum operators, and so is entirely quantum in origin. More specifically it is present on the adiabatic steps of the Otto cycle for systems in which the Hamiltonian, H , does not commute with itself at different times, $[H(t_1), H(t_2)] \neq 0$. The existence of studies such as this seemed to suggest that the

addition of quantum effects into a heat engine will be detrimental to its performance. This need not be the case, however, as shown in the study of quantum batteries by Binder et al. [21]. The authors of this paper were able to determine the optimal, finite time charging procedure for a single qubit battery; additionally, when extending the problem to an N qubit battery, they were able to show that entanglement can be used to achieve an N -fold advantage in charging power per qubit.

An alternative way to find nonclassical performance characteristics is to relax the condition that the baths be thermal and consider cases where they contain nonclassical correlations. Such baths are no longer in thermal equilibrium, though they are still required to be a genuine heat source in the sense that they should only exchange energy with the system via heat and not through work. It can be shown that a system coupled to a non-equilibrium reservoir no longer settles into a Gibbs state (the stationary state for a system in contact with a thermal reservoir of fixed temperature T - the ratios of populations in levels at energies E_1 and E_2 is given by $P(E_2)/P(E_1) = \exp(-(E_2 - E_1)/kT)$ [17]), but rather a perturbation of the Gibbs state [22]; further, it was determined that the efficiency of an engine operating between such reservoirs is bound by a generalised Carnot bound, $\eta \leq 1 - T_c^{\text{eff}}/T_h^{\text{eff}}$, where the effective temperature depends on the difference in average occupation numbers between the standard and perturbed Gibbs states. There have been several studies of heat engines operating between squeezed reservoirs [23, 24, 25]. It was shown that the addition of squeezing to a thermal reservoir enables an engine to achieve performance characteristics precluded by standard thermodynamics, including allowing it to extract work from a single reservoir, being able to achieve unit efficiency, and even achieve refrigeration and work extraction simultaneously [25, 23]. Although such an engine is able to surpass the standard Carnot limit, it is still bound by the generalised Carnot limit, in keeping with the second law [25]. These results don't take into ac-

count the cost of preparing such reservoirs, but rather consider them to be resources available for use, much as with the thermal reservoirs are in the standard heat engine. The introduction of coherence into a thermal reservoir can also have thermodynamic consequences, as demonstrated recently by Scully et al [26]. In this paper the authors consider a photon Carnot engine consisting of an optical cavity with one mirror doubling as a piston, which is driven by the radiation pressure within the cavity. Heat is supplied by a flow of three-level atoms through the cavity, which have previously been prepared by being brought into contact with a hot reservoir; the addition of a vanishingly small coherence between the levels in this atom provides a new control parameter in the form of the phase of the atomic coherence. Using reservoirs of this form, the authors demonstrate that such an engine operating in a Carnot cycle can be made to run more efficiently and produce more power than an engine without coherence; furthermore it was shown that one can obtain lasing without inversion and work extraction from a single reservoir.

More recently Uzdin, Levy and Kosloff determined two interesting effects that might be observed in quantum engines operating with coherence in the energy basis [27]. The first result demonstrates the equivalence in power output and heat flow for different engine types when operating in a weak driving limit. The second results proves the existence of a bound on the performance of an engine operating without coherence, which provides a means of distinguishing the performance of a quantum engine from a stochastic engine, providing what the authors defined to be a quantum thermodynamic signature – this is a thermodynamic measurement which definitely indicates the presence of quantum effects in the heat engine. These theoretical results underlie the work presented in this thesis, and will be discussed more fully in the following chapter.

This thesis documents an experimental study of quantum heat engines using the negative nitrogen vacancy centre in diamond. It is broken up into three broad parts.

To begin with, there is an overview of quantum thermodynamics and quantum heat engines, followed by an introduction to the nitrogen vacancy (NV) centre in diamond. Then the implementation of a quantum heat engine using NV is described together with the design of the experimental setup. Finally, the experimental and theoretical results from this study are presented and discussed. The result from these experimental efforts was the first demonstration of quantum effects in the operation of a physical microscopic heat engine whose environment is thermal.

Chapter 2

Background Theory

2.1 Quantum Thermodynamics

Quantum Thermodynamics is the field which attempts to extend the study of thermodynamics into systems which are non-classical. It is a comparatively new field of study in its own right, although it might be argued that it can trace its origins back to the very beginnings of quantum mechanics and Planck's solution to the ultraviolet catastrophe for black body radiation. The principal aim of quantum thermodynamic is to determine how the laws of quantum mechanics, describing the dynamics of single (or small numbers of) particles, might give rise to a statistical theory for ensembles of particles, from which macroscopic thermodynamic variables and their governing rules could be extracted. Since quantum theory provides our most accurate fundamental description of the underlying constituents of matter and their behaviour, we expect any theory of quantum thermodynamics to replicate the results of classical thermodynamics in the limit as the system size approaches macroscopic scales. The fact that the quantum world is so very different our familiar macroscopic world also raises the possibility of the quantum theory deviating from classical thermodynamics in this realm; this includes the possibility of completely new thermodynamic phenomena,

and perhaps even violations of the heretofore unshakable laws of thermodynamics. Motivated by this possibility, theoretical studies to determine the validity of the laws of classical thermodynamics in the quantum realm have formed an important part of the nascent field. Perhaps surprisingly, so far these studies indicate that the foundational laws of thermodynamics continue to hold good in the quantum world [6, 5]. Nevertheless, the question as to whether there is anything to distinguish quantum thermodynamics from the classical theory remains open, and the subject of active research. The remainder of this chapter is a brief overview of the subject, specifically focussing on work relating to quantum heat engines.

2.1.1 Dynamical Quantum Thermodynamics

The analysis of quantum heat engines in this thesis is based on a study of the dynamics of the heat engine. This approach is founded on the study of open quantum systems, using Lindblad-type equations as its principle tool, and is a standard method used in the study of quantum heat engines [28, 29, 30, 31]. Below some of the basic concepts and tools that underlie these methods are described.

Completely Positive Trace Preserving maps

Recall that, if our system is in a statistical ensemble of quantum states, then the appropriate description is given by the density matrix formalism. Given a system which has probabilities $\{p_i\}$ of being in state $\{\psi_i\}$, the density matrix, denoted ρ , is given by,

$$\rho = \sum_i p_i |\psi_i\rangle \langle \psi_i|$$

Notice that ρ is an operator rather than a wavefunction. If the state evolves according

the the Schrodinger equation, $i\hbar \partial_t |\psi\rangle = H |\psi\rangle$, then the density matrix evolves according to Eq 2.1.

$$i\hbar \partial_t \rho = [H, \rho] \quad (2.1)$$

If $U(t)$ is the unitary evolution operator for the system (the solution to $i\hbar \partial_t U = HU$, with $U(t=0) = \mathbb{I}$) then the solution to Eq. 2.1 is simply given by,

$$\rho(t) = U(t)\rho(0)U(t)^\dagger, \quad (2.2)$$

It is useful to describe an operator analogous to U for the density matrix. Because this operator acts on an operator, it is termed a superoperator. The density matrix time evolution superoperator, denoted $\Lambda(t)$, is defined by,

$$\Lambda(t) : \rho \mapsto U(t)\rho U(t)^\dagger$$

$\Lambda(t)$ describes a special form of map known as a completely-positive, trace preserving (CPTP) map. These mappings are endomorphisms on the set of density matrices (they map density matrices to density matrices), and represent the allowed processes that a physical system can undergo.

Definition 1 (Completely positive trace preserving maps).

A CPTP map, $\Lambda : \mathcal{M}_d \rightarrow \mathcal{M}_d$, is one which satisfies the following:

1. $\text{Tr}[\Lambda(\rho)] = \text{Tr}[\rho] \quad \forall \rho \in \mathcal{M}_d$.
2. $(\mathbb{I}_k \otimes \Lambda)(\rho)$ is positive semi-definite for all density matrices $\rho \in \mathcal{B}(\mathcal{H}_k \otimes \mathcal{H}_d)$ and $k \in \mathbb{N}$.

The first condition ensures that we can continue to interpret the diagonal elements as probabilities. The second point is more subtle: first, complete positivity implies

positivity, which is again required for the probabilistic interpretation of the diagonal elements; the reason that we require complete positivity, rather than just positivity, is because this description must consistently describe a joint system and an environment, with Λ acting on the system alone.

The form of Λ in Eq. 2.2 is a special form of CPTP map, which describes unitary evolution of the system; however, there are more general forms of process which are not described by such unitary evolution. In general a CPTP map may be expressed as [32],

$$\Lambda(\rho) = \sum_k B_k \rho B_k^\dagger, \quad (2.3)$$

where $\sum_k B_k^\dagger B_k = \mathbb{I}$. It can be shown that any CPTP map is equivalent to unitary evolution on a joint system and environment, followed by tracing out the environment.

Up to now we have only considered single maps, but we are interested in determining how these maps arise from some underlying temporal dynamics and the time dependence of the map, in a manner analogous to the time dependence of the unitary evolution operator. The requirements that such a set of operators needs to satisfy are set out in definition 2.

Definition 2 (Quantum Dynamical Semigroup). *A quantum dynamical semigroup is a one parameter family of linear CPTP maps, $\{\Lambda_t \mid t \in \mathbb{R}\}$, which satisfy,*

1. $\Lambda_{t+s} = \Lambda_t \Lambda_s$
2. $\langle A \rangle(t) = \text{Tr}[A(\Lambda_t \rho)]$ is a continuous function of t for all ρ and A .

We say that an operator \mathcal{L} is the generator for a quantum dynamical semigroup, $\{\Lambda_t\}$, if it satisfies $\partial_t \Lambda_t = \mathcal{L} \Lambda_t$. Lindblad [33] and Gorini, Kossakowski and Sudarshan [34] were independently able to prove the general form that such a generator assumes, which is given in Theorem 1, which gives us the well known Lindblad equation.

Theorem 1 (Generators for semigroups of quantum channels).

A linear map $\mathcal{L} : \mathcal{M}_d(\mathbb{C}) \rightarrow \mathcal{M}_d(\mathbb{C})$ is the generator of a continuous dynamical semigroup of trace-preserving CP maps iff it can be written in the form:

$$\mathcal{L}(\rho) = i[\rho, H] + \sum_k A_k \rho A_k^\dagger - \frac{1}{2} \left\{ A_k^\dagger A_k, \rho \right\}$$

where H is hermitian and $\{A_k\}_k \subseteq \mathcal{M}_d(\mathbb{C})$.

Proof. Lindblad [33], Gorini, Kossakowski and Sudarshan [34]. □

This result immediately gives us the Lindblad equation for the evolution of a density matrix,

$$i\hbar\partial_t\rho = [\rho, H] + L(\rho), \tag{2.4}$$

where the dissipative term, L , is given by,

$$L(\rho) = \sum_k A_k \rho A_k^\dagger - \frac{1}{2} \left\{ A_k^\dagger A_k, \rho \right\}$$

The operators A_k quantify the effect of the environment on system and are known as Lindblad operators. Prior to the above result Davies showed that such a Markovian Master Equation described the interaction of a system weakly coupled to a heat bath composed of an ideal fermionic gas [35]. The exact form of these operators needs to be derived for each case in question – the derivation generally involves the use of weak coupling, Markovian and Born approximations [28]. It can be shown that the interaction of a thermal bath with a harmonic oscillator results in there being two Lindblad operators [36, 37, 29],

$$A_1 = \sqrt{\gamma} \hat{a} \quad \text{and} \quad A_2 = \sqrt{\gamma} e^{-\frac{1}{2}\beta\omega} \hat{a}^\dagger$$

Here ω is the spacing of the oscillator energy levels (the angular frequency of the oscillator) and $\beta = 1/(k_B T)$ is the inverse temperature. The parameter γ is the strength of the coupling, which depends on details of the situation in question. These Lindblad operators can be interpreted as the bath exciting the system by one quanta at an average rate of $\gamma e^{-\beta\omega}$, whilst removing one quanta at an average rate of γ . The systems that we consider are different from harmonic oscillators, as they are taken to be finite and are allowed to have variable energy spacings; nevertheless it is possible to write down analogous Lindblad operators for such a system. Suppose we have a thermal bath of inverse temperature β coupling two states $|i\rangle$ and $|j\rangle$, with energy difference $\Delta E = E_j - E_i > 0$. Then the Lindblad operators describing this interaction are [27],

$$A_{ij} = \sqrt{\gamma} e^{-\frac{1}{2}\beta\Delta E} |j\rangle \langle i| \quad \text{and} \quad A_{ji} = \sqrt{\gamma} |j\rangle \langle i|,$$

where $\gamma > 0$ quantifies the system-reservoir coupling strength.

2.1.2 Liouville space

It is more convenient to work in the Liouville (or superoperator) space, where the density matrix is vectorised (this can be thought of as flattening out the matrix, for instance concatenating all the rows), $\rho \mapsto |\rho\rangle$. This allows one to use the familiar representation of linear transformations as matrices, rather than rank 4 tensors. Suppose that our system has a Hamiltonian H and Lindblad operators $\{A_k\}$, so that the system simply evolves according to Eq 2.4. We are then able to define operators \mathcal{H} and \mathcal{L} by,

$$\mathcal{H}|\rho\rangle = |[\rho, H]\rangle \quad \text{and} \quad \mathcal{L}|\rho\rangle = |L(\rho)\rangle$$

Eq 2.4 can be expressed in terms of these operators as,

$$i\hbar\partial_t|\rho\rangle = (\mathcal{H} + \mathcal{L})|\rho\rangle$$

If we can further split the Hamiltonian into bare and interaction terms, then we can write $\mathcal{H} = \mathcal{H}_0 + \mathcal{H}_I$, and transform into the interaction picture,

$$i\hbar\partial_t|\tilde{\rho}\rangle = (\tilde{\mathcal{H}}_I + \tilde{\mathcal{L}})|\tilde{\rho}\rangle$$

Here the tilde represents the state/operator in the interaction picture: $|\tilde{\rho}\rangle = U|\rho\rangle$ and $\tilde{A} = UAU^\dagger$, where $U(t) = \exp(-i\mathcal{H}_0 t/\hbar)$. Henceforth I will work exclusively in the interaction picture and so drop the tildes, and simply write,

$$i\hbar\partial_t|\rho\rangle = (\mathcal{H} + \mathcal{L})|\rho\rangle, \tag{2.5}$$

2.1.3 First Law

Suppose our Hamiltonian is given by $H = H_0 + V(t)$. There are two distinct extreme situations we can consider, together with a continuum of possibilities lying between them. The first occurs when the time dependent term $V(t)$ varies adiabatically, so that the system's energy levels change with time, and our internal energy is given by $U = \text{Tr}(\rho H)$. Taking the time derivative yields,

$$\langle d_t U \rangle = \text{Tr} \left(\frac{d\rho}{dt} H \right) + \text{Tr} \left(\rho \frac{dH}{dt} \right)$$

This suggests that we might identify these two terms with the heat and work flows.

The first term describes changes in the system which are not linked to changes in its Hamiltonian; thus these can be associated with interactions between the system and its environment, which results in changes beyond our direct control, and can therefore be identified with heat flow. The second term describes changes in the internal energy due to changes in the system Hamiltonian, over which we do have control, and allows us to identify this term with work flow into the system. Thus we can write [6],

$$\langle Q \rangle = \int \text{Tr}(\dot{\rho} H) dt \quad \text{and} \quad \langle W \rangle = \int \text{Tr}(\rho \dot{H}) dt \quad (2.6)$$

We can substitute Eq. 2.4 into the heat expression to show,

$$\begin{aligned} \langle Q \rangle &= -\frac{i}{\hbar} \int \text{Tr}(H \mathcal{L}(\rho)) + \text{Tr}([H, \rho] H) dt \\ &= -\frac{i}{\hbar} \int \text{Tr}(H \mathcal{L}(\rho)) dt \end{aligned}$$

Thus Q is due solely to the interaction with the environment, as expected. In the superoperator picture, expectation values are given by,

$$\langle A \rangle_{\rho} = \text{Tr}(\rho A) = \langle A | \rho \rangle \quad (2.7)$$

So we can recast the definitions 2.6 into the superoperator picture:

$$\langle Q \rangle = -\frac{i}{\hbar} \int \langle H | \mathcal{L} | \rho(t) \rangle dt \quad \& \quad \langle W \rangle = -\frac{i}{\hbar} \int \langle \dot{H} | \rho(t) \rangle dt \quad (2.8)$$

When the Hamiltonian no longer changes adiabatically, it is not longer straightfoward to seporate out the heat and work. This case still presents an open research question; however if the thermal and unitary interactions are applied seperately, then we can

still define heat and work by examining the internal energy of the system at the end of each of these periods. In either case the First Law of Thermodynamics (Eq. 2.9) is satisfied.

$$\langle \Delta U \rangle = \langle Q \rangle + \langle W \rangle \quad (2.9)$$

2.1.4 Entropy and the Second Law

The second law of thermodynamics is a statement that the entropy of a closed system cannot decrease in time.

$$\Delta S \geq 0 \quad (2.10)$$

This statement is closely linked with performance limitations on heat engines, in terms of which the second law was first stated [17]. When working in the quantum world it is possible to extend the classical definition of thermodynamic entropy in a straightforward manner [6], using the definitions of heat described in the previous section,

$$\Delta S_{th} = \int_{rev} \frac{\langle \delta Q \rangle}{T}$$

The von Neumann entropy is the version used more often in the quantum domain; this definition has an information theoretic origin and is defined naturally in terms of the density matrix, and is given by,

$$S_{vn} = -\text{Tr}(\rho \ln \rho)$$

The von Neumann entropy is simply an extension of the Shannon entropy to the

quantum domain; moreover, the Shannon entropy is equivalent to the statistical mechanics definition of the entropy of a system (up to proportionality), which is given by,

$$S = -k_B \sum_i p_i \log(p_i)$$

This can be seen to reduce to the more familiar expression of $S = -k_B \log |\Omega|$ in the case of equiprobable microstates (the equal a priori probability postulate of statistical mechanics).

Whilst the thermal entropy and von Neumann entropy may appear to be unrelated, it can be shown that they agree on a particular, but important, set of states known Gibbs states. Recall that the canonical ensemble describes a system in thermal equilibrium with a reservoir – it is the state that maximises the entropy of the system subject to a fixed energy, or equivalently it minimises the energy for fixed entropy. The Gibbs state is the quantum state analogous to the canonical ensemble, and for temperature T it is defined by,

$$\rho = \frac{1}{\mathcal{Z}} e^{-\beta H}, \text{ where } \mathcal{Z} = \text{Tr} [e^{-\beta H}] \text{ and } \beta = 1/k_B T$$

A system coupled to a thermal reservoir of inverse temperature β has the Gibbs state as its limit point, regardless of the initial state. Gibbs states belong to a special class of state known as passive states, which are those states from which we cannot extract energy using unitary transformations [5]. More formally they are those states, ρ , for which,

$$\text{Tr} [\rho H] \leq \text{Tr} [U \rho U^\dagger H] \quad \forall U \in U(n)$$

It can be shown that such states must be diagonal in the energy basis, and have monotonically decreasing elements when ordered according to their energies. This

can be thought of as a manifestation of the Kelvin formulation of the second law, which prevents us from extracting work from a system coupled only to a single thermal reservoir. The efficiency of a heat engine is closely related to the production of entropy during the engine cycle. The Carnot cycle, which is able to achieve the maximum possible efficiency, set by the Carnot limit, is reversible and so produces no net entropy; this reversibility comes at the cost of the cycle taking infinite time, and consequently the engine having zero power output.

2.1.5 Dynamical analysis of Quantum Heat Engines

Here we consider a dynamical description of the operation of a quantum heat engine; this is one of the primary techniques used in the study of quantum heat engines, and it was in this formalism that the theoretical results underlying this experiment were derived. The formalism is based on the study of open quantum systems [29, 28], where we consider our working fluid to be the system of interest, with the thermal baths forming the environment.

Continuous Engines

There are a number of different types of heat engine in both the quantum and classical domains, the simplest of which is the continuous engine. This engine has the working medium coupled constantly to each of the thermal reservoirs and work reservoir, as illustrated in Fig. 2.1,

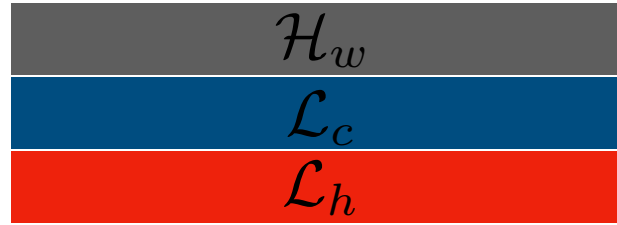


Figure 2.1: Continuous engine block diagram. The horizontal axis represents time, whilst the vertical axis represents the interaction strength for the relevant interaction.

This requires a system with a minimum of three levels to function. A schematic of a continuous engine implementation is given in Fig. 2.2.

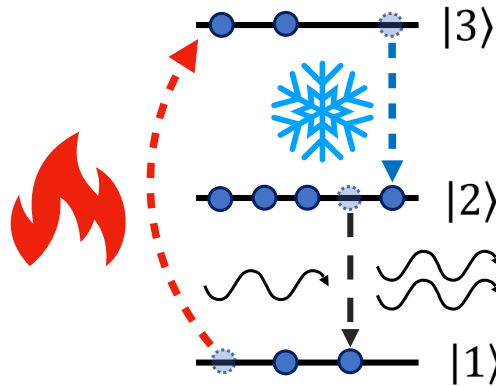


Figure 2.2: 3-level continuous engine schematic. The first and third levels are coupled by the hot reservoir, the second and third by the cold reservoir, and the first and second by the work reservoir. The combined effect of the thermal reservoirs is to continuously create an inversion between the first and second levels, which can be exploited for work.

This system was first analysed in the context of heat engines in the paper by Scovil and Schulz-DuBois [10]. The condition for this engine to produce work is that there be a population inversion, as is the case for a LASER/MASER. It can further be shown that the performance of this engine is still bound by the Carnot limit – this follows quite simply from the Boltzmann factors describing the steady state population ratios due to the baths. The ratio of populations in $|1\rangle$ and $|2\rangle$ at thermal equilibrium is given by,

$$\frac{p_2}{p_1} = e^{-\beta_h \omega_{13}} \times e^{\beta_c \omega_{23}}$$

Here $\omega_{ij} = E_i - E_j$ and $\beta = 1/kT$. The condition for work production is that this quantity be greater than unity, which implies $\beta_h \omega_{13} < \beta_c \omega_{23}$, or equivalently, $T_c/T_h < \omega_{23}/\omega_{13}$. The efficiency at steady state is then given by,

$$\eta = \frac{W}{Q_h} = \frac{\omega_{12}}{\omega_{13}} = 1 - \frac{\omega_{23}}{\omega_{13}} < 1 - \frac{T_c}{T_h} \equiv \eta_{carnot},$$

demonstrating that the engine is indeed bound by the Carnot limit. This limit can only be achieved on the brink of inversion, which implies zero power output, as in the case of the classical Carnot engine. This engine can be viewed as a form of quantum amplifier, which is able to increase the number of photons at frequency ω_{12} through the process of stimulated emission. A more detailed analysis of the dynamics of a continuous engine, including analyses of entropy production, efficiency-power tradeoff, and conditions for maximum power are given in Ref. [38].

Reciprocating Engines

Reciprocating engines are those which have a well defined cycle time, and distinct strokes during each cycle, which results in the engine having non-trivial dynamics when steady state operation has been reached (steady state corresponds to periodic time evolution of the engine state with period equal to the cycle duration).

There are two widely studied varieties of reciprocating engine, the Otto engine and the Carnot engine, with the Otto engine having received the greater share of attention due to it being simpler to study theoretically [30]. The Otto engine does differ in several aspects from the variety of engine studied in this thesis; nevertheless, because the quantum Otto cycle is the prototype reciprocating quantum heat engine and because

the techniques used in its study are applicable to reciprocal engines more generally, I will give a brief overview of the Otto engine and these approaches.

Reciprocating engines are described by cycles which are products of CPTP maps, with each corresponding to a distinct stroke in the cycle. If the individual strokes are described by operators \mathcal{K}_i , then the total cycle operator is given by,

$$\mathcal{K}_{cyc} = \prod_i \mathcal{K}_i \quad (2.11)$$

A steady state of the system is given by the zero eigenvector of $(\mathcal{K}_{cyc} - \mathbb{I})$,

$$\mathcal{K}_{cyc} \rho_0 = \rho_0$$

If the kernel of $(\mathcal{K}_{cyc} - \mathbb{I})$ is one dimensional, then the engine has a unique steady state ρ_0 . In this case \mathcal{K}_{cyc} is referred to as relaxing, and the engine always settles to ρ_0 , regardless of the starting state. This can be written as,

$$\lim_{n \rightarrow \infty} (\mathcal{K}_{cyc})^n \rho = \rho_0$$

The Otto cycle is a four stroke engine which is depicted schematically in Fig. 2.3.

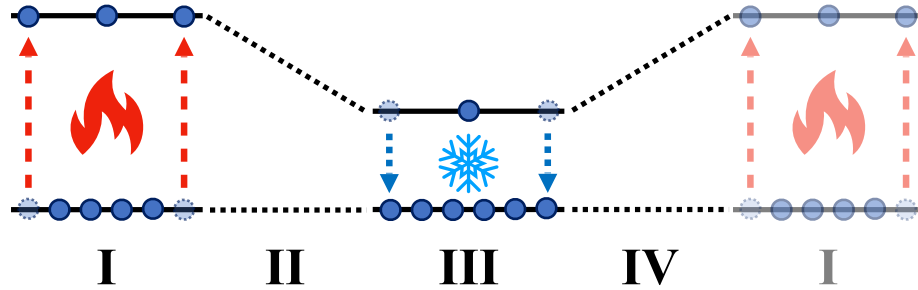


Figure 2.3: Schematic of the Otto engine cycle in a two level system. The hot bath is first coupled to the hot reservoir, transferring population into the upper level, after which the spacing between the levels is reduced, producing work; then the cold reservoir is coupled moving population back down into the ground state, which is followed by an expansion of the level spacing, which requires work. There is net work produced because of the difference in population ratios between the level expansion and contraction steps.

One such example of an Otto cycle operating in the quantum regime, and one often considered in the literature [39, 11, 30], is a particle in a trapping potential. The sequence is as follows,

1. Hot isochore – the working substance is coupled to a hot reservoir, increasing its temperature whilst holding the trapping potential fixed, so that, again, no work is done. The engine gains entropy in this step.
2. Isentropic expansion – the curvature of the trap potential is reduced, allowing the working substance to expand without heat transfer, such that the entropy is constant and its internal energy scale is decreased.
3. Cold isochore – the working substance is coupled to a cold reservoir, decreasing its temperature whilst holding the trapping potential fixed, such that no work is done. The engine entropy is reduced in this step.
4. Isentropic compression – the curvature of the trap potential is increased, compressing the working substance, again without heat transfer, such that the en-

trophy is constant and its internal energy scale is increased.

The engine is able to produce a net positive amount of work due to the asymmetry between the expansion and compression strokes, since the compression occurs at a lower temperature than the expansion. We need to consider what is meant by the volume of a few, or even single, particle engine. In some implementations, such as a single particle in a harmonic trap [30, 16, 11], this does correspond to a spatial volume in the form of the width of the trapping potential, which interacts with the spatial wavefunction of the particle. However, for the Otto cycle one simply requires that no work be exchanged between the system and the work reservoir during the ischores, and that the expansion/compression steps correspond to constant entropy processes in which no heat is exchanged between the system and environment. We denote the corresponding operators, cyclically shifted from the previous ordering, by,

$$\mathcal{K}_{cyc} = \mathcal{K}_h \mathcal{K}_{ch} \mathcal{K}_c \mathcal{K}_{hc}$$

Note that we can express the work done and heat flow comparatively simply in terms of these operators:

$$W = \langle H_0 | (\mathcal{K}_{hc} - \mathbb{I}) | \rho_0 \rangle + \langle H_0 | (\mathcal{K}_{ch} - \mathbb{I}) \mathcal{K}_c \mathcal{K}_{hc} | \rho_0 \rangle$$

$$Q_h = \langle H_0 | (\mathcal{K}_h - \mathbb{I}) \mathcal{K}_{ch} \mathcal{K}_c \mathcal{K}_{hc} | \rho_0 \rangle$$

$$Q_c = \langle H_0 | (\mathcal{K}_c - \mathbb{I}) \mathcal{K}_{hc} | \rho_0 \rangle$$

The efficiency is given by,

$$\eta = \frac{W}{Q_h} \leq \eta_c \equiv 1 - \frac{T_c}{T_h} \quad (2.12)$$

In both classical and quantum realms, engines operating at maximum efficiency are necessarily quasi-static and so produce no power. Any deviation from this quasi-static condition reduces the efficiency of the engine (even in the absence of friction and heat leaks) and is the focus of studies of power/efficiency trade-off. Curzon and Ahlhorn determined the efficiency of a Carnot engine working at maximum power output, which is given by Eq. 2.13 [40]. It can further be shown that this bound extends to the case of a quantum Carnot engine [6, 5]:

$$\eta_{CA} = 1 - \sqrt{\frac{T_c}{T_h}} \quad (2.13)$$

The engine type considered in this thesis differs from the Otto engine by implementing its unitary work stroke using coherent driving of one of the system transitions, rather than adiabatically shifting the energy levels, similar to the continuous engine described in SubSec. 2.1.5. In this case talking about processes involving volume and pressure has little meaning; nevertheless, we can still describe our engine in terms of stroke operators as done in Eq. 2.11. These strokes are now described by Eq. 2.5. There are a number of variations of four stroke engine that one can implement which differ in their level scheme and stroke ordering [27], but the standard form has strokes which bear a close similarity to those in the Otto engine, and is represented in Fig. 2.4. The four-stroke engine has the following cycle decomposition,

$$\mathcal{K}_{cyc} = \mathcal{K}_h \mathcal{K}_{w_2} \mathcal{K}_c \mathcal{K}_{w_1}$$

We can explicitly write down the form of these operators, which are given by,

$$\begin{aligned}\mathcal{K}_{w_1}(t) &= e^{-\frac{i}{\hbar}\mathcal{H}_{w_1}t} \quad \text{and} \quad \mathcal{K}_{w_2}(t) = e^{-\frac{i}{\hbar}\mathcal{H}_{w_2}t} \\ \mathcal{K}_h(t) &= e^{-\frac{i}{\hbar}\mathcal{L}_h t} \quad \text{and} \quad \mathcal{K}_c(t) = e^{-\frac{i}{\hbar}\mathcal{L}_c t}\end{aligned}$$

Here \mathcal{K}_{w_i} describe the unitary strokes, whilst $\mathcal{K}_{h(c)}$ correspond to the hot (cold) thermal strokes. The expressions for the work and heat per stroke remain unchanged, although the instantaneous flows would now be calculated using Eq. ?? rather than Eq. 2.8.



Figure 2.4: Block diagram for a four-stroke engine. The horizontal axis represents time, and the vertical indicates the coupling strength.

Finally, one can also consider a two stroke variant of engine using the resonant driving form of unitary. In this engine, there are separate thermalisation and work steps, but now with both hot and cold baths coupled simultaneously during the thermal stroke – this is shown schematically in block diagram form in Fig. 2.6.

This has the following cycle decomposition,

$$\mathcal{K}_{cyc} = \mathcal{K}_{th}\mathcal{K}_w,$$

where the operators are now given by,

$$\mathcal{K}_{th}(t) = e^{-\frac{i}{\hbar}(\mathcal{L}_h + \mathcal{L}_c)t} \quad \text{and} \quad \mathcal{K}_w(t) = e^{-\frac{i}{\hbar}\mathcal{H}_w t}$$

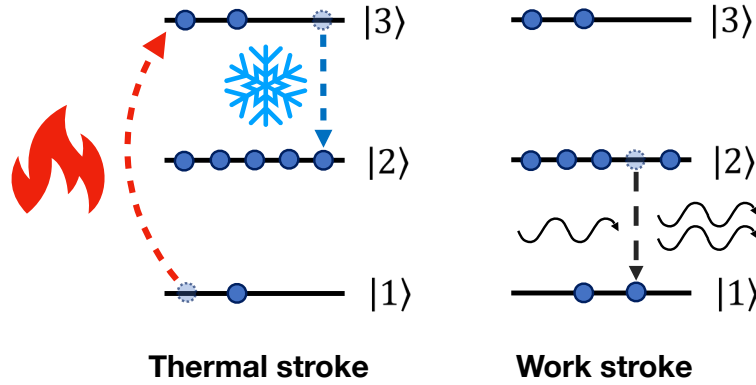


Figure 2.5: Two-stroke engine schematic. Both thermal reservoirs are coupled in the first stroke, creating a population inversion between the lower two levels. This inversion then allows for work extration through stimulated emission in the second stroke.

This functions much as one might expect – the thermal stroke creates a population inversion between levels $|1\rangle$ and $|2\rangle$, which is then exploited in the work stroke, by driving this transition and producing photons in this mode, through stimulated emission. This is illustrated schematically in Fig. 2.5.



Figure 2.6: Two-stroke engine block diagram. The horizontal axis represents time, and the vertical indicates the coupling strength. Note that the thermal reservoirs are coupled simulatenously unlike the four-stroke engine.

Finally, before we go further, it is necessary to define the notion of the *action* of a reciprocating quantum heat engine. Intuitively this can be thought of as the sum of the products of the coupling constants and the stroke periods, and indicates the

extent to which the system changes during a stroke. Formally it can be defined as follows.

Definition 3 (Action).

Suppose we have a heat engine evolving according to Eq. 2.5. Then, if we write $\mathcal{H} = \mathcal{H}_w + \mathcal{L}$, the action of the engine is defined by,

$$s = \int_0^{t_{cyc}} \|\mathcal{H}(\tau)\| d\tau$$

In the next two subsections I give an account of the material in the paper by Uzdin, Levy and Kosloff [27], which inspired the work in this thesis and provides its theoretical underpinnings. There are two significant results in this paper, both of which relate to quantum phenomena exhibited by engines whose working fluid possesses coherence in the energy basis. The first of these concerns the existence a bound on the performance of a stochastic engine, which provides a means of distinguishing the performance of a quantum engine from a stochastic engine, whilst the second demonstrates the thermodynamic equivalence of different engine types in the small action limit.

2.1.6 Quantum Thermodynamic Signatures

The second result demonstrated by Uzdin et al. was the prediction that coherence in the working fluid of a heat engine could produce measurable thermodynamic traces of its presence [27]. This was formalised using a concept called the quantum thermodynamic signature, which is defined in terms of an equivalent classical engine. To make any such comparison meaningful, the classical engine must be as similar as possible to the the quantum engine – so we require that it be obtained through a minimal possible set of modifications. More specifically, given a quantum engine, the authors postulated that the equivalent classical engine should satisfy the following set

of requirements:

1. The dynamics should be described entirely in terms of the populations.
2. The essential parameters of the engine should remain unchanged – this includes the level structure, the bath temperatures and the coupling strengths.
3. The modification should not introduce new sources of heat or work.

An additional condition is that the strokes comprising the engine should agree on their action on population only states, which gives the notion of an equivalent engine mathematical meaning. Suppose we have a stroke \mathcal{S} , and if \mathcal{S}_{stoch} is the classical stroke, then, for all density matrices ρ , this condition takes the form,

$$\mathcal{S}(\rho)|_{pop} = \mathcal{S}_{stoch}(\rho|_{pop})$$

It should be noted that these conditions do not uniquely determine the equivalent stochastic engine; however it does uniquely determine the overall effect of each stroke, and so the performance of the engine, ensuring this correspondence is well defined. It can be shown that the resulting strokes for this equivalent engine are given by the mapping in Eq 2.14 [27].

$$\mathcal{S} \mapsto \mathcal{S}_{stoch} = (\mathcal{D}\mathcal{S}\mathcal{D})|_{pop} \quad (2.14)$$

Here \mathcal{S} represents the quantum stroke operator, \mathcal{S}_{stoch} the corresponding classical operator, and \mathcal{D} is the complete dephasing operator, which is simply the projection operator onto the population subspace. Note that this mapping also satisfies all the conditions by construction. To construct the equivalent classical engine, we simply perform this operator for each of the constituent strokes of the original quantum engine, and then sandwich them together in the correct order. The thermal operators

are essentially left unchanged under this operation, since their action is closed on the population space. The unitary strokes get mapped to doubly stochastic operators, which can be interpreted as describing complete population swaps with certain probabilities. Given this mapping, one can then consider how the performance of the quantum engine differs from that of the corresponding classical engine. For this purpose, and for the sake of simplicity, we consider the two stroke engine. Let $\tilde{\rho}$ be the steady state of $\mathcal{K}_{th} \mathcal{K}_w$ (i.e $\mathcal{K}_{th} \mathcal{K}_w |\tilde{\rho}\rangle = |\tilde{\rho}\rangle$). Then the work done per stroke for the quantum two-stroke engine is given by,

$$W = -\langle H_0 | e^{-\frac{i}{\hbar} \mathcal{H}_w t_w} - \mathbb{I} | \tilde{\rho} \rangle, \quad (2.15)$$

Define $|\tilde{\rho}_{pop}\rangle \equiv \mathcal{D} |\tilde{\rho}\rangle$ and $|\tilde{\rho}_{coh}\rangle \equiv (\mathbb{I} - \mathcal{D}) |\tilde{\rho}\rangle$. Then one can split the work done per stroke into two distinct terms, one deriving entirely from the populations in the density matrix and one entirely from the coherences, as follows,

$$W = W_{pop} + W_{coh},$$

where $W_\alpha = -\langle H_0 | e^{-\frac{i}{\hbar} \mathcal{H}_w t_w} - \mathbb{I} | \tilde{\rho}_\alpha \rangle$ for $\alpha = pop, coh$. It can be shown that if our interaction derives from a dipole type coupling, $H_I = \vec{\mu} \cdot \vec{F}$, then by partitioning our basis into coherence terms and population terms, so that $|\rho\rangle = |\rho_{coh}\rangle \oplus |\rho_{pop}\rangle$, the Hamiltonian \mathcal{H}_w assumes the form,

$$\mathcal{H}_w = \begin{pmatrix} 0 & h \\ h^\dagger & 0 \end{pmatrix} \quad (2.16)$$

Because $|H_0\rangle$ only has population terms, this form results in even and odd powers of the expansion acting selectively on the population and coherence components, as shown below.

$$\langle H_0 | \mathcal{H}_w^{2n} | \rho_{coh} \rangle = 0 \quad \text{and} \quad \langle H_0 | \mathcal{H}_w^{2n+1} | \rho_{pop} \rangle = 0 \quad \forall n \in \mathbb{N}$$

Expanding the exponential of 2.15 and using these expressions yields,

$$W_{pop} = \sum_{k=1} \frac{1}{(2k)!} \left(\frac{-i}{2\hbar} \right)^{2k} \langle H_0 | \mathcal{H}_w^{2k} | \rho_{pop} \rangle t_w^{2k}$$

$$W_{coh} = \sum_{k=1} \frac{1}{(2k-1)!} \left(\frac{-i}{2\hbar} \right)^{2k-1} \langle H_0 | \mathcal{H}_w^{2k-1} | \rho_{coh} \rangle t_w^{2k-1}$$

It can be seen that to leading order $W_{pop} \sim \mathcal{O}(t_{cycle}^2)$ and $W_{coh} \sim \mathcal{O}(t_{cycle})$. This implies that, in the limit of $t_{cycle} \rightarrow 0$, $P_{pop} = W_{pop}/t_{cycle}$ vanishes, whilst $P_{coh} = W_{coh}/t_{cycle}$ tends to some constant proportional to the coherence.

The above observation forms the basis for the quantum thermodynamic signature. The goal is to determine whether the presence of coherence in the engine is able to modify the thermodynamic flows in such that they could not be produced by the corresponding stochastic engine. Measuring such a flow would then indicate the presence of coherence in the engine working fluid. The approach taken in Ref. [27] was to determine an upper bound on the performance of the stochastic engine, which, if broken, indicates that coherence must be present in the engine. It is important that this bound depends only on parameters which are not dependent on coherence in any way – in particular this requires that it be independent of the state of the system. For the purposes of this work, I will only describe the stochastic bound for the two-stroke engine; a more complete derivation can be found in Ref [27]. The power output from the equivalent classical engine is given by,

$$W_{stoch} = - \left\langle \tilde{H}_0 \left| \left(\mathcal{D} e^{-\frac{i}{\hbar} \mathcal{H}_w t_w} \mathcal{D} \right)_{pop} - \mathbb{I} \right| \tilde{\rho}_{pop} \right\rangle \quad (2.17)$$

where $\tilde{\rho}_{pop}$ need not be the same as ρ_{pop} , and $\tilde{H}_0 = H_0|_{pop}$. Using the previously derived relations it can be shown that only even powers of the expansion contribute to the work. This allows one to write,

$$W_{stoch} = \frac{t_w^2}{2\hbar^2} \left\langle \tilde{H}_0 \left| (\mathcal{D} \mathcal{H}_w^2 \mathcal{D})_{pop} \right| \tilde{\rho}_{pop} \right\rangle + \mathcal{O}((s/\hbar)^4) \quad (2.18)$$

In the case of the dipole interaction, the interaction Hamiltonian takes the form:

$$H_I = \frac{\hbar}{2} \begin{bmatrix} 0 & \Omega \\ \Omega^* & 0 \end{bmatrix}$$

It can be shown that,

$$(\mathcal{D} \mathcal{H}_w^2 \mathcal{D})_{pop} = \frac{1}{2} \hbar^2 \Omega^2 \begin{bmatrix} 1 & -1 & 0 \\ -1 & 1 & 0 \\ 0 & 0 & 0 \end{bmatrix}$$

Substituting this back into Eq. 4.5 we have,

$$\begin{aligned} W_{stoch} &= \frac{1}{4} t_w^2 \Omega^2 [0, \hbar\omega_{12}, \hbar\omega_{13}] \begin{bmatrix} 1 & -1 & 0 \\ -1 & 1 & 0 \\ 0 & 0 & 0 \end{bmatrix} \begin{bmatrix} \tilde{\rho}_{11} \\ \tilde{\rho}_{22} \\ \tilde{\rho}_{33} \end{bmatrix} \\ &= \frac{1}{4} \hbar\omega_{12} t_w^2 \Omega^2 (\tilde{\rho}_{22} - \tilde{\rho}_{11}) \end{aligned}$$

In order to ensure that our final quantity is state independent, we maximise over all possible population states. We use the fact that $0 \leq \tilde{\rho}_{11}, \tilde{\rho}_{22} \leq 1$ to obtain,

$$W_{stoch} \leq \frac{1}{4} \hbar \omega_{12} t_w^2 \Omega^2$$

Therefore the work per cycle from a stochastic engine, with coupling Ω to the work reservoir and work stroke duration t_w , is constrained to lie below the above bound irrespective of the details of the thermalisation step. This can be cast in terms of a bound on the power by dividing through by the cycle time,

$$P_{stoch} \leq \frac{1}{4} \hbar \omega_{12} d \Omega^2 t_w, \quad (2.19)$$

where d is the duty cycle. A theoretical example of this is given in Fig. 2.7

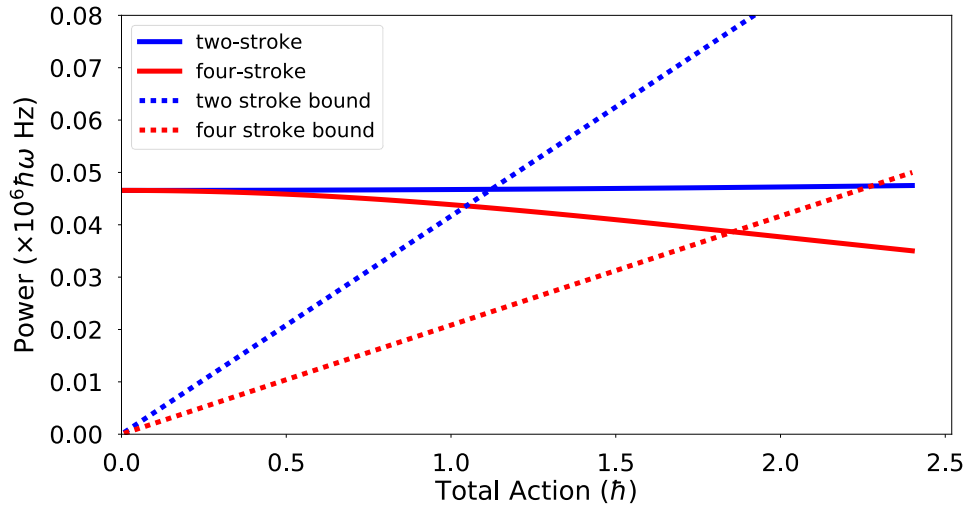


Figure 2.7: Demonstration of beating the stochastic bound. The two-stroke and four-stroke duty cycles are 50% and 25% respectively. Here the temperatures are given by $\omega_h/kT_h = 1$ and $\omega_c/kT_c = 2$ for both engine types. The two-stroke coupling strengths are $\Omega = \gamma_h = \gamma_c = 2.5$ MHz, whilst the corresponding couplings for the four-stroke engine are 5 MHz. It can be seen that the coherent engine power output is greater than the stochastic bound in both cases for actions less than \hbar , whilst both drop below the bound for larger actions.

2.1.7 Equivalence of quantum heat machines

This result relates to thermodynamic equivalence of different engine varieties in the small action limit. We begin by considering the three fundamental engine types: continuous, two-stroke, and four-stroke. This result is reached by showing that each of the different stroke varieties is equivalent to the continuous engine as the action tends toward zero provided the average couplings are equal for each case. Recall that strokes are simply given by evolution operators of the form $\exp(\mathcal{A}t)$, with the total cycle evolution being a product of such operators. The result relies on being able to decompose the exponential of a sum into a product of operators. If we were dealing with numbers (or any abelian set) then this occurs trivially since we have, $\exp(a + b) = \exp(a) \exp(b)$. However, because operators do not commute in general, we use a decomposition known as the Strang decomposition [27, 41],

$$e^{t(X+Y)} = e^{\frac{1}{2}tY} e^{tX} e^{\frac{1}{2}tY} + \mathcal{O}(s^3)$$

where $s = (\|X\| + \|Y\|)t$. $\|X\|$ is the spectral norm of the operator X . For this decomposition to be valid we simply require $s \ll 1$. In this case we write,

$$e^{t(X+Y)} \cong e^{\frac{1}{2}tY} e^{tX} e^{\frac{1}{2}tY}$$

Suppose that we have a two-stroke engine with cycle time τ_{cyc} , that we wish to compare a continuous engine. Then evolution of a continuous engine in time τ_{cyc} is given by,

$$\mathcal{K}_{cont} = e^{-\frac{i}{\hbar}(\mathcal{H}_w + \mathcal{L}_c + \mathcal{L}_h)\tau_{cyc}}$$

We can now apply the Strang decomposition to this operator to obtain,

$$\mathcal{K}_{cont} \cong e^{-\frac{i}{2\hbar}\mathcal{L}\tau_{cyc}} e^{-\frac{i}{\hbar}\mathcal{H}_w\tau_{cyc}} e^{-\frac{i}{2\hbar}\mathcal{L}\tau_{cyc}}$$

Finally, in order to compare this to the two-stroke engine, we need to ensure that the sum of the stroke times in the above decomposition is equal to τ_{cyc} . This is achieved by simply rescaling the couplings,

$$\mathcal{K}_{cont} \cong e^{-\frac{i}{\hbar}\left(\frac{1}{\alpha}\mathcal{L}\right)\left(\frac{\alpha}{2}\tau_{cyc}\right)} e^{-\frac{i}{\hbar}\left(\frac{1}{\beta}\mathcal{H}_w\right)(\beta\tau_{cyc})} e^{-\frac{i}{\hbar}\left(\frac{1}{\alpha}\mathcal{L}\right)\left(\frac{\alpha}{2}\tau_{cyc}\right)},$$

where $\alpha + \beta = 1$. Finally, because this operator is applied repeatedly, cyclic rotations of these operators produce equivalent engines, so we can write,

$$\mathcal{K}_{cont} \cong e^{-\frac{i}{\hbar}\left(\frac{1}{\alpha}\mathcal{L}\right)(\alpha\tau_{cyc})} e^{-\frac{i}{\hbar}\left(\frac{1}{\beta}\mathcal{H}_w\right)(\beta\tau_{cyc})} \quad \text{if } (\|\mathcal{H}_w\| + \|\mathcal{L}_c\| + \|\mathcal{L}_h\|) \tau_{cyc} \ll \hbar$$

We can identify β as the duty cycle ($d = \tau_w/\tau_{cyc}$) of the engine. Thus we can see that the two stroke engine with duty cycle d is equivalent to a continuous engine with thermal and unitary operators given by $(1 - d)\mathcal{L}$ and $d\mathcal{H}_w$ respectively. It is possible to continue splitting up these exponentials in an analogous manner to obtain different engine types, including the four-stroke by separating out the hot and cold couplings. This result shows the dynamical equivalence of these different engine types at the end of each cycle. This implies that these engines will have the same steady states, and will also share the same transient behaviour in their approach to steady state operation. Note that this says nothing about the dynamics within the stroke, which might differ significantly – thus the engines are still distinct. This also means that the dynamical equivalence does not immediately imply a thermodynamic equivalence between the different engine types, since work and heat are not state variables. Nevertheless, the

net heat and work flows of the different engine types can be shown to be equivalent up to $\mathcal{O}(s^3)$ using a result called the symmetric rearrangement theorem [27].

Theorem 2. (*symmetric rearrangement theorem*)

Suppose we have time-symmetric couplings $\Omega(t)$, $\gamma_c(t)$ and $\gamma_h(t)$. Then a transformation of these constitutes a symmetric rearrangement if the transformed functions remain time symmetric and if the time integral of each is left unchanged. If we have such a symmetric rearrangement, then the heat and work flows into the system are left invariant under the transformation up to $\mathcal{O}(s^3)$.

Proof. See Appendix D of [27] by Uzdin, Levy and Kosloff. □

It can be seen that any Strang splitting of the continuous engine satisfies the conditions for the symmetric rearrangement theorem, which immediately implies that the heat and work flows of the continuous, two-stroke and four-stroke engines are equal provided the action is sufficiently small. An example demonstrating this is given in Fig. 2.8.

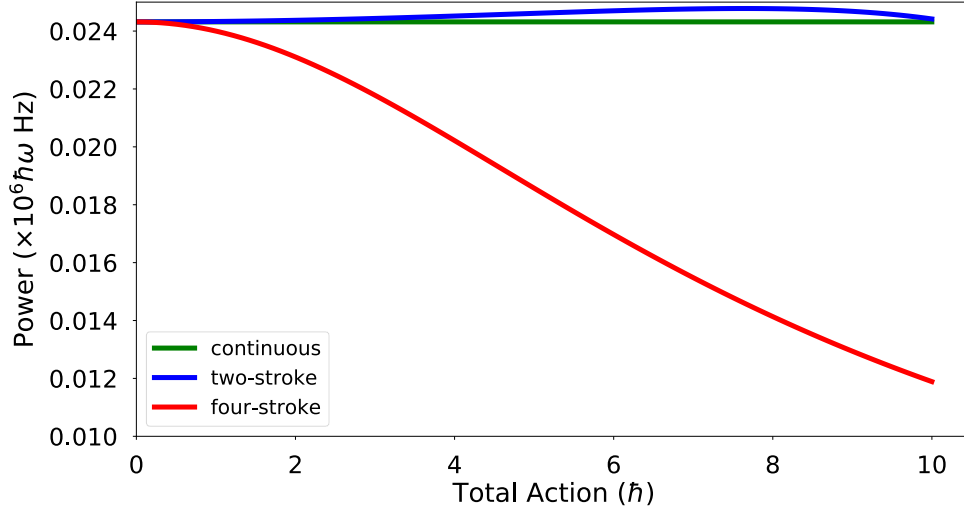


Figure 2.8: A numeric demonstration of the convergence in engine performance in the small action limit. The two-stroke and four-stroke duty cycles are 50% and 25% respectively. Here the temperatures are given by $\omega_h/kT_h = 1$ and $\omega_c/kT_c = 2$ for all engine types. The continuous coupling strengths are $\Omega = \gamma_h = \gamma_c = 0.5$ MHz, whilst the corresponding couplings for the two-stroke and four-stroke engines are 1 MHz and 2 MHz respectively. It can clearly be seen that the power outputs converge for actions less than \hbar .

2.2 The Nitrogen Vacancy Centre in Diamond

We choose the NV centre in diamond as our system to test for quantum heat machine equivalence (QHME) and the quantum thermodynamic signature (QTS). The NV centre is a crystal defect in diamond which has attracted a great deal of interest as a system for use in various quantum technologies, including as a qubit for quantum information processing (QIP) tasks, as a single photon source [42, 43], and finally for applications in quantum metrology where it has been used to make ultra-sensitive measurements of quantities such as temperature and magnetic fields [44, 45, 46, 47, 48]. We were already interested the NV centre in the context of quantum memories prior to this project, and it was the similarity between the memory and heat engine schemes

in the NV centre that first suggested the experiment. The reasons for this choice are as follows:

1. The NV centre provides us with a suitable level structure in the form of a spin triplet – these levels have long coherence lifetimes at room temperature, can be coherently controlled using convenient microwave frequencies, and can be shifted using an external magnetic field [49, 50, 51].
2. This spin triplet can be incoherently spin-pumped (net transfer of population between spin states resulting in a spin polarisation) using off-resonant optical excitation [52, 49].
3. In addition to spin pumping the ground state, the off-resonant optical excitation provides a sensitive means of reading out the ground state spin via a technique known as optically detected magnetic resonance (ODMR) [49, 42, 53].

The discrete level structure afforded by the spin triplet together with the fact that these states have long coherence times is important for this experimental implementation of a quantum heat engine. The incoherent optical pumping is also important for emulating the effect of a thermal coupling. Finally, the ODMR allows us to measure the performance of the engine, even when producing very low powers, and as a natural consequence of the thermalisation step. It is the combination of all three of these features that makes the NV^- a suitable test platform for this experiment. In the remainder of this section I will cover the essential properties and physics of the NV centre, as well as how it can be used to implement a heat engine.

2.2.1 Introduction to the NV centre

The NV centre consists of a substitutional nitrogen atom adjacent to a vacant site within the carbon lattice (see [54] for a detailed description of the diamond lattice). It can exist in one of two charge states, neutral and negative (and less often, positive); the negative centre has received the greater share of attention, largely due its QIP and metrology potential, whilst the NV^0 has generally considered ill suited to these applications due to its electronic structure. The two charged states can be distinguished by their different zero phonon lines (ZPL) of 637nm (NV^-) and 575nm (NV^0). The defect is produced either during the chemical vapour deposition (CVD) process of producing diamonds, or by radiating and annealing diamond which has a natural abundance of substitutional nitrogen. [49]

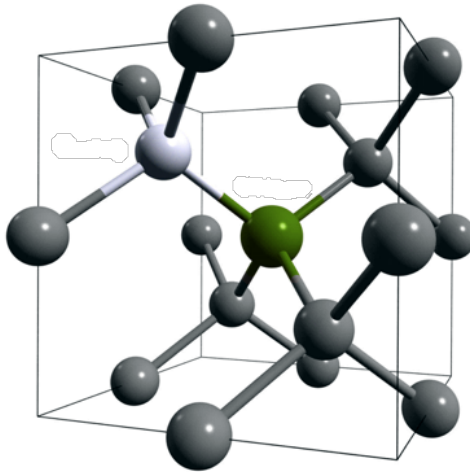


Figure 2.9: - geometric structure of the nitrogen vacancy centre: The NV consists of a substitutional nitrogen atom (green) and a vacant lattice site (grey) replacing two adjacent carbon atoms in the cubic diamond lattice.

2.2.2 Electronic structure

The electronic structure of the NV centre has been determined by combined experimental and theoretical studies, where the theoretical studies have made use of ab initio methods, as well as semi-empirical molecular models of deep level defects in semiconductors. Below I summarise the contents of Dr Jero Maze's thesis [55].

A defect in the crystal breaks the translational symmetry of the crystal, so that the full symmetry group of the crystal is reduced to a discrete point group (transformations which leave one point fixed – i.e rotations and reflections), which is some subset of the crystal point group. In the case of the NV centre this group is known as C_{3v} (or just the familiar dihedral group D_3). Due to this symmetry breaking, Bloch states are no longer a good approximation for electrons in the region of the defect; instead the states of interest are those which are localised in the vicinity of the defect. When the defect includes a vacancy, there are unpaired electrons in orbitals protruding into the vacancy, which are known as dangling bonds. The NV centre has four such orbitals, one from the Nitrogen and three from the Carbon atoms. These can be used to construct the leading order single electron orbitals by acting on them with the projection operators associated with the irreducible representations of C_{3v} . This yields three single electron wavefunctions denoted a_1 , e_x and e_y , lying within the band gap, with the degenerate e states lying at higher energy than the a . There is also an additional level, a'_1 which lies in the valence band, so that it is always occupied and does not contribute to the dynamics.

The negative NV centre has 6 electrons occupying these orbitals – one from each Carbon atom, two from the Nitrogen atom, and an additional electron contributed from substitutional Nitrogen atoms in the environment (or any other donors in the vicinity) – which requires it be described with multi-electron wavefunctions. Due

to there being 6 electrons in 8 possible states, it is simpler to describe the multi-electron states in terms of the two remaining 'holes'. An application of the group projection operators to these two electron wavefunctions yields combinations of the single electron wavefunctions which are the symmetry adapted basis states of the NV^- . There are 6 possible e^2 (in the hole picture) contributions, consisting of a triplet and 3 singlets, and 8 ae configurations, at a higher energy than the e^2 states, which consist of 2 triplets and 2 singlets.

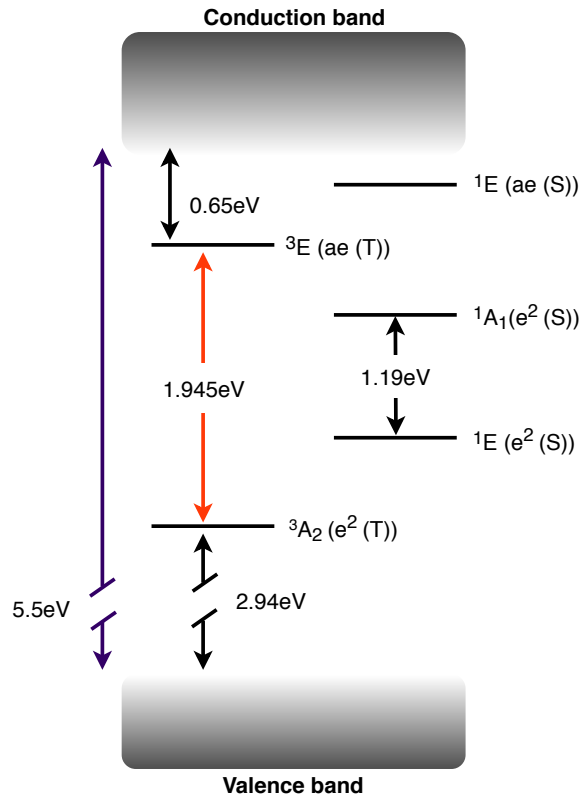


Figure 2.10: The energy level structure of the negative NV centre. The states on the left side are spin triplets (T), whilst those on the right are spin singlets (S), and the labels denote the orbital symmetry of the state.

All levels with the same molecular orbitals are degenerate prior to including electron-electron repulsion – the inclusion of this Coloumb interaction splits these states based on their orbital configurations. The resulting states and their ordering is shown in

Fig. 2.10; here the states are labeled according the irreducible representation of the C_{3v} (A_1, A_2 and E), with the corresponding single electron orbitals given in parenthesis together with the spin type, and the number to the left indicating the number of states (e.g there are six states in 3E as E is a two dimensional representation).

2.2.3 Ground state fine structure

We have not yet considered terms in the Hamiltonian that split states according to their spin component, nor interactions with external fields, so that states with the same orbital wavefunction and total spin are degenerate. The addition of such interactions raises this degeneracy, allowing us to observe the fine structure of the NV centre. Ordinarily the spin-orbit interaction provides the largest shift in those states which have orbital angular momentum; however the ground 3A_2 orbital state, given by $|e_x e_y - e_y e_x\rangle$, has zero angular momentum, with the result that the spin-orbit interaction has no effect on these states [49, 55]. Instead the resonance associated with the ground states, observed at 2.87GHz at zero field, can be attributed to the spin-spin interaction. This is given by,

$$H_{ss} = -\frac{\mu_0 g^2 \mu_B^2}{4\pi} \sum_{i < j} \frac{1}{r_{ij}^3} [3 (\vec{s}_i \cdot \hat{r}_{ij}) (\vec{s}_j \cdot \hat{r}_{ij}) - \hat{s}_i \cdot \hat{s}_j]$$

Because the ground states all share the same orbital wavefunction, one can trace out the orbital parts to be left with $\sum_{i,j} D^{ij} S_i S_j$, where D is a rank two tensor describing the spin-spin interaction Ref. [56, 55]. Of these terms, only the axial (z – aligned with the NV axis) component has a non-zero expectation value in the ground state. So if we write $D_{zz} = d_{gs}^{\parallel} = 2.87GHz$, we are left with,

$$H_{ss} = d_{gs}^{\parallel} S_z^2 \quad (2.20)$$

The effect of this term is to split the levels in the ground state, raising the ± 1 levels 2.87 GHz above the 0 spin-state. In addition to spin-spin and spin-orbit, one can consider hyperfine interactions with the nuclear spin of the substitutional Nitrogen, and with the Carbon-13 isotope if any are in the vicinity of the centre; I do not consider these interactions in detail here, as they are too weak (\sim MHz) for us to resolve in our experiment (as discussed below), and so play no role.

Finally we need to account for the effect of interactions with external fields, such as electric and magnetic fields, as well as strain in the diamond. Firstly the interaction of the centre with external magnetic fields is simply accounted for by the Zeeman interaction,

$$\begin{aligned} H_{\text{Zeeman}} &= \frac{\mu_B}{\hbar} \left(\vec{L} + g_{gs} \vec{S} \right) \cdot \vec{B} \\ &= \frac{g_{gs} \mu_B}{\hbar} \vec{S} \cdot \vec{B}, \end{aligned}$$

where $g_{gs} = 2.00232$ is the ground state Lande g factor, $\mu_B = 13.9964 \text{ GHz/T}$ is the Bohr magneton, and the orbital term vanishes in the ground state as discussed previously. To first order, both the electric field and strain act on the centre through the electric dipole operator, $\vec{d} = e\vec{r}$, via an interaction term of the form $(\vec{E} + \vec{\xi}) \cdot \vec{d}$, where \vec{E} is the electric field and $\vec{\xi}$ is the strain. Because the ground states share the same orbital wavefunction, this simply shifts them all relative to the other orbital states (the singlets and excited state manifold). If we include the effect of the electric field interaction on the spin (a second order effect similar in origin to the spin-orbit interaction), and trace out the orbital part, we obtain the following interaction term [49, 56]

$$\begin{aligned}
H_{\text{Stark}} = & d_{gs}^{\parallel} (E_z + \xi_z) \left[S_z^2 - \frac{1}{3} S(S+1) \right] + d_{gs}^{\perp} (E_x + \xi_x) (S_y^2 - S_x^2) \\
& + d_{gs}^{\perp} (E_y + \xi_y) (S_y S_x + S_x S_y)
\end{aligned}$$

The axial term is as before (Eq. 2.20), whilst the term d_{gs}^{\perp} is the perpendicular coupling coefficient. Although this interaction is not used explicitly in our experiment, I mention it because it is responsible for broadening of the ground state transitions due to varying strain in the crystal.

2.2.4 Excited state fine structure

Temperature plays an important role when it comes to discussing the fine structure of the excited states; this is because the details of the fine structure apparent at cryogenic temperatures are blurred out due to orbital averaging when working at room temperature [57, 49]. The six symmetry adapted states in 3E are given in Table 2.1.

Table 2.1: States in the 3E manifold. Here $E_{\pm} = ae_{\pm} - e_{\pm}a$, where $e_{\pm} = \mp(e_x \pm ie_y)$. Taken from Ref. [55].

$$\begin{aligned}
A_1 &= |E_{-}\rangle |\uparrow\uparrow\rangle - |E_{+}\rangle |\downarrow\downarrow\rangle \\
A_2 &= |E_{-}\rangle |\uparrow\uparrow\rangle + |E_{+}\rangle |\downarrow\downarrow\rangle \\
E_1 &= |E_{-}\rangle |\downarrow\downarrow\rangle - |E_{+}\rangle |\uparrow\uparrow\rangle \\
E_2 &= |E_{-}\rangle |\downarrow\downarrow\rangle + |E_{+}\rangle |\uparrow\uparrow\rangle \\
E_x &= i |E_{-} + E_{+}\rangle |\uparrow\downarrow + \downarrow\uparrow\rangle / 2 \\
E_y &= |E_{-} - E_{+}\rangle |\uparrow\downarrow + \downarrow\uparrow\rangle / 2
\end{aligned}$$

Low temperature

Unlike the ground states, the excited states have a non-trivial orbital angular momentum, and so the spin-orbit interaction does play a role in their structure. The spin-orbit interaction is a relativistic effect due to the motion of a charge through an electric potential, V , which is given by,

$$H_{SO} = (g - 1) \frac{\hbar}{2m^2c^2} (\nabla V \times \vec{p}) \cdot \vec{s}$$

In a system with full rotational symmetry, we can write $V = V(r)$, so that $\nabla V = \partial_r V \hat{\mathbf{r}}$. In this case the spin-orbit interaction is simply proportional to $\mathbf{L} \cdot \mathbf{S}$; however because of the reduced symmetry in the defect, it is given by [56],

$$\begin{aligned} H_{SO} &= \sum_{k=1}^2 \lambda_{xy} \left(\hat{l}_k^x \hat{s}_k^x + \hat{l}_k^y \hat{s}_k^y \right) + \lambda_z \hat{l}_k^z \hat{s}_k^z \\ &= \lambda_z (|A_1\rangle \langle A_1| + |A_2\rangle \langle A_2| - |E_1\rangle \langle E_1| - |E_2\rangle \langle E_2|) \end{aligned}$$

High temperature

Studies of the 3E fine structure at room temperature were only able to observe three states [58]. This was later shown to be a consequence of phonon mediated orbital averaging [59]. When the centre is excited into one of the 3E states, phonon interactions tend to distribute it into a equal statistical distribution of states with the correct spin projection, with the effective energy given by the average of the energies of the states with the same spin. The rate at which this redistribution occurs depends on the temperature – at low temperatures it is sufficiently slow compared to the 3E lifetime so as to have no effect; as the diamond approaches room temperature the rate increases to be significantly faster than the lifetime, so that there is a complete

redistribution prior decaying back to the ground state. The effective excited state Hamiltonian is then obtained by taking a partial trace over the orbital states. This results in a washing out of the spin-orbit part of the Hamiltonian, since the phonons act with the orbits, but leave the spin-spin interaction unmodified to first order.

$$H_{es} = D_{es} S_z^2$$

The axial spin-spin coupling in the excited state is now $D_{es} = 1.42\text{GHz}$ rather than 2.87GHz in the ground state. As with the ground state, we can consider the addition of terms coupling these states to external fields. The interaction Hamiltonian describing the Stark, Strain and Zeeman interactions is given by,

$$V_{es}^{(I)} = \frac{\mu_0 g_{es}}{\hbar} \vec{S} \cdot \vec{B} + d_{es}^{\parallel} (E_z + \xi_z) + f(\vec{\xi}) (S_y^2 - S_x^2) ,$$

where $f(\vec{\xi})$ is a function of the strain [59].

2.2.5 Optical Dynamics

The excited 3E state lies 1.945eV (637nm) above the lower 3A_2 state, which corresponds to a red optical transition. By illuminating the centre with 532nm (green) light, we excite the centre to the 3E phonon sideband (PSB). It then rapidly ($T_1 < 1\text{ps}$) decays from these excited vibrational states to the 3E ground vibrational state via phonon transitions. It is important to note that, although it preserves the spin state of the centre, this excitation is an incoherent process – this results from the random phase acquired by the centre during the phonon decay, due to its interaction with the Markovian phonon bath. This means that any coherence between two of the 3A_2 ground states is destroyed once the centre is excited to one of the 3E states in this manner. Because this is an incoherent process, we can model the dynamics of the

NV centre under off-resonant optical illumination using a simple rate equation model, taking only the populations into account.

Define the rate matrix, \mathcal{R} , to be such that the rate at which population is transferred from $|i\rangle$ to $|j\rangle$ is given by $\mathcal{R}_{ij}P_i$, where P_i is the population in the i^{th} state. Then the dynamics is given in terms of \mathcal{R} by,

$$d_t P_i = \sum_j \mathcal{R}_{ji}P_j - \sum_j \mathcal{R}_{ij}P_i$$

If we write the populations in a row vector, \mathbf{P} , the equation above can be written in matrix form as,

$$d_t \mathbf{P} = M\mathbf{P} \text{ , where } M_{ij} = \mathcal{R}_{ji} - \delta_{ij} \sum_k \mathcal{R}_{ik} \quad (2.21)$$

Because the phonon decays into the ground 3E vibronic state are so fast (\sim ps [49]), we can model the process of off-resonant optical excitation into 3E via the phonon sideband, as simply being a direct incoherent excitation from 3A_2 into 3E , and denote the rate by Γ . Once in the excited state manifold there are two possible decay routes back to the ground states: the first is directly through the fluorescent emission of an optical photon, in a spin-preserving decay. The second path consists of a non-radiative decay into the intermediate A_1 singlet, from which it rapidly ($T_1 < 1$ ns [42]) decays radiatively into the second lower lying singlets 1E , and finally from there back to the ground states via another non-radiative transition. Again, because the rate from A_1 to 1E is so fast, we model the three singlets as a single effective state [60, 61], which we denote by $|S\rangle$. A digram of the structure and the possible transitions is presented in Fig. 2.11. The resulting rate matrix for the NV centre is given by Eq. 2.22.

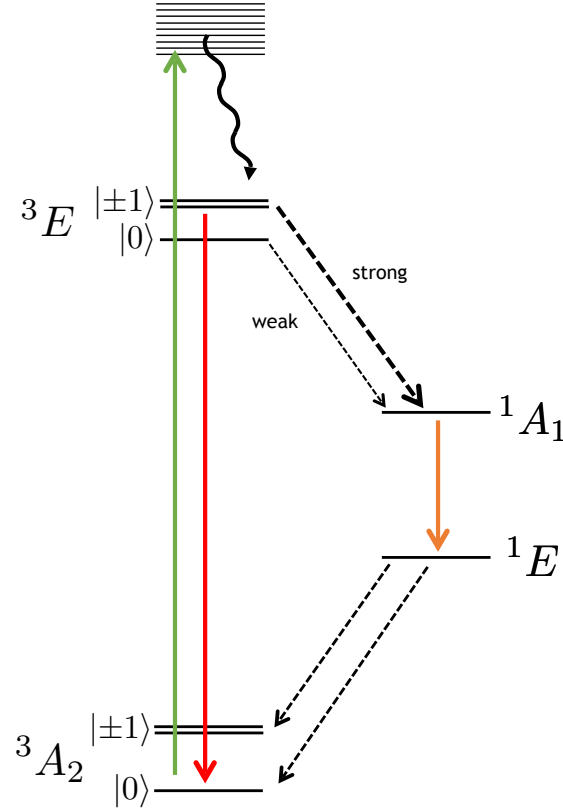


Figure 2.11: A schematic depicting the nature and strength of the transitions between the NV electronic states. Solid line denote optical transitions, whilst dotted transitions non-optical (phonon) transitions. The 3A_2 level is denoted by g in our model, 3E by e , and the states 1A_1 and 1E are treated as an effective singlet, s .

$$\mathcal{R} = \begin{bmatrix} 0_{3 \times 3} & \Gamma \mathbb{I}_{3 \times 3} & 0_{3 \times 1} \\ \gamma \mathbb{I}_{3 \times 3} & 0_{3 \times 3} & v \\ u & 0_{1 \times 3} & 0 \end{bmatrix} \quad (2.22)$$

Where we have used the basis $\{g_0, g_{-1}, g_1, e_0, e_{-1}, e_1, s\}$, and we have defined $v = (k_{0s} \ k_{1s} \ k_{1s})$ and $u = (k_{s0} \ \frac{1}{2}k_{s1} \ \frac{1}{2}k_{s1})$. The rate constants are given in Table. 2.2.

The resulting optical matrix M described the dynamics is given by,

Table 2.2: Spontaneous decay rates between NV levels used in the analysis [62]

	rate (MHz)
γ	65.9 ± 1.9
k_{1s}	53.3 ± 2.5
k_{0s}	7.9 ± 1.4
k_{s0}	0.98 ± 0.31
k_{s1}	0.73 ± 0.11

$$M = \begin{bmatrix} -\Gamma \mathbb{I}_{3 \times 3} & \gamma \mathbb{I}_{3 \times 3} & u \\ \Gamma \mathbb{I}_{3 \times 3} & -(\gamma \mathbb{I}_{3 \times 3} + \text{diag}(v)) & 0_{3 \times 1} \\ 0_{1 \times 3} & v & -\text{sum}(u) \end{bmatrix} \quad (2.23)$$

An examination of the numbers in Table. 2.2 shows that the second route through the intermediate singlets is not spin preserving, since all excited state spins are able to decay into the upper singlet; moreover, there is a strong preferential decay from the $|^3E\rangle \otimes |\pm 1\rangle$ states into the first singlet, as well as a slight preference for the 1E singlet to decay into the $|^3A_2\rangle \otimes |0\rangle$ ground state. The existence of the path through the singlets with a spin dependent branching ratio has two important consequences for us: the first is optical spin pumping of the ground state triplet, whilst the second is the provision of a method to optically readout the ground state populations.

2.2.6 Optical spin pumping

The first consequence of the branching ratio is that off-resonant optical excitation results in spin pumping of the ground state triplet. It can be seen that by cycling through this process several times, there is a net pumping into the $|0\rangle$ ground state due to the greater likelihood of an excited state of $|\pm 1\rangle$ decaying into the singlets, from

where it has near equal probability of decaying into $|0\rangle$ and $|\pm 1\rangle$. This can be shown analytically by solving for the steady state of the centre under optical illumination (the zero eigenvector of M). Denote the populations in the ground state triplet by G , those in the excited state triplet by E , and in the singlet by S . It is clear that there are three linearly independent zero-eigenvectors with all the population in the ground state if $\Gamma = 0$. In the case where $\Gamma \neq 0$, the steady state populations are given by:

$$G = \frac{1}{N(\Gamma)} \left[k_{s0} \left(1 + \frac{\gamma}{k_{0s}} \right), \frac{1}{2} k_{s1} \left(1 + \frac{\gamma}{k_{1s}} \right), \frac{1}{2} k_{s1} \left(1 + \frac{\gamma}{k_{1s}} \right) \right]^T \quad (2.24)$$

$$E = \frac{\Gamma}{N(\Gamma)} \left[\frac{\gamma k_{s0}}{k_{0s}}, \frac{\gamma k_{s1}}{2k_{1s}}, \frac{\gamma k_{s1}}{2k_{1s}} \right]^T \quad \text{and} \quad S = \frac{\Gamma}{N(\Gamma)},$$

Here we have defined $\alpha = k_{s0}/k_{0s} + k_{s1}/k_{1s}$, $\beta = k_{s0} + k_{s1}$, and the normalisation factor $N(\Gamma) = \Gamma(1 + \alpha) + \gamma\alpha + \beta$. Note that the ratios between the levels within a manifold (ground or excited), are independent of the pumping rate; all that adjusting Γ does is to shift population between the different manifolds. The total population in each manifold is plotted as a function of Γ in 2.12. This is no longer exactly true if there is any mixing between the states or if one includes thermalisation in the ground states, but both these rates are negligible compared to the rates being considered here [63, 52]. With this the percentage of the ground state population in $|0\rangle$ can be calculated to be,

$$\eta = \frac{G_0(\Gamma = 0)}{\sum G_i(\Gamma = 0)} = \frac{k_{s0} \left(1 + \frac{\gamma}{k_{0s}} \right)}{k_{s1} \left(1 + \frac{\gamma}{k_{1s}} \right)} \approx 0.85$$

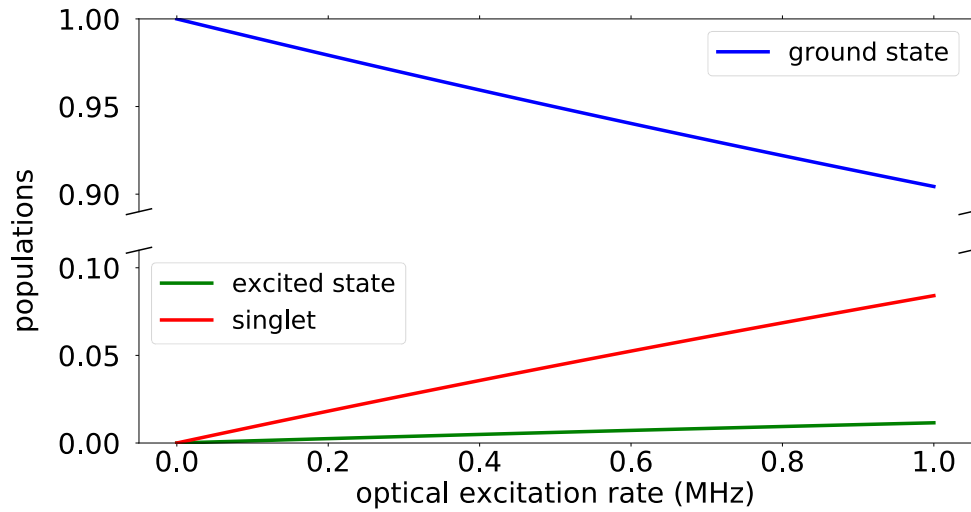


Figure 2.12: Manifold populations as a function of optical excitation rate

2.2.7 Optically detected magnetic resonance

The standard method used to probe microwave-separated spin states is known as electron spin resonance (ESR). ESR relies on measuring microwave absorption or reflection of microwaves directed at the sample. This technique has been a powerful tool since it was first invented at the end of the second world war (allowed by the advances made in MW technology due to RADAR). The technique does have a number of shortcomings: the first is that at room temperature, the Boltzman distribution between GHz separated levels results in near equal populations in each of the levels, so one needs to cool the sample down to cryogenic temperatures in order to obtain a spin polarisation that can be probed with resonant driving with microwaves. The second problem relates the sensitivity of the detection of microwaves – due both to a lack of high-efficiency detectors and the high level of blackbody background noise in this frequency range.

The existence of the branching ratio in the NV centre allows us to make use of a

different technique known as optically detected magnetic resonance (ODMR), which takes advantage of the fact that an NV centre starting in one of the $|\pm 1\rangle$ ground states is less likely to produce a fluorescence photon than one starting in $|0\rangle$ when excited into the 3E manifold, due to the larger branching to the singlet states. Thus we can expect a fluorescence contrast between different ground spin states under optical excitation, so that measuring the fluorescence allows us to determine the ground state spin. Fig. 2.13 shows a theoretical plot of the time resolved fluorescence for initial states $|\pm 1\rangle$ (red) and $|0\rangle$ (blue).

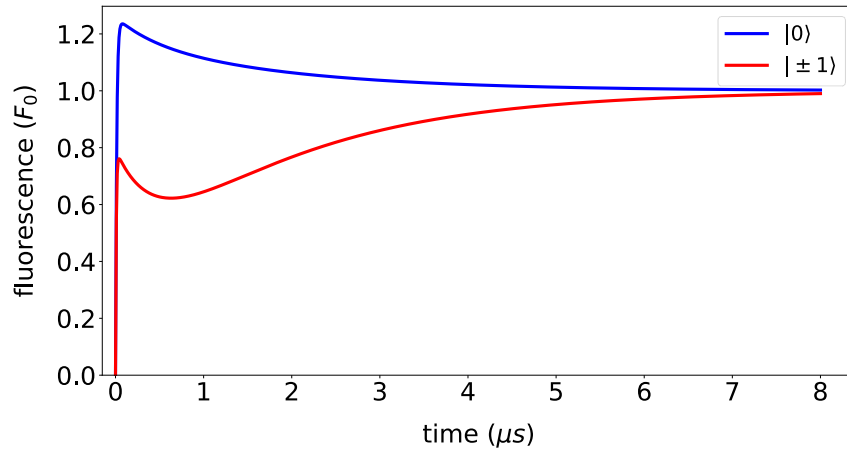


Figure 2.13: Normalised (to steady state fluorescence) fluorescence as a function of time for different starting states. A clear distinction can be seen between starting in the 0-spin state as opposed to the ± 1 -states. This example is plotted with $\Gamma = 1.0$ MHz.

It is clear that the fluorescence from $|0\rangle$ is initially significantly higher than $|\pm 1\rangle$, and then as the populations are redistributed, being pumped into $|0\rangle$, the fluorescence in each case approaches the steady state value. Fig. 2.14 simply shows the same data, but plotted as a difference in the fluorescence.

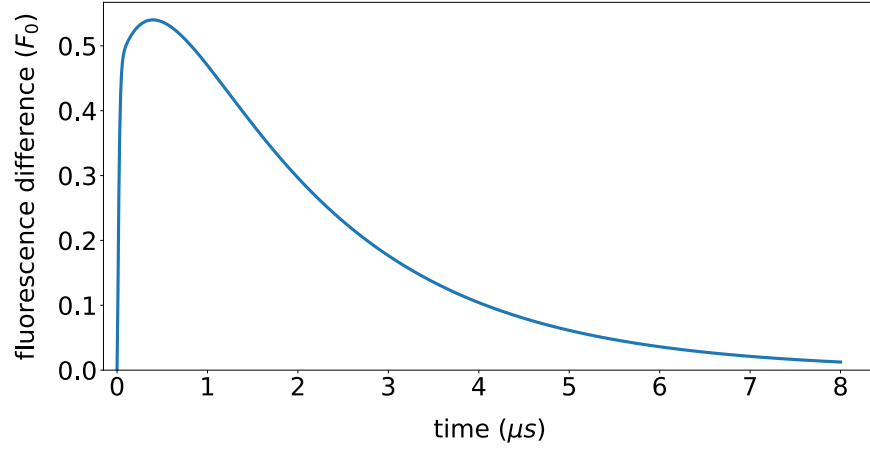


Figure 2.14: This shows the difference in fluorescence between starting states 0 and ± 1 normalised to the steady state fluorescence.

So by observing the fluorescence in the correctly gated window, we can tell (on average) the starting state of the centre.

2.2.8 Optical dynamics in a magnetic field

When we apply an external magnetic field to the centre, the zero-field states are mixed in addition to being shifted, which may change the transition rates between the new levels. We therefore need to determine how the rate matrix changes in these circumstances. Recall that the ground and excited state Hamiltonians at room temperature and in the presence of a magnetic field are given by,

$$H_{g(e)} = H_0^{g(e)} + \frac{\mu_0 g_{g(e)}}{\hbar} \vec{S} \cdot \vec{B},$$

where $H_0^{g(e)} = \text{diag}(0, D_{g(e)}, D_{g(e)})$, $D_g = 2.87\text{GHz}$, and $D_e = 1.42\text{GHz}$. By diagonalising each matrix, we are able to determine the eigenstates and their corresponding energies at a given magnetic field strength. Fig 2.15 is a plot of the effect of a magnetic field, orientated slightly off the NV axis.

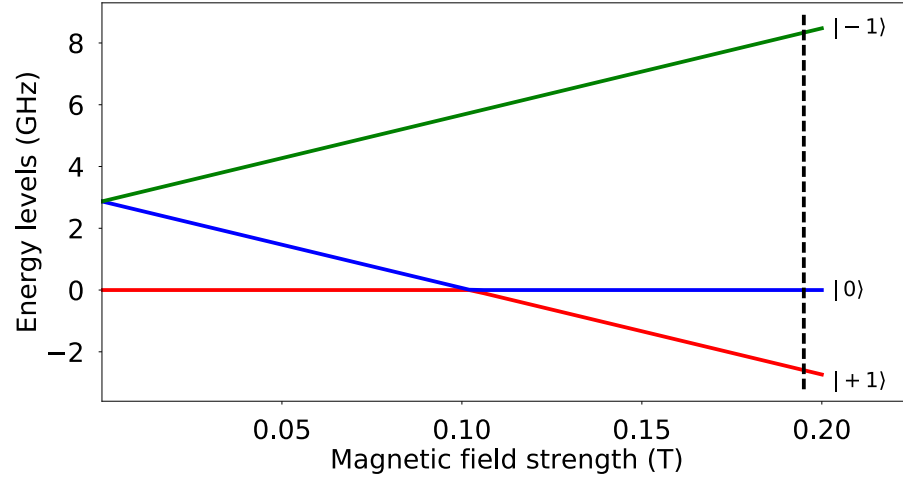


Figure 2.15: The ground state energy levels under an off-axial (1°) magnetic field.

Suppose that the initial basis states are $\{|\psi_i\rangle\}_i$ and that the transformed state vectors are $\{|\phi_i\rangle\}_i$, which are related to one another by unitary U :

$$|\phi_i\rangle = \sum_j U_{ij} |\psi_j\rangle$$

The contribution of state $|\psi_j\rangle$ to the population of the transformed state $|\tilde{\psi}_i\rangle$ is $|U_{ij}|^2$. Elements in the transformed rate matrix are then given by a sum over the zero-field rates, weighed by these factors. Then the elements of new rate matrix, $\tilde{\mathcal{R}}$, are simply given by the incoherent sum of the contributions of the original states to the transformed states [62]:

$$\tilde{\mathcal{R}}_{ij} = \sum_{k,l} |U_{ik}|^2 |U_{jl}|^2 \mathcal{R}_{kl}$$

$$\therefore \mathcal{R} \rightarrow |U|^2 \mathcal{R} |U^T|^2,$$

where $|U|^2$ denotes the element-wise absolute square. We can calculate the dynamics

of the centres under optical excitation as before by replacing the zero field \mathcal{R} with the transformed matrix above.

2.2.9 Ground state spin dynamics of the NV centre

As described previously, the NV centre has a spin-triplet ($S = 1$) ground state. As with any spin system it is characterised its spin lifetime (or inverse spin relaxation rate) T_1 , its homogeneous coherence time (inverse decoherence rate) T_2 , and in the case of an ensemble, the inhomogeneous coherence time T_2^* ($\leq T_2$). These rates are not fixed, but depend on a number of parameters, including the temperature of the diamond, the density of paramagnetic impurities (including other NV centres) in the neighbourhood of the centre, and the presence of strain and other external fields.

The spin relaxation time T_1 is largely determined by spin-phonon interactions, and so is strongly temperature dependent [52]. Measured values range from several milliseconds at room temperature, up to a few seconds at cryogenic temperatures [63, 52]. The homogeneous coherence time is dominated by spin-spin interactions with neighbouring paramagnetic defects [64]. In Type Ib diamond, this is principally due to substitutional Nitrogen atoms (N_s). The values measured for T_2 vary from $\mathcal{O}(1 - 10)\mu\text{s}$ [63, 64, 65, 66, 67] in dense type 1b samples, and up to 1.8 ms in isotopically pure and low nitrogen diamond [68]. Additionally, studies have shown that the ground state T_1 and T_2 times are independent of the magnetic field, provided we are away from any resonance (when the transition is resonant with a transition in some other paramagnetic impurity e.g. N_s at about 500 G) [63, 69]. Finally the inhomogeneous dephasing time (T_2^*) is strongly dependent on the sample in question, principally due to factors such as strain and impurity content.

In addition to the passive dynamics of the ground state spins, we can consider actively

driving these transitions. Because these states share the same orbital wavefunction, we cannot drive it using an electric dipole transition. However, because they have a non-zero magnetic dipole moment, we can drive it using the magnetic dipole transition, which arises from the Zeeman interaction term:

$$H_I(t) = \frac{\mu_0 g}{\hbar} \left(\vec{S} \cdot \vec{B}_0 \right) e^{i\omega t}$$

This term allows population to be transferred between the ground spin states by tuning microwave radiation to the frequency separating the states in question (for instance 2.87 GHz in the zero field case). This can be achieved for any states ψ_1 and ψ_2 such that $\langle \psi_2 | \vec{S} \cdot \vec{B}_0 | \psi_1 \rangle \neq 0$.

Chapter 3

Experiment

In this chapter we discuss how a quantum heat engine can be implemented using NV centres, and describe the experimental setup used to realise this implementation and test the theoretical results discussed previously. The ability to perform experiments of this nature has been allowed by relatively recent advances in quantum control and metrology. In particular, our experiment relies heavily on advances made in using NV centres for ultra-sensitive magnetic field sensing [44].

3.1 Heat Engines with NV centres

Recall that the NV centre has a number of special properties which have singled it out as of interest for various quantum technologies. These include the fact that exists in a solid state environment, but retains long coherence times in its ground state spin triplet, even at room temperature; the ground state spin-triplet can be spin-polarised using optical pumping; and the ground state populations can be sensitively read out using the same optical excitation as used for pumping. These properties suggest that the NV centre is an ideal platform to implement a quantum heat engine.

Our scheme relied on using the ground state triplet together with the lower lying

singlet of the NV centre as the system for our heat engine. Controllable coupling to thermal baths was emulated using the off-resonant optical pumping mechanism. Since the optical pumping transfers population into the $|0\rangle$, and because the action of the thermal coupling should produce an inversion, the ground states of the centre required reordering – this was done by applying a static axial magnetic field to shift the states such that $|0\rangle$ lay between $|\pm 1\rangle$ (Fig. 3.1). In this configuration, when the optical pumping is turned on, population is transferred from the upper and lower states, $|\pm 1\rangle$, to $|0\rangle$ via the singlet $|^1E\rangle$. It will be shown that this emulates a simultaneous thermal coupling to hot and cold reservoirs (Sec. 3.2). The resulting population inversion between $|0\rangle$ and $|+1\rangle$ can then be exploited to produce work in the form of microwave gain by driving this transition with resonant microwaves. Since this pumping mechanism is only able to effect the simultaneous coupling of both hot and cold reservoirs, only the continuous and 2-stroke engine types could be investigated with this setup. Finally, ODMR forms the basis for measuring the power output of this engine – it is the sensitivity of this technique that allows for the measurement of the small power outputs produced when the engine operates in the small action regime.

3.2 Emulation of the thermal action

An essential part of this thesis is the idea that the effect of coupling to a thermal reservoir can be emulated using off-resonant optical pumping. In this section this claim is justified and the method for extracting the effective thermal action is derived.

The approach taken here is to find a subset of the NV^- states, which generate a subspace S , together with a reduced evolution operator \mathcal{L} on S , which satisfies the

requirements for a thermal evolution operator. Let \mathcal{P} be a projection operator onto S . Then the condition we require of S and \mathcal{L} is,

$$e^{\mathcal{L}t}(\mathcal{P}\sigma) = \mathcal{P}(e^{Mt}\sigma) \quad \forall \sigma \in S \quad (3.1)$$

This condition is a statement that the thermal operator \mathcal{L} should describe the time evolution of the reduced state, when the evolution of the whole system is generated by the optical matrix M . Physically it means that if we only observe the population dynamics of the states in the subsystem, we should be unable to determine whether the dynamics is generated by the full optical matrix M on the whole system, or by \mathcal{L} acting on the subsystem alone. Note that, as defined here, \mathcal{L} differs from the previous definition by a factor of $i\hbar$ – this is done for convenience in this section, but we will revert to the former definition for consistency with the Schrödinger equation thereafter. Expanding the exponentials in Eq. 3.1 and examining the first order terms yields the following condition on \mathcal{L} :

$$(\mathcal{L}\mathcal{P} - \mathcal{P}M)|_S = 0$$

It is possible to attempt to solve this exactly, but doing so results in a \mathcal{L} which is far from population conserving. This is not surprising because in taking this restriction terms which transfer population from outside S back into S are completely ignored. This might seem to suggest that it is simply not possible to find an \mathcal{L} which satisfies 3.1, even approximately. However, if the terms in M which are responsible for returning population into the subsystem are sufficiently large, then even a small amount of population in the orthogonal complement of S will change the dynamics substantially,

and can make it possible to find a good approximation.

Suppose M has an eigen-decomposition $\{\lambda_i, \psi_i\}_{i=1}^n$. Then a suitable \mathcal{L} can be found if it is possible to find $m = \dim(S)$ eigenvectors $\{\psi_{i_j}\}_{j=1}^m$ such that $(\mathcal{P} - \mathbb{I}) \psi_{i_j} \approx 0$ for $j = 1, \dots, m$, and further such that $\{\mathcal{P}\psi_{i_j}\}_{j=1}^m$ and $\{(\mathcal{P} - \mathbb{I}) \psi_{i_j}\}_{j=m+1}^n$ are independent. The idea is that, if $\{\psi_{i_j}\}_{j=1}^m$ are nearly in S , the subspace they generate can be used in place of S in condition 3.1.

$$e^{\mathcal{L}t} (\mathcal{P}\psi_i) = \mathcal{P} (e^{Mt}\psi_i), \quad i = 1, \dots, m \quad (3.2)$$

Again equating the first order terms yields,

$$(\mathcal{L}\mathcal{P} - \mathcal{P}M) \psi_i = 0 \text{ for } i = 1, \dots, m$$

By virtue of $\{\psi_i\}_{i=1}^m$ being eigenvectors of M , it can be seen that this simply reduces to,

$$[\mathcal{L} - \lambda_i \mathbb{I}] (\mathcal{P}\psi_i) = 0$$

This is simply a statement that \mathcal{L} has eigenvectors $\{\mathcal{P}\psi_i\}_{i=1}^m$ and corresponding eigenvalues $\{\lambda_i\}_{i=1}^m$. Since there are m eigenvector/eigenvalue pairs this completely determines \mathcal{L} on S ; it is then simply required that it be zero on the orthogonal complement of S . It can also be seen that this is sufficient to satisfy Eq. 3.2.

Given an operator \mathcal{L} calculated in this manner, it still needs to be shown that it closely approximates a thermal operator, and also that it satisfies Eq. 3.1 to a good degree. We begin with the later: suppose $\psi \in S$ and that the eigen-pairs are ordered

such that $\|(\mathcal{P} - \mathbb{I})\psi_i\| = \epsilon_i \ll 1$ for $i = 1, \dots, m$, where $m = \dim(S)$. Further, let ψ have eigen-expansion,

$$\psi = \sum_{k=1}^m \alpha_k \psi_k + \sum_{l=m+1}^n \beta_l \psi_l$$

Since $\psi \in S$, we can write $\beta_l \sim \mathcal{O}(\epsilon)$, where $\epsilon = \max\{\epsilon_i \mid i = 1, \dots, m\}$:

$$0 = (\mathcal{P} - \mathbb{I})\psi = \sum_{k=1}^m \alpha_k (\mathcal{P} - \mathbb{I})\psi_k + \sum_{l=m+1}^n \beta_l (\mathcal{P} - \mathbb{I})\psi_l$$

$$\therefore \sum_{l=m+1}^n \beta_l (\mathcal{P} - \mathbb{I})\psi_l \sim \mathcal{O}(\epsilon) \implies \beta_l \sim \mathcal{O}(\epsilon)$$

So ϵ_l can be written in place of β_l . Since $\{\mathcal{P}\psi_i\}_{i=1}^m$ is a basis for S (by assumption), it is possible to write,

$$\mathcal{P}\psi_l = \sum_{k=1}^m \omega_{lk} \mathcal{P}\psi_k, \quad l = m+1, \dots, n$$

Then,

$$\begin{aligned} \therefore (e^{\mathcal{L}t} \mathcal{P} - \mathcal{P} e^{Mt}) \psi &= \sum_{k=1}^m \sum_{l=m+1}^n \epsilon_l \omega_{lk} (e^{\lambda_k t} - e^{\lambda_l t}) \mathcal{P}\psi_k \\ &= \sum_{k=m+1}^n \epsilon_k (e^{\mathcal{L}t} - e^{\lambda_k t}) \mathcal{P}\psi_k \sim \mathcal{O}(\epsilon) \end{aligned}$$

Here the fact that $\lambda_i \leq 0$ for all i and ψ is normalised has been used. So it can be seen that, when derived this way, \mathcal{L} does satisfy Eq. 3.1 approximately. Note that the resulting matrix need not be exactly population conserving unless $(\mathcal{P} - \mathbb{I})\psi_i = 0$

for $i = 1, \dots, m$. Note that if $(\mathcal{P} - \mathbb{I}) \psi_i = 0$ is only satisfied approximately, then population conservation can be imposed manually, modifying \mathcal{L} by the minimal amount required to obtain the thermal evolution operator sought. A means of doing this for a subsystem with N states ($N=4$ in our case) is via the following procedure:

```

for ( $n = 0$ ;  $n < N$ ;  $n \leftarrow n + 1$ ) do

     $S \leftarrow 0$ 
    create priority queue  $Q$ 

    for ( $m = 0$ ;  $m < N$ ;  $m \leftarrow m + 1$ ) do
        if ( $m \neq n$ ) then
             $\mathcal{L}_{mn} \leftarrow \max \{0, \mathcal{L}_{mn}\}$ 
             $S \leftarrow S + \mathcal{L}_{mn}$ 
             $Q.\text{enqueue}(\mathcal{L}_{mn})$ 
        else
             $\mathcal{L}_{mn} \leftarrow \min \{0, \mathcal{L}_{mn}\}$ 
        end if
    end for

    while ( $(1+Q.\text{size}()) Q.\text{top}() < \mathcal{L}_{nn} + S$ ) do
         $q \leftarrow Q.\text{dequeue}()$ 
         $S \leftarrow S - q$ 
         $q \leftarrow 0$ 
    end while

     $\Delta\mathcal{L} \leftarrow (\mathcal{L}_{nn} + S) / (Q.\text{size}() + 1)$ 
     $\mathcal{L}_{nn} \leftarrow \mathcal{L}_{nn} - \Delta\mathcal{L}$ 

    for ( $q$  in  $Q$ ) do
         $q \leftarrow q - \Delta\mathcal{L}$ 
    end for

end for

```

This simply scans down each column, initially ensuring that the elements are the correct sign by setting them to zero if not, and then adding the off-diagonal elements to

a priority queue, as well as summing them up. At this point it would seem natural to simply subtract the median value off each element; however it needs to be checked that this does not result in elements acquiring the wrong sign – this is achieved by the while loop in the middle, which sets these elements to zero and removes them from the queue. Only then is the median subtracted from the remaining elements.

The preceding discussion has been quite heuristic, so we now apply it to the NV centre under off-resonant optical excitation, and show that it does produce the desired results. Recall that the optical matrix is given by 2.23.

$$M = \begin{bmatrix} -\Gamma \mathbb{I}_{3 \times 3} & \gamma \mathbb{I}_{3 \times 3} & u \\ \Gamma \mathbb{I}_{3 \times 3} & -(\gamma \mathbb{I}_{3 \times 3} + \text{diag}(v)) & 0_{3 \times 1} \\ 0_{1 \times 3} & v & -\text{sum}(u) \end{bmatrix}$$

Further recall that the zero-eigenvector is given by 2.24. Perturbation theory can be used to determine the other eigenvectors as a function of Γ . Ordinarily the matrices to which perturbation theory is applied are hermitian or symmetric; however $M(\Gamma)$ is neither symmetric nor hermitian, which requires a slight modification to the usual formulae used in perturbation theory in quantum mechanics. Additionally, the expansion is taken about $\Gamma = 0.5$ MHz rather than $\Gamma = 0$ MHz, since it lies nearer the centre of the range used in the experiment. The zeroth order eigenvalues (in MHz) and their corresponding eigenvectors (given by the columns) are,

$$\lambda^{(0)} = [0.0 , -0.15 , -0.22 , -1.84 , -74.28 , -119.47 , -119.48]$$

$$\sigma^{(0)} = \begin{bmatrix} 0.99 & 0.84 & 0.00 & -0.46 & -0.66 & 0.00 & 0.00 \\ 0.09 & -0.38 & 0.71 & -0.19 & 0.00 & -0.10 & 0.45 \\ 0.09 & -0.38 & -0.71 & -0.19 & 0.00 & -0.43 & -0.11 \\ 0.01 & 0.01 & 0.00 & 0.00 & 0.74 & 0.00 & 0.00 \\ 0.00 & 0.00 & 0.00 & 0.00 & 0.00 & 0.18 & -0.82 \\ 0.00 & 0.00 & 0.00 & 0.00 & 0.00 & 0.77 & 0.19 \\ 0.06 & -0.08 & 0.00 & 0.85 & -0.08 & -0.43 & 0.29 \end{bmatrix}$$

Note that the first four eigenvectors are of exactly the form for which we are looking – they describe changes in the ground state triplet and the singlet, and their excited state components are negligible compared to the other components. Finally, note that if we restrict our attention to the ground state triplet together with the singlet, then the first four vectors form a linearly independent set spanning these states; and similarly so with the second set and the excited state triplet. This suggests that the effective system should be taken to consist of the ground states together with the singlet. If the states are ordered according to their relative energy, the corresponding projection operator is $\mathcal{P} = \mathbb{I}_{4 \times 4} \oplus 0_{3 \times 3}$. To see that this is not just true for $\Gamma = 0.5$ MHz, consider the first and second order perturbative corrections; which are given by,

$$\lambda^{(1)} = [0.0, -0.28, -0.45, -0.27, -0.89, -0.55, -0.55]$$

$$\sigma^{(1)} = \begin{bmatrix} -0.10 & 0.08 & 0.00 & 0.05 & 0.00 & 0.00 & 0.00 \\ -0.01 & 0.04 & 0.00 & -0.02 & 0.00 & -0.16 & -0.04 \\ -0.01 & 0.04 & 0.00 & -0.02 & 0.00 & 0.04 & -0.17 \\ 0.01 & 0.01 & 0.00 & -0.01 & 0.00 & 0.00 & 0.00 \\ 0.00 & 0.00 & 0.01 & 0.00 & 0.00 & 0.29 & 0.07 \\ 0.00 & 0.00 & -0.01 & 0.00 & 0.00 & -0.07 & 0.31 \\ 0.10 & -0.16 & 0.00 & 0.00 & 0.00 & -0.10 & -0.17 \end{bmatrix}$$

$$\lambda^{(2)} = [0.00 , 0.02 , 0.00 , -0.02 , 0.00 , 0.00 , 0.00]$$

$$\sigma^{(2)} = \begin{bmatrix} 0.01 & 0.00 & 0.00 & 0.00 & 0.00 & 0.00 & 0.00 \\ 0.00 & 0.00 & 0.00 & 0.00 & 0.00 & 0.07 & 0.02 \\ 0.00 & 0.00 & 0.00 & 0.00 & 0.00 & -0.02 & 0.08 \\ 0.00 & 0.00 & 0.00 & 0.00 & 0.00 & 0.00 & 0.00 \\ 0.00 & 0.00 & 0.00 & 0.00 & 0.00 & -0.13 & -0.03 \\ 0.00 & 0.00 & 0.00 & 0.00 & 0.00 & 0.03 & -0.14 \\ -0.01 & 0.00 & 0.00 & 0.00 & 0.00 & 0.05 & 0.08 \end{bmatrix}$$

This demonstrates that substance of the previous discussion does indeed still hold provided $\Delta\Gamma = \Gamma - 0.5$ is not too large (in practise we have $|\Delta\Gamma| \leq 0.5$).

If \mathcal{L} only needs to be determined for a single value of Γ , then one need simply calculate the eigenvalues and eigenvectors of $M(\Gamma)$, and define the change of basis matrix, U , to be that with columns $\mathcal{P}\sigma_i(\Gamma)$ for $i = 0, 1, 2, 3$. If $D \equiv \text{diag}(\lambda_0, \lambda_1, \lambda_2, \lambda_3)$, then,

$$\mathcal{L}(\Gamma) = U D(\Gamma) U^{-1}$$

On the other hand, if \mathcal{L} needs to be calculated for many values of Γ , then this can be a costly calculation. Note the following: if $X(t) = X_0 + tX_1 + t^2X_2 + \mathcal{O}(t^3)$ and X is invertible for all $t > 0$, then $X^{-1}(t) = Y_0 + tY_1 + t^2Y_2 + \mathcal{O}(t^3)$, where:

$$Y_0 = X_0^{-1}$$

$$Y_1 = -Y_0 X_1 Y_0$$

$$Y_2 = -Y_0 X_1 Y_1 - Y_0 X_2 Y_0$$

So instead of diagonalising and inverting the matrix from scratch for each value of Γ , it is possible to use the perturbative expansion to calculate $D(\Gamma)$ and $U(\Gamma)$, and use this procedure to determine $U^{-1}(\Gamma)$. Then

$$\begin{aligned} \mathcal{L}(0.5 + \Delta\Gamma) &= U(\Delta\Gamma) D(\Delta\Gamma) U^{-1}(\Delta\Gamma) \\ &= \mathcal{L}_0 + \Delta\Gamma \mathcal{L}_1 + \mathcal{O}(\Delta\Gamma^2) \end{aligned}$$

where,

$$\mathcal{L}_0 = \begin{bmatrix} -0.05 & 0.00 & 0.00 & 0.97 \\ 0.00 & -0.22 & 0.00 & 0.36 \\ 0.00 & 0.00 & -0.22 & 0.36 \\ 0.05 & 0.22 & 0.22 & -1.71 \end{bmatrix}$$

$$\mathcal{L}_1 = \begin{bmatrix} -0.11 & 0.00 & 0.00 & -0.01 \\ 0.00 & -0.45 & 0.00 & 0.00 \\ 0.00 & 0.00 & -0.45 & 0.00 \\ 0.11 & 0.45 & 0.45 & 0.00 \end{bmatrix}$$

These matrices can then be stored and used to calculate the series when $\mathcal{L}(\Gamma)$ is needed. It can also be seen that these matrices are very nearly population conserving, but nonetheless, once \mathcal{L} has been calculated, this can be ensured using the previously described procedure.

Now consider the nature of the thermal reservoirs and couplings to which this thermal matrix corresponds. First notice that all the couplings are between the ground states and the singlet, with no couplings between states within the ground triplet. Also, because the energy difference between the ground manifold and the singlet is expected to be much greater than the differences within the ground manifold (~ 89 THz vs ~ 3 GHz) [53], the effective temperature and coupling between the $|\pm 1\rangle$ states and the singlet is effectively the same. Further, by examining the ratios of the rates, it can be seen that the effective temperature between the singlet and $|0\rangle$ is less than that between the singlet and $|\pm 1\rangle$. So we are left with the picture in Fig. 3.1.

Suppose that the energy gap between the ground manifold and 1E is denoted by ΔE . Then the effective temperatures are simply given by 3.3 and are plotted as a function of the optical excitation rate in Fig. 3.2.

$$T_c \simeq \frac{\Delta E}{k} \frac{1}{\ln(17.63/\Gamma)} \quad \text{and} \quad T_h \simeq \frac{\Delta E}{k} \frac{1}{\ln(1.63/\Gamma)} \quad (3.3)$$

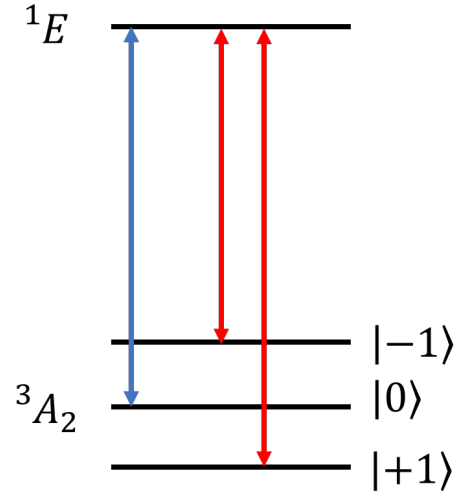


Figure 3.1: The effective system together with couplings to thermal baths. Here red denotes a coupling to the hot bath, whilst blue denotes a coupling to the cold bath.

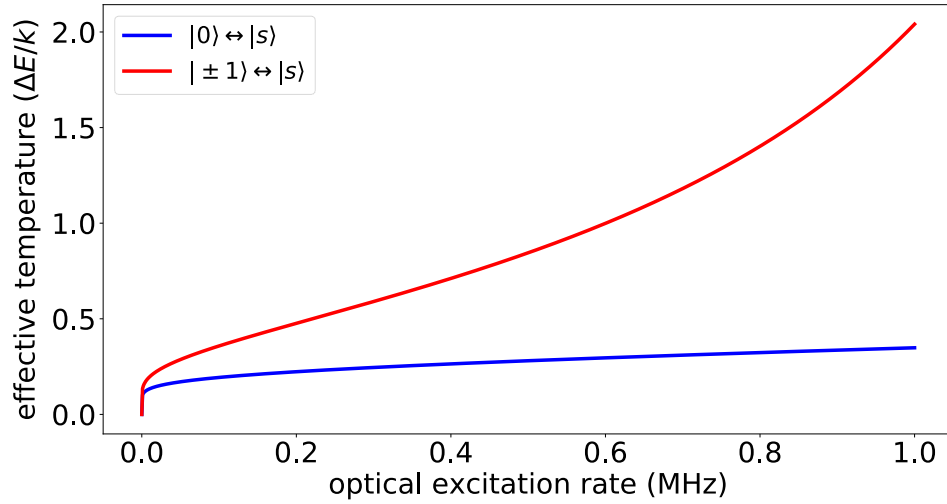


Figure 3.2: The effective temperatures of the reservoirs as a function of the pumping rate. Note that the units are $\Delta E/k$.

The measure of the extent to which the thermal action generated in this way is approximated by the optical cycle in the NV centre is given by 3.1. This strongly depends on the portion of the population sitting in the excited state manifold. In the

following figures I plot $e^{Lt}(\mathcal{P}\sigma)$ and $\mathcal{P}(e^{Mt}\sigma)$ for different starting states σ . Fig. 3.3 $\Gamma = 0.5$ MHz and a starting state of $(0.4, 0.5, 0, 0.01, 0, 0, 0.09)$, whilst Fig. 3.4 has the same optical excitation rate ($\Gamma = 0.5$ MHz), and equal populations in each of the ground states and singlet, whilst zero population in the excited states.

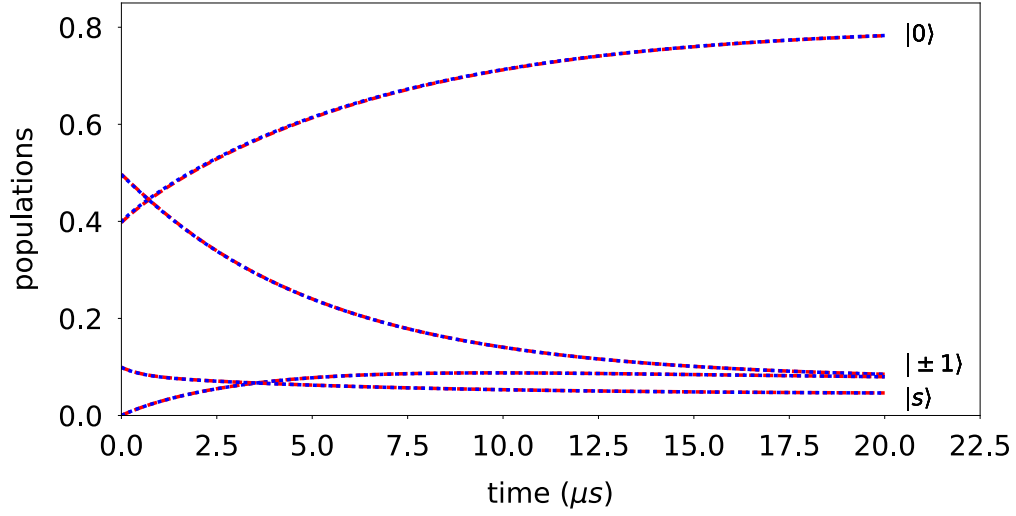


Figure 3.3: Evolution of a state with the full rate matrix (blue) vs the effective thermal action (red)

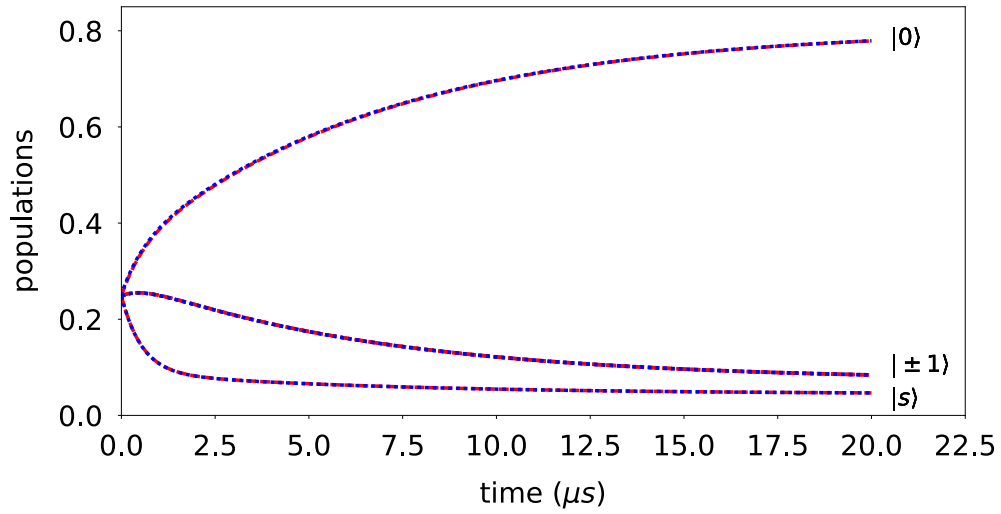


Figure 3.4: Evolution of a state with the full rate matrix (blue) vs the effective thermal action (red)

The deviation is too small to see effectively in these graphs, so the norm of the difference between the two vectors is plotted as a function of time and optical excitation rate in Fig. 3.5, again for a starting state with equal populations in each of the ground states and the singlet, and 0.3% in the excited state.

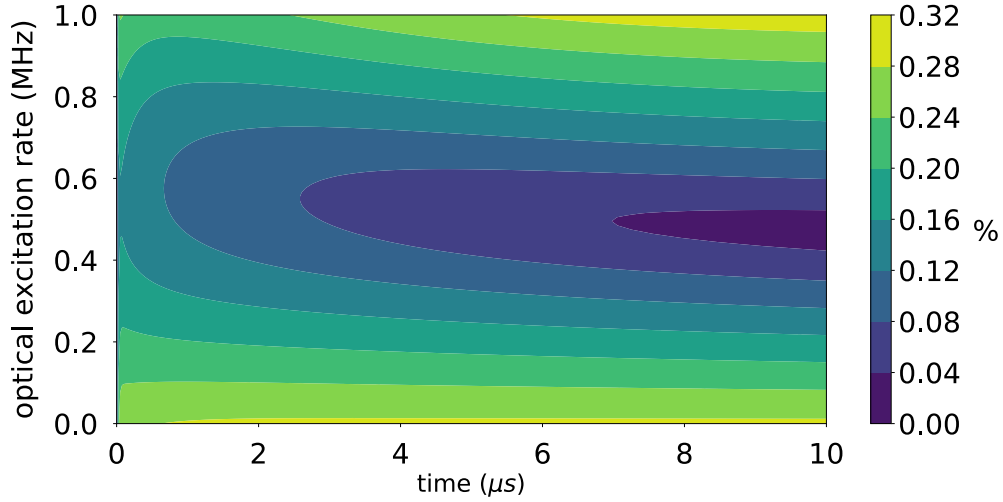


Figure 3.5: Plot of $\|(e^{Lt}\mathcal{P} - \mathcal{P}e^{Mt})\sigma\|^2$ expressed in %

These show that the population dynamics of the states in the subsystem under the full matrix M is very well approximated by those of the subsystem under \mathcal{L} , provided the population in the excited state manifold is close to the steady state population. Finally, and perhaps more importantly, it is also possible to compare simulations of the engine power output when using the full optical matrix (what we have in the laboratory) to that using \mathcal{L} (what we are emulating). This no longer suffers from the problem of having to place population in the excited state in an ad hoc manner. Fig. 3.6 compares the relative difference between these two powers for a range of Rabi frequencies and optical excitation rates.

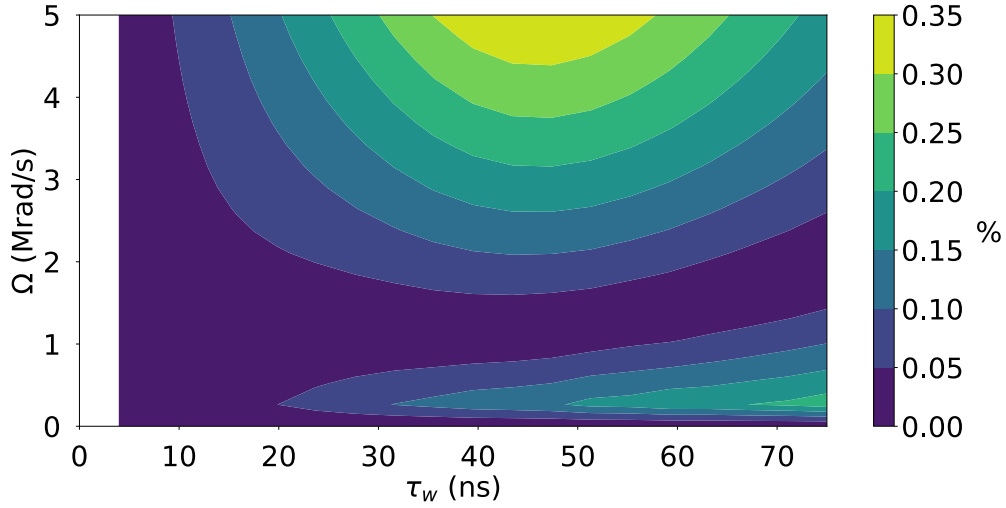


Figure 3.6: Difference in power output between the engines with the full optical matrix and thermal matrix. The quantity plotted is $2|p_1 - p_2| / |p_1 + p_2|$ expressed as a percentage.

The above analysis therefore does allow for us to conclude that, provided the optical excitation rate is not too large, the optical cycle in the NV^- centre does approximate thermal Markovian dynamics between the ground states and singlet to a very good degree.

Up to this point only the effect of the thermal baths (or optical dynamics) on the populations, or equivalently the diagonal elements of the density matrix, of the levels of the NV centre have been considered. The fact that the optical dynamics of the system can be described in this manner using a rate matrix acting on the populations alone, is an essential feature for correctly emulating the thermal action. However, when describing the heat engine, the action of the thermal action on the coherences of the density matrix also need to be taken into account. This is done quite simply in this system by adding in a phenomenological decay term for the ground state coherences at a rate Γ ; because only the coherences between the states we are driving ($|0\rangle \leftrightarrow |1\rangle$ here) need to be taken into account – this corresponds to adding a block

$(-\Gamma) \mathbb{I}_2$ to the matrix \mathcal{L} . The full thermal matrix is then given by,

$$\mathcal{L} = (-\Gamma \mathbb{I}_2) \oplus \mathcal{L}_{pop}$$

3.3 Converting Fluorescence Change into Power

It was previously stated that the power output of the NV heat engine could be determined by monitoring the fluorescence emission; this approach is based on the ability to make all optical measurements of the ground state populations in the NV centre, using ODMR. This can be formalised using the rate equation model, and allows for all the necessary measurements in the experiment.

Let σ be a vector whose elements are the populations in the various levels. Then given some rate, $R(t)$, at which population is transferred from the $|0\rangle$ to the $|1\rangle$ ground states, through some mechanism other than optical excitation, the equation describing the system is:

$$\partial_t \sigma = M\sigma + R(t)\nu,$$

where $\nu = [-1 \ 1 \ 0 \cdots 0 \ 0]^T$. The rate R is the quantity we wish to determine from the experimentally measured fluorescence, which derives from the interaction of the microwaves with the ground state levels. Although this is an inherently quantum process, we are only interested in determining the net rate of population transfer arising from the interaction, not in the details of the mechanism by which it occurs. Let $\Phi(t)$ be the fundamental matrix solution (a matrix which satisfies the differential equation – akin to the unitary evolution operator for the Schrodinger equation in standard QM) for the homogeneous equation; then it can be checked that the following is a solution to the inhomogeneous equation:

$$\sigma(t) = \Phi(t, t_0)\sigma_0 + \int_{t_0}^t d\tau \Phi(t, \tau)R(\tau)\nu, \quad (3.4)$$

where $\Phi(t, \tau) = \Phi(t)\Phi(\tau)^{-1}$. We take $R(t)$ to be periodic with the same period as that of $M(t)$, since $R(t)$ results from pulsed microwaves at the same rate as the laser pulses – this follows quite generally from Floquet theory and physical considerations. To proceed we need to find the state at the start of the cycle, σ_0 , during this steady state operation. Using the periodicity of the solution we have:

$$\begin{aligned} \sigma_0 = \sigma(T) &= \Phi(T)\sigma_0 + \int_0^T d\tau \Phi(T, \tau)R(\tau)\nu \\ \therefore [\mathbb{I} - \Phi(T)]\sigma_0 &= \int_0^T d\tau \Phi(T, \tau)R(\tau)\nu \end{aligned} \quad (3.5)$$

We would like to invert this to obtain σ_0 ; however the matrix on the LHS is singular. Note that $\Phi(T)$ is diagonalisable (with inverse $\Phi(-T)$), which allows us to write $(\mathbb{I} - \Phi(T)) = UDU^\dagger$ where D is diagonal. We define the pseudo-inverse, $(\mathbb{I} - \Phi(T))^+ = VD^+U^\dagger$, where the diagonal matrix D^+ is given by:

$$D_{ii}^+ = \begin{cases} 1/D_{ii} & \text{if } D_{ii} \neq 0 \\ 0 & \text{otherwise} \end{cases}$$

Let $\mathcal{A} = (\mathbb{I} - \Phi(T))^+$. A solution to equation 3.5 is then given by:

$$\tilde{\sigma}_0 = \mathcal{A} \int_0^T d\tau \Phi(T, \tau)R(\tau)\nu$$

The full space of solutions to 3.5 is then generated by $\alpha\rho_0 + \tilde{\sigma}_0$ for $\alpha \in \mathbb{R}$, where ρ_0 is

the (unique) zero eigenvector. We show that $\text{sum}(\tilde{\sigma}_0) = 0$: Suppose $\{\rho_i\}$ are the eigenvectors of $\Phi(T)$ with corresponding eigenvalues $\{\lambda_i\}$ (Again let ρ_0 be the unique eigenvector with eigenvalue 1). Then by virtue of $\Phi(T)$ being population preserving we have,

$$\text{sum}(\Phi(T)\rho_i) = \lambda_i \text{sum}(\rho_i) = \text{sum}(\rho_i),$$

which implies $\text{sum}(\rho_i) = 0$ for $i \geq 1$. Then given a vector ω , $\text{sum}(\omega) = 0 \implies \omega \in \text{span}(\rho_1, \dots, \rho_n)$. It is also clear that $\text{Im}(\mathcal{A}) \subseteq \text{span}(\rho_1, \dots, \rho_n)$. Finally notice that the RHS of 3.5 sums to zero. The unique normalised solution, σ_0 , to 3.5 is therefore simply obtained by setting $\alpha = 1$ (assuming we have normalised ρ_0). Substituting this back into 3.4, we have,

$$\begin{aligned} \sigma(t) &= \Phi(t, 0)\rho_0 + \Phi(t, 0) \mathcal{A} \int_0^T d\tau R(\tau)\Phi(T, \tau)\vec{\nu} + \int_0^t d\tau R(\tau)\Phi(t, \tau)\nu \\ \therefore \sigma(t) - \rho(t) &= \Phi(t, 0) \mathcal{A} \int_0^T d\tau R(\tau)\Phi(T, \tau)\vec{\nu} + \int_0^t d\tau \Phi(t, \tau)R(\tau)\nu \end{aligned}$$

where ρ is the state evolution when $R = 0$. We define the excited state population projector to be the vector $\zeta = [0, 0, 0, 1, \dots, 1, 0]$, so that the fluorescence from a state ρ is proportional to $\zeta \cdot \rho(t)$. Let $F(t)$ be the time dependent fluorescence with driving and $F_0(t)$ that without driving, and further define

$$\begin{aligned} g(t, \tau) &= \zeta \cdot \Phi(t, 0) \mathcal{A} \Phi(T, \tau) \cdot \nu \\ f(t, \tau) &= \zeta \cdot \Phi(t, \tau) \cdot \nu \end{aligned}$$

$$\therefore \frac{\zeta \cdot \rho_0}{F_{cw}} \times (F(t) - F_0(t)) = \int_0^T d\tau g(t, \tau)R(\tau) + \int_0^t d\tau f(t, \tau)R(\tau)$$

The fraction on the LHS is the proportionality constant linking the fluorescence to the excited state population – F_{cw} is the fluorescence emitted when the system is continuously excited, and ρ_0 is the corresponding steady state. This ratio is measured experimentally, and for each measured ratio we can determine the corresponding rate, R , using Γ and the values given in Table. 2.2. This expression can be rewritten as,

$$(\zeta \cdot \rho_0) \frac{\delta F(t)}{F_{cw}} = \int_0^T d\tau h(t, \tau) R(\tau), \quad \text{where}$$

$$h(t, \tau) = \begin{cases} g(t, \tau) + f(t, \tau) & \text{if } t > \tau \\ g(t, \tau) & \text{otherwise} \end{cases}$$

Experimentally we measure the change in fluorescence averaged over the period, $\langle \Delta F \rangle$; we therefore define $H(\tau) = \int_0^T dt h(t, \tau)$ and integrate both sides over the the period to obtain,

$$(\zeta \cdot \rho_0) \frac{\langle \delta F \rangle}{F_{cw}} = \frac{1}{T} \int_0^T d\tau H(\tau) R(\tau)$$

Numerically it can be shown that is H constant to a good approximation for $\Gamma < 1$ MHz, so that we can write:

$$\langle R \rangle = \beta(\Gamma) \frac{\langle \delta F \rangle}{F_{cw}} ; \text{ where } \beta = \frac{\Omega_E \cdot \rho_0}{H}$$

If ω_{12} is the energy gap between the relevant levels, then the power is given by,

$$\langle P \rangle = \hbar \omega_{12} \beta(\Gamma) \frac{\langle \delta F \rangle}{F_{cw}} \quad (3.6)$$

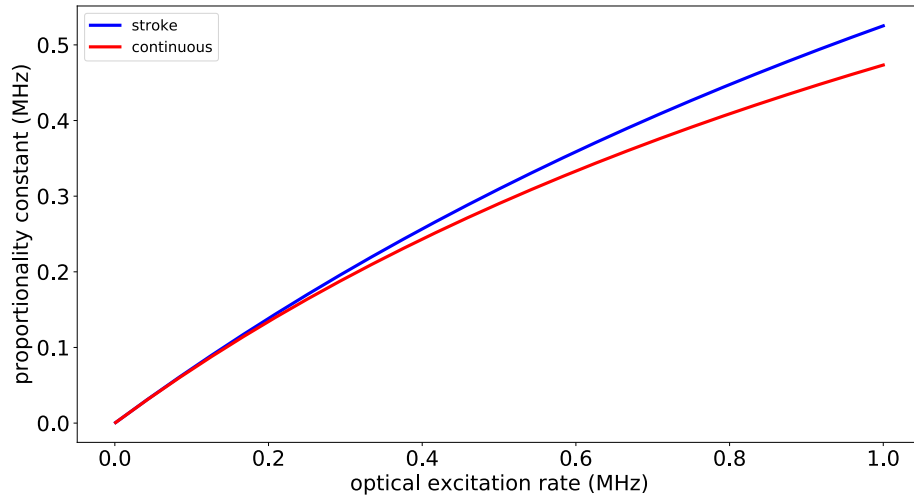


Figure 3.7: Proportionality constant as a function of Γ for both continuous and two-stroke engines ($d = 33\%$) .

3.4 Putting it together

We have shown that off-resonant optical excitation emulates a simultaneous coupling of the hot and cold baths, and that we may deduce information about the engine performance from measurements of the resulting fluorescence emission. In this section we consider how these results may be used to implement the different varieties of quantum heat engine with an ensemble of NV centres. Recall that the simultaneous coupling of hot and cold baths allows us to test the continuous and two-stroke engines, but prevents us testing the four-stroke engine. In principle, ignoring some of the practicalities of the experimental setup, the procedure for implementing these varieties is now comparatively simple. To begin with, the microwaves should be tuned to the central frequency of the $|0\rangle \leftrightarrow |1\rangle$ transition. For a given experimental run the CW fluorescence intensity is measured for the optical power being used to obtain the normalisation factor F_{cw} – one quarter of the measured value is used because only 25% of the NV centres, those which are aligned with the magnetic field, are addressed by the microwaves. Then for the continuous engine, this microwave transition should

be continuously driven in conjunction with the off-resonant optical transition, whilst also monitoring the fluorescence emitted by the centre, as shown in Fig. 3.8.



Figure 3.8: The sequence of driving and measurement for the continuous engine.

The two-stroke engine is not considerably more complicated, merely requiring that we separate out the coherent and thermal parts of the driving. This involves choosing a duty cycle (which need not be 50%), and correctly synchronising the driving of the microwave and optical transitions, so that each is driven alternately – this is done whilst still monitoring the fluorescence continuously, as shown in Fig. 3.9.

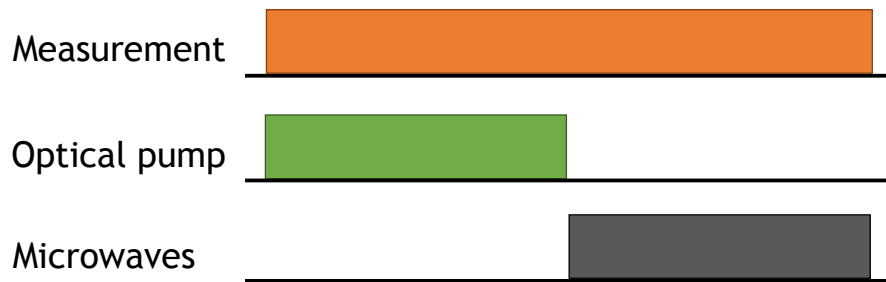


Figure 3.9: The sequence of driving and measurement for the two-stroke engine.

In each of these engine types, the differences between the fluorescence with and without microwave driving was measured, whilst leaving the optical driving unchanged.

The optical excitation rate was then determined for the laser power used, in order to determine the proportionality constant $\beta(\Gamma)$ (Eq. 3.6) and thermalisation rates.

3.5 Experimental setup

3.5.1 Diamond sample preparation

A type Ib high-pressure-high-temperature $3 \times 3 \times 0.3\text{mm}$, (100) diamond slab (fabricated by Element-Six) was electron irradiated (10^{18} cm^{-2}) and then annealed (950 °C, 2.5 h), to form a dense (10^{18} cm^{-3}) ensemble of NV centres. The orientations of the centres are randomly distributed between all the $\langle 111 \rangle$ directions.

3.5.2 Microwave Waveguide

To begin with we consider the design of the microwave waveguide used to deliver microwaves to address the ground state resonances and provide the coherent part of the engine action. Some of the standard methods used to drive the microwave transitions of the NV centre include placing a single-nano wire close to single NV-centres, microwave waveguides, and microwave resonator structures [70, 71, 44]. Because we were using an ensemble, we required the microwave field be both sufficiently strong and uniform across the volume we were probing. In this section some of the steps taken toward the final design of the microwave setup are briefly detailed.

A first attempt simply involved twisting a short length of copper wire into a loop, inserting one end into the end of the coaxial cable attached to a microwave generator (HP8763), and placing the diamond in the middle of the loop. We were unable to see any form of signal using this antenna, even when using maximum power (10dBm). This can be attributed to several design flaws, foremost of which was the fact that

the loop was not impedance matched to the coaxial cable (50Ω) – this mismatch will have resulted in most of the incident microwaves reflecting at the interface. Secondly, by placing the sample near the middle of the loop, it was too far from the wire, where the field is strongest.

To remedy these problems a second design was attempted. This was also a loop, but now designed with impedance matching in mind, and further made on a printed circuit board (PCB). The impedance of a circuit with resistance R , inductance L and capacitance C , for waves with angular frequency ω , is given by,

$$Z = R + i(\omega L - \frac{1}{\omega C}),$$

If the negligible self-inductance of the wire is omitted, the loop inductance is given by,

$$L_{loop} = r\mu_0 \left[\ln \left(\frac{8r}{a} - 2 \right) \right]$$

Initially only a resistor in series was added to match the real part of the impedance. Additionally, rather than input the microwaves directly into the loop from a coaxial cable, the microwaves were launched into the antenna via a microwave slotline – the impedance of the slotline could be matched by choosing the width of the slot. Finally, the sample was moved to lie closer to the wire. A photograph of this design is given in Fig. 3.10. In addition to the modifications made directly to the antenna, a 35 dB microwave amplifier was added in conjunction with a circulator. These modifications immediately allowed us to obtain an ODMR signal as shown in Fig. 3.11.

Notwithstanding this improvement, it was decided that this design could be improved upon further. This resulted in the design and fabrication of a microwave waveguide, known as a microstrip line, which was the final design used in the experiment. A microstrip line consists of a thin strip of conductor lying on a (ideally infinite) slab of



Figure 3.10: The improved loop antenna design.

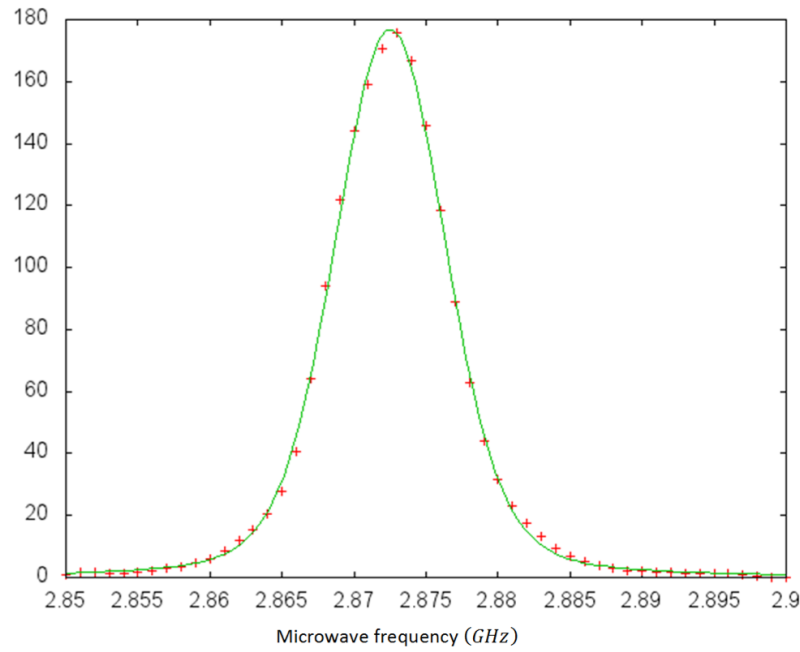


Figure 3.11: ODMR spectrum of the zero field microwave resonance

dielectric material with ground plane on its underside. The impedance of a microstrip line is determined by the width of the strip (W), the thickness of the dielectric material (h), the dielectric constant (ϵ_r), and the RF frequency (f), through the following expression [72],

$$Z = \frac{120\pi}{\sqrt{\epsilon_{eff}}} \left[\frac{W}{h} + 0.677 \ln \left(\frac{W}{h} + 1.44 \right) + 1.393 \right]^{-1},$$

where the effective dielectric, ϵ_{eff} , can be thought of as the dielectric constant for a homogeneous medium which yields the same behaviour as the combination of air and the microstrip line, and is given by [72]:

$$\epsilon_{eff} = \frac{\epsilon_r + 1}{2} + \frac{\epsilon_r - 1}{2} \left(1 + 12 \frac{h}{W} \right)^{-\frac{1}{2}}$$

Because the type of dielectric and its thickness were pre-specified by the PCB we used, we had to adjust the width of the strip to ensure that the waveguide impedance was matched to 50Ω . In order to maximise the field strength in the sample, a short (1.7mm) section of the strip was tapered down to $300\mu m$; the diamond sample was then centred over this tapered section. The tapered section was made to be significantly shorter than the wavelength ($l_{taper}/\lambda = 1.7/100$) in order to minimise reflections from the resulting impedance mismatch.

An additional requirement was that the magnetic field of the microwaves be perpendicular to the static field; due to the design and constraints of our setup, this necessitated the inclusion of corners in the strip, which were constructed using mitred bends, whose geometry is such that the incoming microwaves are neither scattered nor reflected. The relevant quantity here is the ratio of x to d (see Fig. 3.13), which is given by [73]:

$$\frac{x}{d} = \frac{1}{100} \left[52 + 65e^{-\frac{27}{20} \frac{W}{h}} \right],$$

where x and d are as in Fig. 3.12, and W and h are the width of the strip and thickness of the dielectric respectively. The parameters characterising the microstrip line we used are given in Table. 3.1.

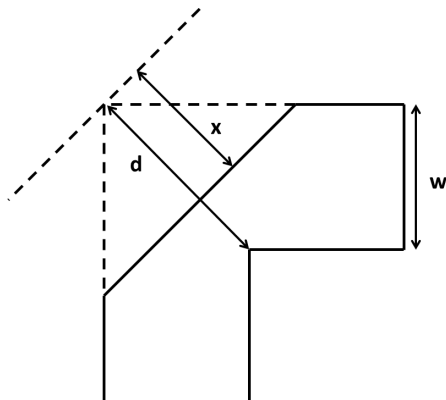


Figure 3.12: Optimal design for right angled bend for microstrip line

Table 3.1: Table of parameters for 50Ω microstrip line

Width	1.95 mm
Taper width	$300\text{ }\mu\text{m}$
Taper length	$\sim 1.7\text{ mm}$

The final design is shown in Fig. 3.13 (in this case the taper was $200\text{ }\mu\text{m}$ rather than the $300\text{ }\mu\text{m}$ used in the experiment).

3.5.3 Setup

Aside from the microwave components, the remaining parts can be broadly divided into the optics to direct light into the sample, and the detection part to collect and measure the emitted fluorescence, as well as electronics to control the experiment and collect data.

The light for the optical excitation was provided by a continuous wave (CW) 532nm diode laser (Thorlabs DJ532-40), able to produce up to 50mW. The diode was housed in a laser mount (Thorlabs TCLDM9 - TE-Cooled Mount) with temperature and current controllers. A telescope consisting of 11mm followed by 50mm lenses was placed immediately after the laser in order both to collimate the slightly divergent



Figure 3.13: Top down view of the microstrip line.

beam, and to expand it from $\sim 1\text{mm}$ up to $\sim 5\text{mm}$. The beam was then focussed down into an acousto optical modulator (AOM – Gooch and Housego AOMO 3350-197) using a 50mm lens. The rise and fall time of the AOM is set by the time it takes for the acoustic wavefront to propagate across the beam waist; therefore, in order to minimise the response time, it is necessary to minimise the width of the waist – this is the reason for expanding the beam prior to the AOM. This can be seen by considering a Gaussian beam propagating through a thin lens:

$$\omega'_0 = \frac{\lambda_0 f}{n\pi\omega_0} \frac{1}{\sqrt{1 + \left(\frac{f}{z_R}\right)^2}}$$

Here λ_0 is the wavelength of the light, f the focal length of the lens, ω_0 the width of the waist, and z_R the Raleigh range. Fom this it can be seen that there is a tradeoff between the rise/fall time of the AOM and its diffraction efficiency (the percentage of light that it is able to diffract into the first order mode), due to the efficiency also depending on the beam waist area (the number of acoustic wavelengths across the waist). The diffraction efficiency and rise/fall times in our configuration were approximately 60% and 12ns respectively. The AOM was controlled using a 350MHz analog controller, which was driven using square pulses from an arbitrary waveform generator (AWG – Keysight KS 33600A, 30MHz). The function of the AOM was

to modulate the CW light to produce the pulses required for the two-stroke engine; additionally, because adjusting the laser power using the current is strongly non-linear and takes a long time to fully equilibrate, the AOM allowed us to quickly vary the intensity of light at the sample once the laser was in a stable configuration.

The first order mode from the AOM was then selected by spatially filtering using an iris. It was then recollimated and expanded further using a 150mm lens. A flip mirror directing the light at a photodiode was placed at this point in order that we could measure the light intensity, and takes time traces of the pulsed light. After this the beam was passed through one more telescope, with one lens mounted on a translation stage, in order to provide a final degree of freedom to adjust the light entering the objective lens, and ensure that it filled the aperture of the objective ($\sim 1\text{cm}$). The light was directed into the objective lens using a dichroic mirror (Semrock long pass), reflecting the 532nm (green) light and allowing 637nm (red) to pass, as shown in Fig. 3.16. The objective used was a Sigma Koki S-plan APO HL with $20\times$ magnification and a numerical aperture (NA) of 0.29. The objective focused the light into the sample, with a focal spot size of approximately $2\mu\text{m}$.

The same objective was used to collect the fluorescence emitted by the NV centres in the focal spot. Since the fluorescence is emitted into the zero phonon line (ZPL) and phonon side band (PSB), it spans wavelengths from 637nm and above; these wavelengths are able to pass through the dichroic mirror, whilst any green light which might have been reflected or scattered off the lens and sample is blocked. The confocal setup used was not of the usual kind, but rather adapted to our purposes. We wished to image a small volume within the green focus to ensure a homogeneous intensity distribution for both the light and microwave fields; we therefore used a 300mm lens after the dichroic mirror followed by a single mode optical fibre, so that the focus was imaged onto the fibre with a $\times 30$ magnification. Because of the single mode nature

of the fibre (with $< 5\mu m$ core width), only a small fraction of the total fluorescence, selected from the centre of the focal point, ended up being coupled into the fibre. The other end of the fibre was connected to a silicon avalanche photodetector (APD – Thorlabs APD110A/M, 400-1000 nm), the signal of which was fed into a lock-in amplifier (Stanford research SR810).

The microwaves were provided by an HP 8673D microwave generator, which provides CW microwaves, with a bandwidth of 1Hz, in a power range from -100dBm to 10dBm, and frequency range from 50MHz to 18.6GHz. The microwaves can be modulated slowly (20Hz - 10kHz) using an external analog input – this was provided by a function generator producing a ~ 100 Hz square waveform at a 50% duty cycle; the same signal was used to provide the reference frequency for the lock-in amplifier. The output from the microwave generator was fed into a fast microwave switch (Mini-Circuits ZASWA-2-50DR+) with a 1.5ns switching time. The output from the switch was fed into a microwave circulator (UIY UIYBCC6434A), to prevent high power back reflections into the switch and source, before being sent into a microwave amplifier. The amplifier (Mini-Circuits ZVE-3W-83+) provides +35dB broadband (2GHz -18GHz) amplification to the microwaves; although the important data was taken at low microwave powers (i.e. the low action regime), which could easily be provided by the generator alone, it was useful to be able to reach the higher powers allowed by the amplifier for calibration purposes and auxiliary measurements. After the amplifier, the microwaves were sent to the microstrip waveguide (sub sec. 3.5.2), whose other end was capped with a 50Ω terminator. The signal controlling the microwave switch was provided by the second channel of the AWG controlling the AOM; these two channels were set to the same frequency and were synchronised (phase-locked).

The diamond sample was mounted by gluing it directly onto the tapered section of the microstrip waveguide. The angle of the diamond was adjusted such that one of

the $(1, 1, 1)$ directions lay perpendicular to the magnetic component of the microwave field produced by the stripline (i.e. in the plane parallel to the stripline and at right angles to the PCB) – this simply involved aligning two of the corners of the crystal with the stripline. The waveguide PCB was attached to a plastic mount, which was further attached to translational stages allowing us to adjust the vertical and axial (with respect to the beam) positions of the sample. The beam was directed into the sample perpendicularly through the upper facet of the diamond, as shown in Fig. 3.14.

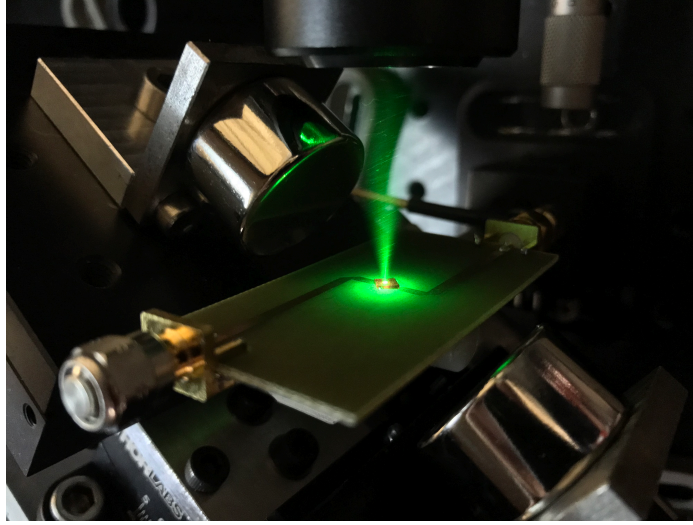


Figure 3.14: The diamond fixed on the waveguide, lying between two magnets, with green light focused in using an objective.

A pair of rare earth magnets were used to provide the static magnetic field required to reorder the ground state levels in the manner required for this experiment. The anti-crossing between $|0\rangle$ and $|+1\rangle$ occurs at an axial field strength of 0.102 T, and the experiment required the field go beyond this strength in order to achieve the correct ordering and to avoid any mixing of the states. In order to produce a homogeneous field of the correct strength and direction, we required control over translational, rotational and separation degrees of freedom. The magnet separation and one of the translational degrees was provided by mounting the magnets on individual stages, which were fixed onto a plate, such that adjusting the stages only changed the axial

separation between the magnets. This plate was mounted on a tilt stage, which in turn was mounted on a rotation stage; these two stages allowed us the necessary degrees of freedom to fix the orientation of the field. Finally, the remaining two translational degrees of freedom were provided by attaching the rotation stage to two more translational stages. A photograph of this construction can be seen Fig. 3.15.

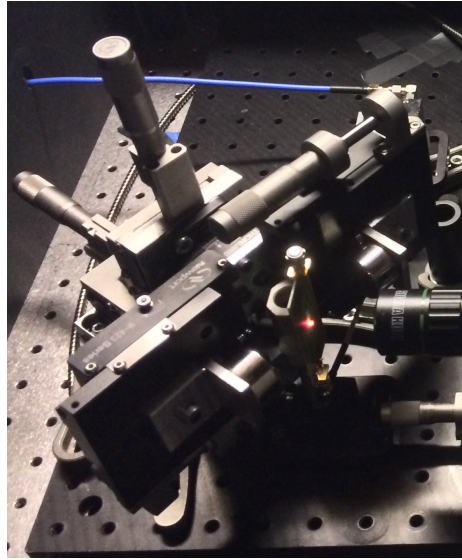


Figure 3.15: Photograph of the stages used to adjust the magnetic field, together with the diamond sample glowing red under fluorescent excitation in the centre.

A schematic of the whole setup and the connections between the various components can be seen in Fig. 3.16.

3.5.4 Spectroscopy

Continuous Wave

Continuous wave spectroscopy, making use of the ODMR technique, was used to take microwave spectra and probe the ground states of the NV centre [49]. During the measurement, the sample is simultaneously illuminated with continuous green laser light and squared amplitude modulated microwaves, whilst at the same time the

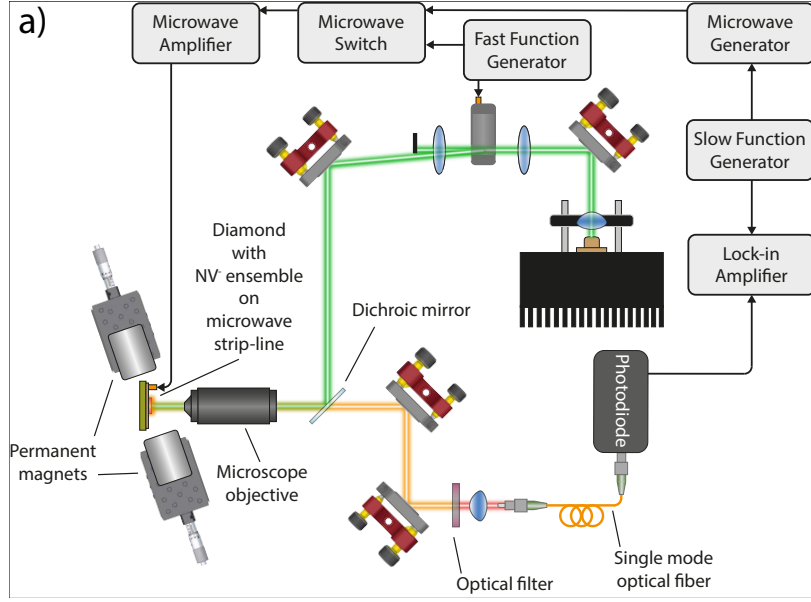


Figure 3.16: Schematic of the experimental setup, showing the more important components.

fluorescence is collected and detected with the lock-in amplifier locked to the same frequency as the microwave modulation. The ODMR response can then be measured as a function of the microwave frequency, which produces a drop in fluorescence when a transition is reached. This measurement enabled us to track the changes in the ground state levels as we increased the static magnetic field. The field was increased until the $|+1\rangle$ state lay $\sim 2\pi \times 2750$ MHz below the $|0\rangle$ state. An anti-crossing was observed during this process; using this we were able to extract the extent to which the magnetic field was misaligned from the NV axis from the minimum energy gap between these states at the anti-crossing. Similar CW scans were run prior to any measurements in order to determine both the position and linewidth of the resonance. An example of such a scan is given in Fig. 3.17.

The minimum linewidth we were able to achieve was a full-width half maximum of $2\pi \cdot 7.5$ MHz ($\sigma = 3.1$ MHz). The ensemble coherence time is given by $1/T_2^* = \sqrt{2}\pi\sigma$, so that the maximum ensemble coherence time ($1/e$) in our sample is 72 ns.

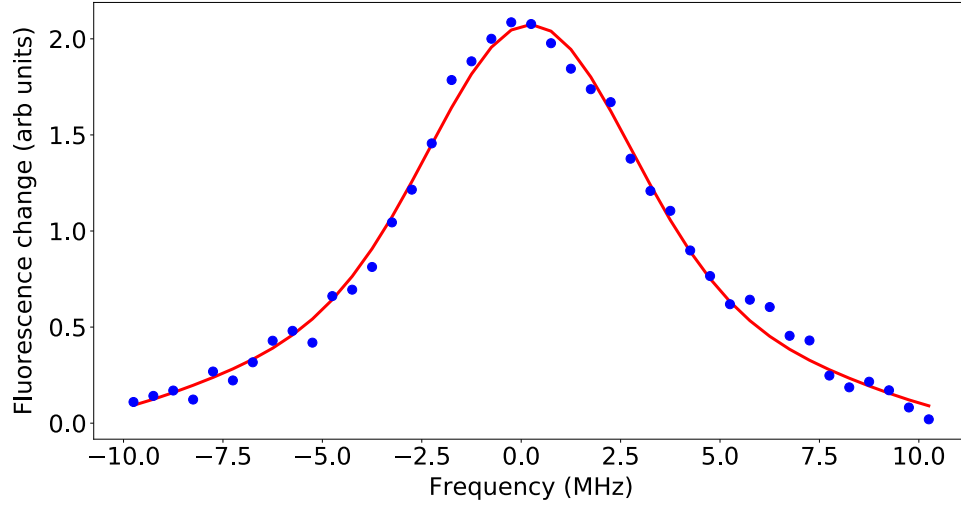


Figure 3.17: ODMR spectrum of the $0 \leftrightarrow 1$ ground state transition in the NV centre, together with best fit Voigt profile.

Aligning the magnetic field

The states are reordered using an external magnetic field, which acts on the states through the Zeeman interaction. Recall that the Hamiltonian describing the interaction in the ground states is given by,

$$H_{Zeeman} = \frac{g_{gs}\mu_B}{\hbar} \vec{S} \cdot \vec{B}$$

If we define $B_{\parallel} = (B_x + iB_y)/\sqrt{2}$ and $B_{\perp} = B_z$, it can be shown that the total Hamiltonian is given by,

$$H_{gs} = \begin{pmatrix} 0 & B_{\perp} & B_{\perp}^* \\ B_{\perp}^* & D_{gs} - B_{\parallel} & 0 \\ B_{\perp} & 0 & D_{gs} + B_{\parallel} \end{pmatrix}$$

It can be seen that the axial terms (B_{\parallel}) are responsible for shifting the levels whilst preserving the eigenstates, and, to first order, the transverse terms (B_{\perp}) do not shift the levels, but do mix the $|\pm 1\rangle$ states with $|0\rangle$. To avoid mixing of the states, which

reduces the fluorescence contrast and pumping efficiency, the magnetic field should be aligned as closely as possible with the NV axis. Any transverse component of the magnetic field results in an anti-crossing between $|1\rangle$ and $|0\rangle$ at $B_z = 0.102\text{T}$ as shown in Fig. 3.18. To get a reasonable separation between the states and minimise any residual mixing, we chose to work at a magnetic field strength of approximately 0.2T , which corresponds to a $|0\rangle \leftrightarrow |1\rangle$ splitting of about 2.7GHz .

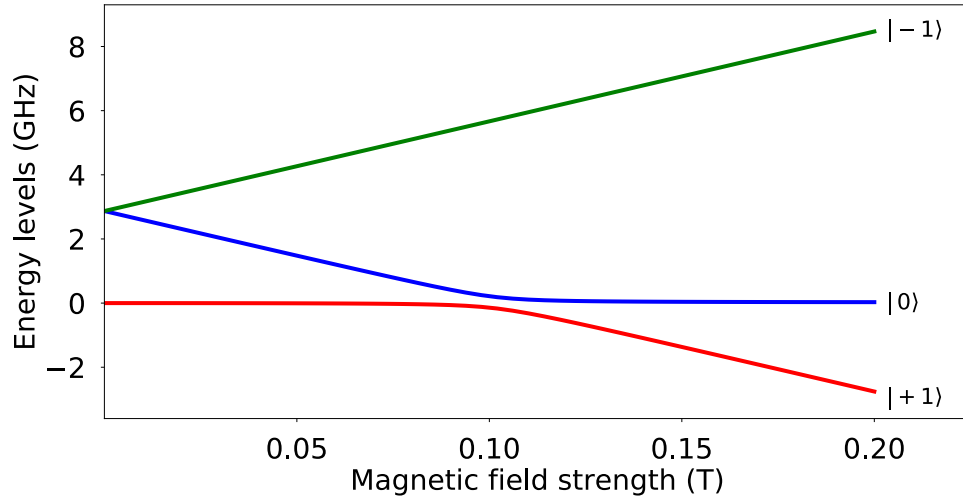


Figure 3.18: A plot of the effect of a magnetic field on the ground state energy levels. The field angle used was 5° off axis.

We were able to use the magnitude of this separation at the anti-crossing to align the field by minimising the separation – the resonances at the anti-crossing are shown in Fig. 3.19. The minimum separation was $\sim 20\text{MHz}$, corresponding to an off axial angle of $< 1^\circ$.

In addition, the position of the magnets was adjusted to minimise the linewidth of the transitions, which corresponds to placing the optical focus in the centre of the magnets where the field was closest to being homogeneous.

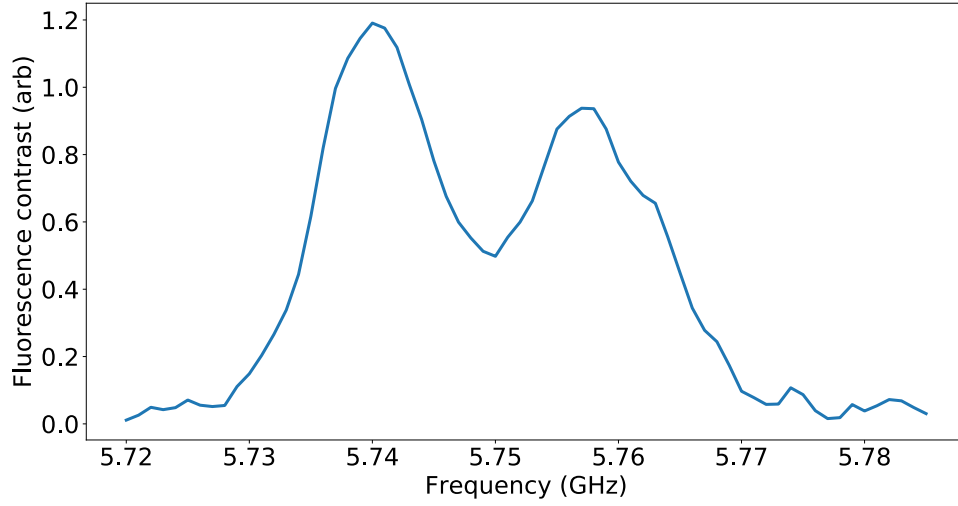


Figure 3.19: Minimum separation of 17 MHz at the anticrossing.

Rabi Oscillations

The Rabi frequency for a given microwave power was also measured using ODMR. In this case, the microwaves were pulsed at a particular repetition rate on top of the slow square-wave amplitude modulation. The optical pumping was also pulsed with the inverse waveform to the microwaves. The repetition rate was chosen to be sufficiently slow for the NV to optically re-equilibrate in the duration of the optical pumping, whilst also being fast enough to ensure a good signal to noise ratio. The pulse sequence is shown schematically in Fig. 3.20. The repetition rate of the pulses was kept fixed and the pulse width was scanned, so that Rabi oscillations in the signal amplitude were observed as seen in Fig. 3.21.

The Rabi frequency is defined by, $\Omega = \mu_B g_{gs} B_{\perp}$ (\vec{B} here refers to the magnetic field component of the microwaves rather than the static field discussed previously). Since the microwave power is proportional to $|B|^2$, we expect the Rabi frequency to go like $\Omega \propto \sqrt{P_{MW}}$. By taking a number of Rabi scans similar to that in Fig. 3.21

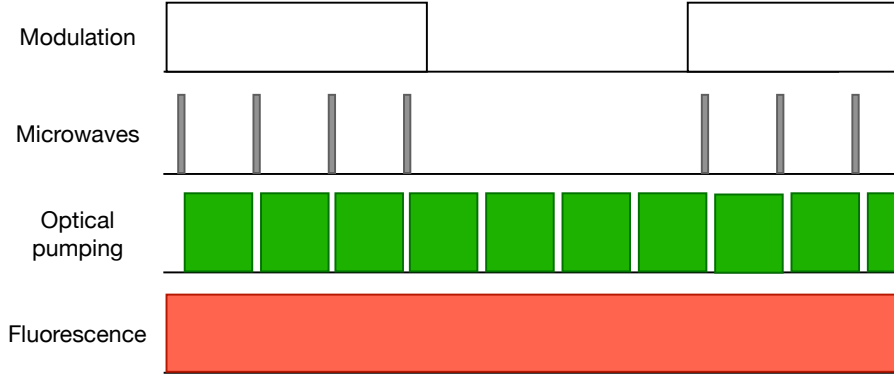


Figure 3.20: Schematic showing the pulse sequences used in the experiment for measuring the Rabi frequency at a given microwave power.

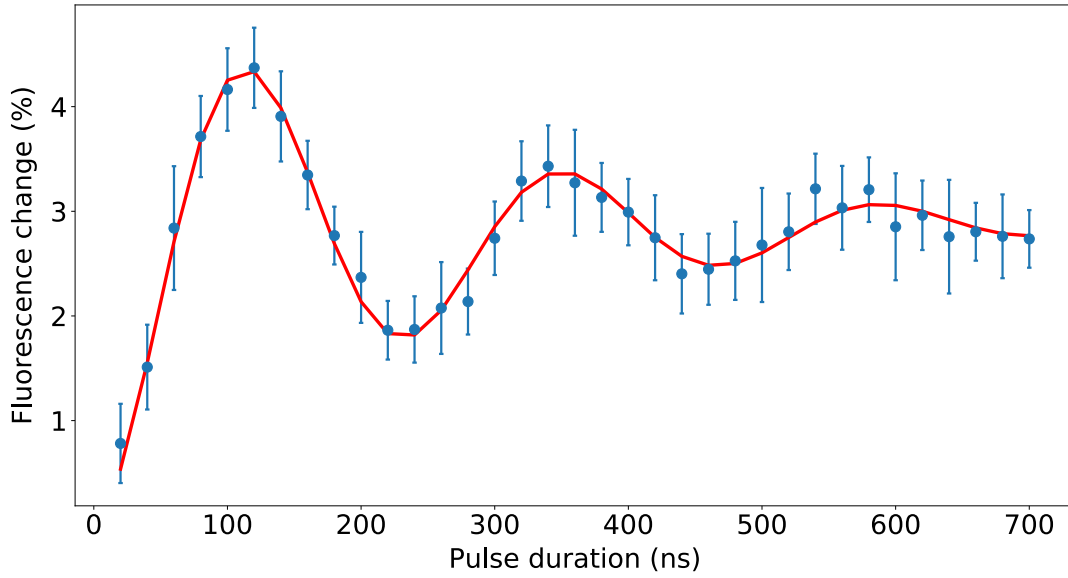


Figure 3.21: An example of a Rabi scan showing several oscillations and an exponential decay, this instance taken at $(-3 \pm 35)\text{dBm}$. Here the errorbars were estimated by the variance of several measurements.

at different input microwave powers, we were able to determine the proportionality between the Rabi frequency and the square-root of the power. The repetition rate was chosen to be approximately 20kHz, the pulse durations were scanned across the range 10ns - 1 μ s, and the slow modulation set to be $\sim 130\text{Hz}$ (ensuring that it was not a multiple of 50Hz). For the data presented in 3.22, the constant was determined

to be $2\pi \times (137 \pm 2) \text{ kHz}/\sqrt{mW}$.

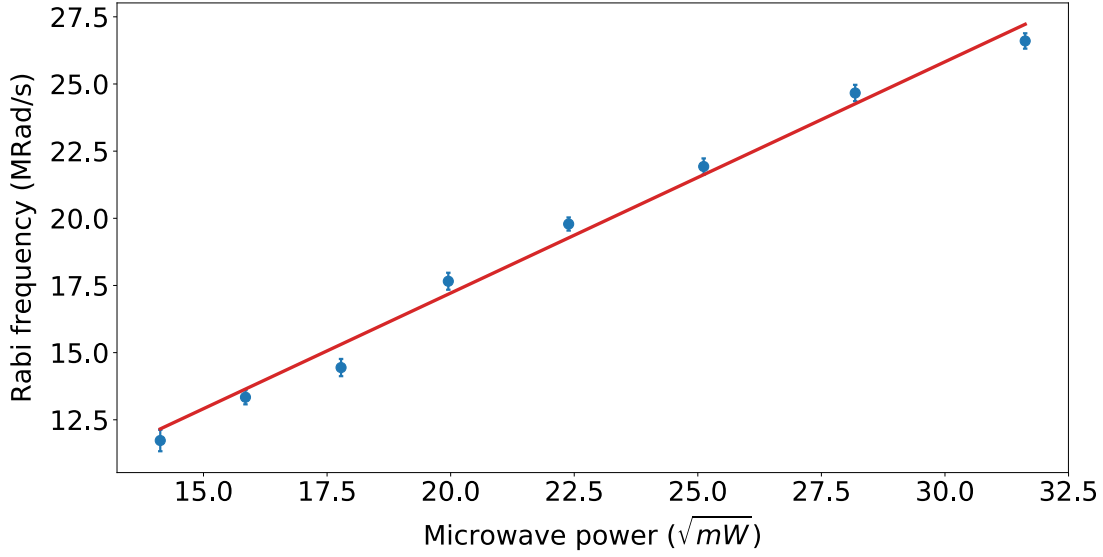


Figure 3.22: Rabi frequency calibration.

Ramsey Interferometry

Ramsey interferometry was also attempted on our sample in order to obtain a second and direct measurement of the ensemble coherence time T_2^* . A Ramsey pulse sequence consists of two $\pi/2$ pulses separated by a delay, denoted by τ . The functional form of the population in $|0\rangle$ after this sequence is given by,

$$P_0 = Ae^{-t/T_2^*} \cos(\omega t + \delta)$$

In order to determine the $\pi/2$ time a Rabi scan is performed first. These pulses are then fixed and delay between them is then scanned to produce the data shown in Fig. 3.23, which also includes the best fit of the above function. The scan in Fig. 3.23 was the clearest of the Ramsey scans that we were able to obtain; nevertheless, it can be seen that it decays too rapidly to be able to extract much information from it.

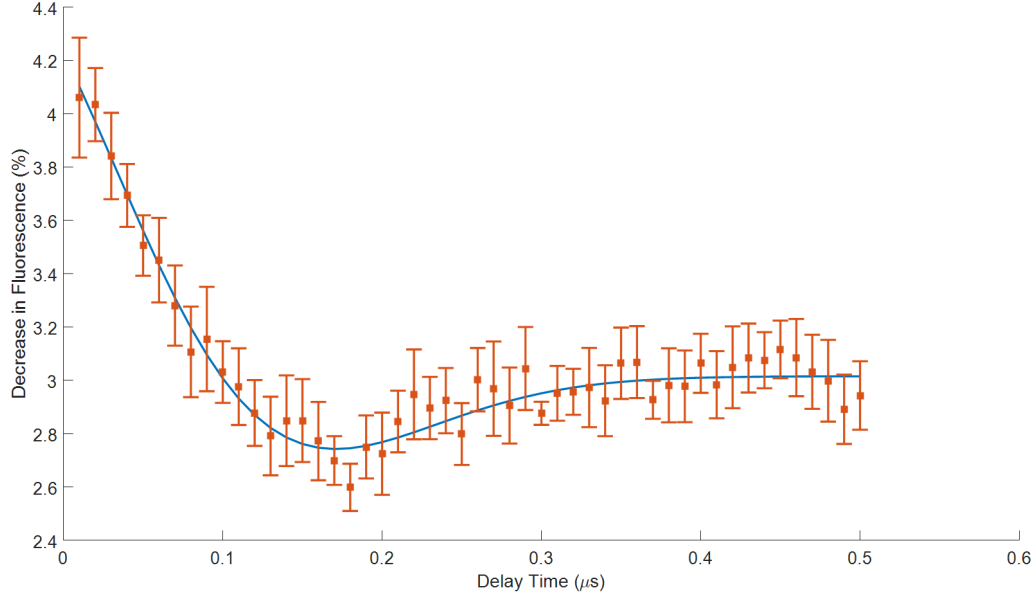


Figure 3.23: Ramsey scan. This data is the result from multiple runs, which allowed for the errorbars to be estimated from the measurement variance.

3.5.5 Thermalisation

The rate equation model was used to determine the relation between the laser power and the optical excitation rate, Γ . This quantity is needed to determine the proportionality constant, $\beta(\Gamma)$, as well as the effective thermalisation rate in the heat engine. The steady state populations, P_0 , as a function of Γ are defined implicitly by $M(\Gamma)P_0(\Gamma) = 0$. The fluorescence (up to proportionality) can be calculated by,

$$F(\Gamma) \propto \zeta \cdot P_0(\Gamma),$$

where the dot product with $\zeta = [0, 0, 0, 1, 1, 1, 0]$ gives the population in the excited state manifold. We also know that the optical excitation rate, Γ , must be proportional to the input light intensity I . This allows us to write,

$$F(I) = \alpha \zeta \cdot P_0(\beta I),$$

where α and β are undetermined proportionality constants, with β being the

constant of interest to us (whereas α relates to the number of NV centres and the collection efficiency).

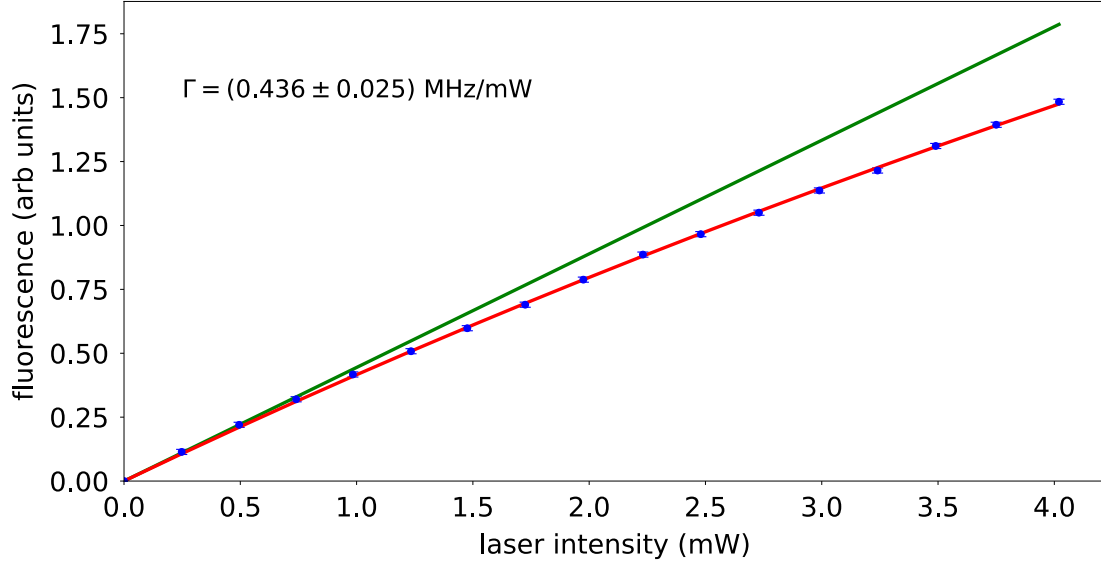


Figure 3.24: The blue dots are the measured data points, the red curve is the best fit used to extract Γ , and the green curve is the linear extrapolation of the data at low intensity (to help illustrate the deviation from linear scaling).

By measuring the fluorescence for a range of input laser powers and fitting the calculated fluorescence to these results, one is able to extract these parameters. Note that it is important that the measurements extend into the region where the fluorescence responds non-linearly, otherwise only the product $\alpha\beta$ can be determined. The result of the fit using these two parameters is shown in Fig. 3.24.

Measuring Pulse Shapes

It was important to determine the pulse shape of the microwaves and light pulses for the theoretical calculations, which used them in the most general form of the numerical integration (rather than assume the ideal case of perfect square pulse shapes). In addition it was important to determine the time average of the Rabi frequency to correctly determine the quantum bound (Eq. 2.19). A fast oscilloscope (30GHz) was

used to directly measure the microwaves transmitted through the waveguide. One such trace is shown in Fig. 3.25. In order to determine the time dependence of the Rabi frequency, we required the envelope of this trace. It was first low pass filtered to remove high frequency noise, which would have resulted in false local extrema; the upper and lower envelopes were subsequently found by searching for local maxima and minima respectively. These are shown in Fig. 3.26.

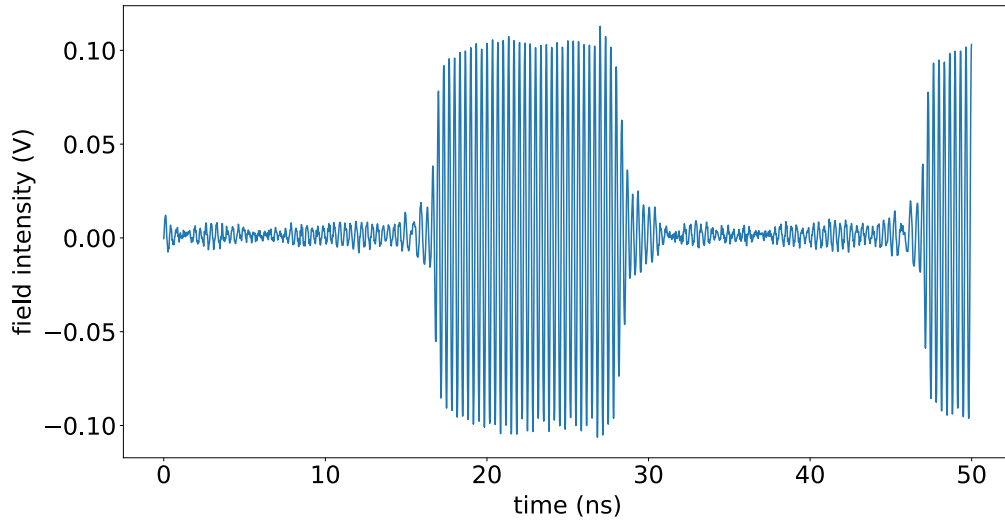


Figure 3.25: The raw signal measured by the oscilloscope for the 10ns pulse duration.

The total waveform is given by $V(t) = A(t)e^{i\omega t} + C(t)$, where $A(t) \propto \Omega(t)$ is the envelope that we are interested in, and $C(t)$ is an offset (which should be zero, but plays no role in any event). These can be found by noting that the waveform can be expressed in terms of the upper and lower envelopes can be expressed as in Eq. 3.7. The resultant difference between the envelopes, normalised to the CW field, is shown in Fig. 3.27.

$$V(t) = 0.5 [U(t) - L(t)] e^{i\omega t} + 0.5 [U(t) + L(t)] \quad (3.7)$$

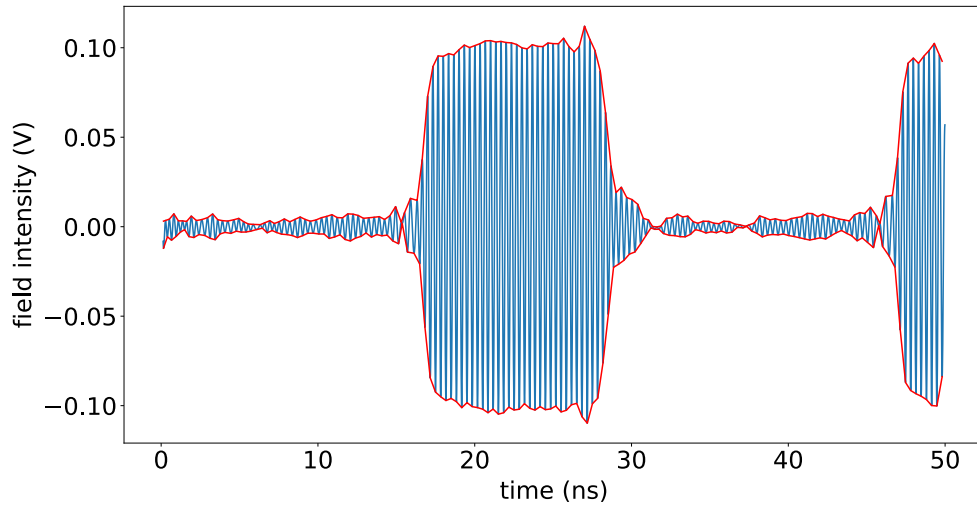


Figure 3.26: Filtered signal with upper and lower envelopes.

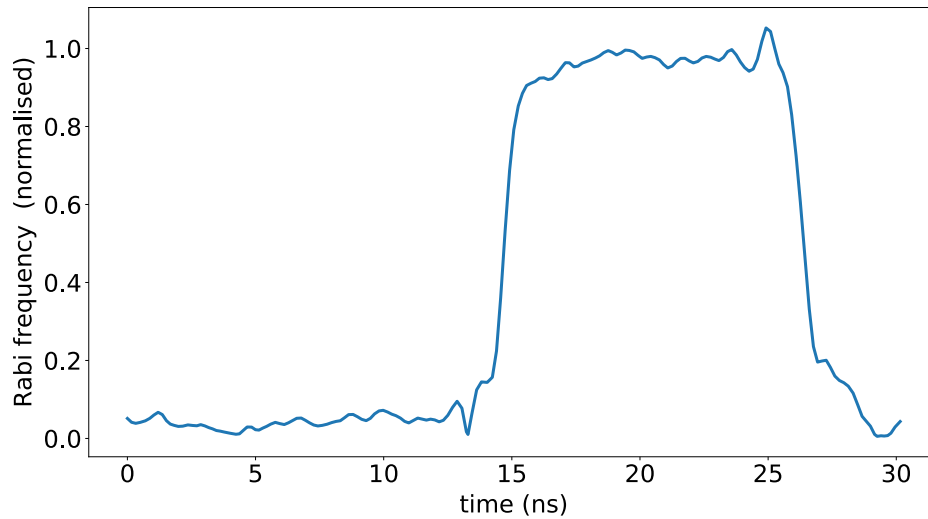


Figure 3.27: The total pulse envelope calculated as the difference between the upper and lower envelopes.

The procedure was simpler for the light pulses for which the intensity could simply be measured directly with a fast photodiode (Thorlabs Si detector with a response time of approximately 1ns). A joint plot of the microwave and light traces, as would have been used for the two stroke engine, can be seen in Fig. 3.28. It can be seen that the optical rise and fall times are substantially slower than the corresponding

microwave times, due to the slower response of the AOM. Whilst this isn't altogether satisfactory from an aesthetic point of view, provided the average optical intensity is as expected (66% in our case), it makes little practical difference to the experiment, since the thermal part of the action does not feature in the bound, as will be shown later.

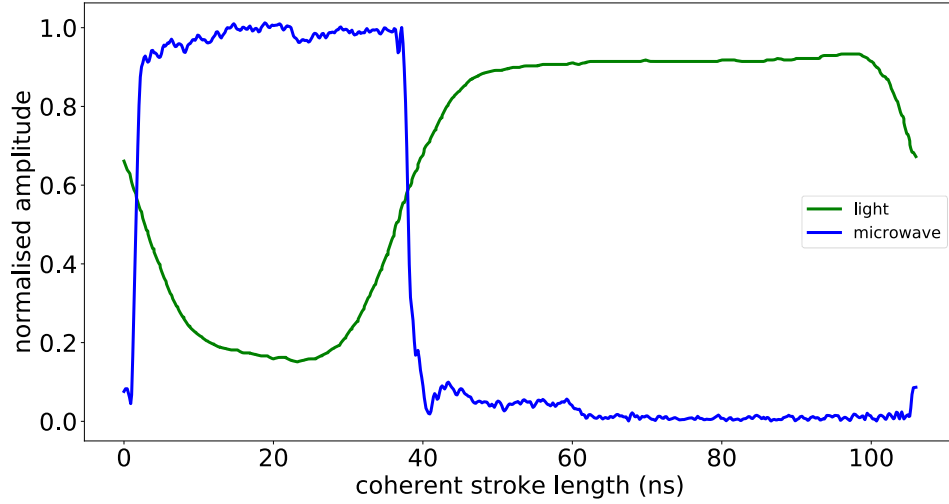


Figure 3.28: Combined microwave and optical waveforms.

Determining NV^0 contribution to the Spectrum

Recall that the power output of the NV engine could be inferred from measurements of the normalised fluorescence difference with and without microwave driving. This relies on the difference being correctly normalised with the background fluorescence. Because the majority of the NV fluorescence spectrum lies at wavelengths greater than the ZPL [49], all wavelengths above 637nm were included in the fluorescence measurement; whilst the NV^0 has a higher energy ZPL of 575nm, a substantial portion of its PSB lies above 637nm, which would affect the fluorescence measurement. In one sense this is not a major problem for either of the experiments considered in this thesis. The equivalence test requires only that we know the power outputs of the

continuous and two stroke engines up to some universal constant, whilst the quantum thermodynamic signature merely requires that the measured power be greater than the stochastic bound – because NV^0 contributions will result in a larger background fluorescence, the measured power is a lower bound for the actual value. Nevertheless, we took a spectrum of our sample which is shown in Fig. 3.29

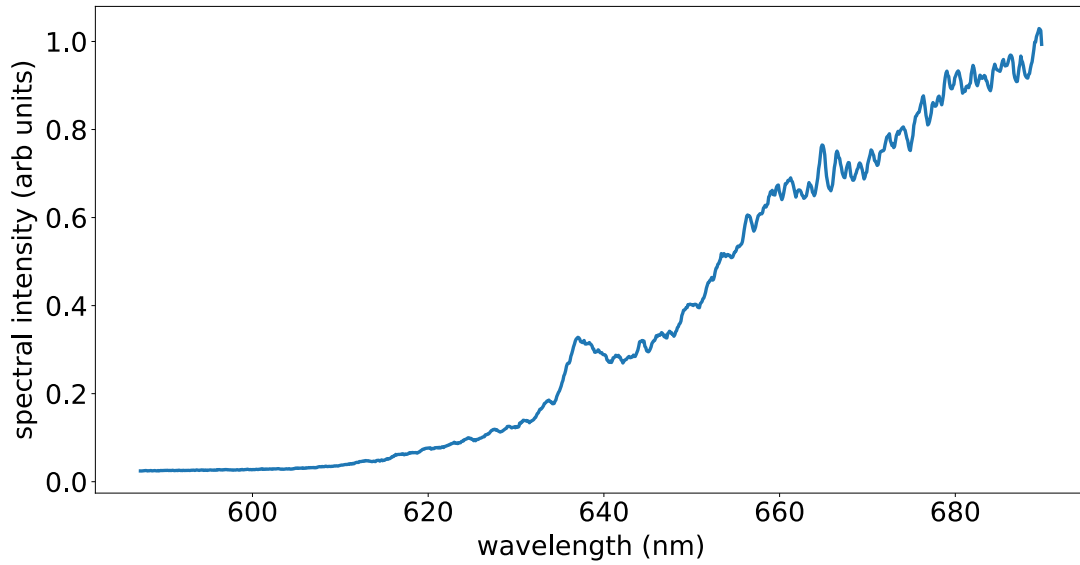


Figure 3.29: Fluorescent spectrum for the diamond sample used in the experiment. It can be seen that there is only a NV^- contribution to the spectrum, with no NV^0 apparent.

It can be seen that only the increasing edge of the NV^- spectrum can be seen in the region (580 - 640) nm, with no indication of the large NV^0 PSB, allowing us to conclude that there is negligible NV^0 contribution to the spectrum.

Chapter 4

Results

4.1 Theory results

Here I present theoretical work related to the heat engine, which extends the work presented in the previous chapter to account for deviations of the physical implantation from the idealised model discussed previously; this is particularly necessary in our realisation which consists of a dense ensemble of defects in a noisy solid state environment.

4.1.1 Inhomogeneous broadening

The idealised engine consists of a single quantum entity, which is driven on resonance; by contrast, our experimental system consists of a large ensemble of NV centres in a room temperature, solid state environment. The NV^- ground spin states are coupled to the local diamond strain, magnetic and electric fields, and neighbouring nuclear and impurity spins. Each of these interactions shift the spacings between the spin states by an amount depending on the local environment of each centre, resulting in a distribution of resonance frequencies across the ensemble.

Hamiltonian

We begin by considering a single detuned NV centre. The ability to drive the transitions in the ground state relies on the magnetic dipole interaction, which arises through the Zeeman term in the Hamiltonian [55, 56, 62],

$$H_{\text{Zeeman}} = g_e \frac{\mu_B}{\hbar} \vec{S} \cdot \vec{B},$$

where $g \approx 2.0$ is the electron g-factor, μ_B is the Bohr magneton, and the spin matrices are given by,

$$S_x = \frac{\hbar}{\sqrt{2}} \begin{bmatrix} 0 & 1 & 1 \\ 1 & 0 & 0 \\ 1 & 0 & 0 \end{bmatrix}, \quad S_y = \frac{i\hbar}{\sqrt{2}} \begin{bmatrix} 0 & 1 & -1 \\ -1 & 0 & 0 \\ 1 & 0 & 0 \end{bmatrix}, \quad S_z = \hbar \begin{bmatrix} 0 & 0 & 0 \\ 0 & -1 & 0 \\ 0 & 0 & 1 \end{bmatrix}$$

We have designed the experiment such that $B_z \approx 0$. Further, since we are only addressing one of the possible transitions, with the other being far detuned, we restrict our attention to the transition between $|0\rangle$ and $|-1\rangle$. Then, if $\vec{B}(t) = \vec{B} \cos(\omega t)$, we are left with the familiar interaction term,

$$H_I = \frac{\hbar}{2} \begin{bmatrix} 0 & \Omega & 0 \\ \Omega^* & 0 & 0 \\ 0 & 0 & 0 \end{bmatrix} \cos(\omega t),$$

where $\Omega = \sqrt{2}g\mu_B (B_x + iB_y) / \hbar$ is the Rabi frequency. One can then go through the usual procedure of moving into the interaction picture, followed by making the rotating wave approximation [27] to obtain the interaction Hamiltonian,

$$H_I = \frac{\hbar}{2} \begin{bmatrix} 0 & \Omega e^{i\delta t} & 0 \\ \Omega^* e^{-i\delta t} & 0 & 0 \\ 0 & 0 & 0 \end{bmatrix},$$

This can be converted into a time independent Hamiltonian by moving into the rotating frame via the unitary transformation given by, $V(t) = \text{diag}(1, e^{-i\delta t}, 1)$, to obtain,

$$\tilde{H}_I = \frac{\hbar}{2} \begin{bmatrix} 2\delta & \Omega & 0 \\ \Omega^* & 0 & 0 \\ 0 & 0 & 0 \end{bmatrix} \quad (4.1)$$

Recall that the theory for the quantum heat engine is most easily done in the so called Liouville space, in which we vectorise the density matrix, and can write the Lindblad equation as a matrix equation. The interaction Hamiltonian Eq. 4.1 can be used to find the corresponding interaction Hamiltonian in Liouville space. If we work in the basis $\{\rho_{13}, \rho_{23}, \rho_{31}, \rho_{32}, \rho_{12}, \rho_{21}, \rho_{11}, \rho_{22}, \rho_{33}\}$, it takes the form,

$$\mathcal{H}_w = \begin{bmatrix} \mathcal{H}_1 & & & \\ & -\mathcal{H}_1 & & \\ & & \mathcal{H}_2 & \\ & & & 1 \end{bmatrix}, \quad (4.2)$$

$$\mathcal{H}_1 = \frac{1}{2}\hbar \begin{bmatrix} \delta & \Omega \\ \Omega & 0 \end{bmatrix} \quad \text{and} \quad \mathcal{H}_2 = \frac{1}{2}\hbar \begin{bmatrix} 2\delta & 0 & -\Omega & \Omega \\ 0 & 2\delta & \Omega & -\Omega \\ -\Omega & \Omega & 0 & 0 \\ \Omega & -\Omega & 0 & 0 \end{bmatrix}$$

Given some inhomogeneous distribution, \mathcal{N} , the procedure is to simply calculate the power output for each detuning, which is then integrated over the distribution to give the ensemble averaged output:

$$\langle P \rangle = \int P(\delta) \mathcal{N}(\delta) d\delta$$

Action

Recall that the action is the variable which parametrizes the relative effect of the engine cycle on the state of the system, and we only expect to observe quantum effects when the action is less than \hbar . Recall that, working in the Liouville space interaction picture with $i\hbar\partial_t |\rho\rangle = \mathcal{H} |\rho\rangle$, the action of the engine is given by,

$$s = \int_0^T \|\mathcal{H}(t)\| dt,$$

where the matrix norm used is the spectral norm, which is given by,

$$\|M\| = \max \left\{ \sqrt{\text{eig}(MM^\dagger)} \right\}$$

We begin by considering how this quantity changes when we introduce detuning. In the case of zero detuning the coherent contribution to the action is simply given by $s_{coh} = \Omega t_{coh}$, where Ω is the Rabi frequency of the driving field. Naively one might expect the action to increase when a detuning is introduced, since the Rabi frequency gets replaced by the modified Rabi frequency: $\Omega \rightarrow \sqrt{\Omega^2 + \delta^2}$; on the other hand, intuitively we would expect the action to decrease, since the interaction strength diminishes as one detunes far from resonance.

The definition of the action given above originates from a consideration of the unitary evolution operator in the interaction picture, which, in the simplest case of a constant Hamiltonian, is given by $\exp(\mathcal{H}_I t)$. The results in [27] follow from the argument of the exponential being 'small', so we will follow this approach. The problem with simply replacing the Rabi frequency with the generalised Rabi frequency is that we have then implicitly transformed into the rotating frame. Instead, using the expression for the time-independent interaction Hamiltonian 4.1, it can be shown that the interaction picture unitary evolution operator is given by,

$$U(t) = V(t)^\dagger e^{-\frac{i}{\hbar} \tilde{H}_I t} = \begin{bmatrix} X(t) & Y(t) & 0 \\ -Y(t)^* & X(t)^* & 0 \\ 0 & 0 & 1 \end{bmatrix},$$

where,

$$X(t) = e^{i\delta t/2} \left[\cos\left(\frac{1}{2}\tilde{\Omega}t\right) - i\frac{\delta}{\tilde{\Omega}}\sin\left(\frac{1}{2}\tilde{\Omega}t\right) \right] \text{ and } Y(t) = -i(\Omega/\tilde{\Omega})e^{i\delta t/2}\sin\left(\frac{1}{2}\tilde{\Omega}t\right),$$

and where $\tilde{\Omega} = \sqrt{\Omega^2 + \delta^2}$ is the modified Rabi frequency. The unitary evolution operator in Liouville space is given by $K = U \otimes U^*$. Since U is unitary, we can find a Hermitian matrix M such that $U = \exp(iM)$; this together with the identity, $\exp(A) \otimes \exp(B) = \exp(A \otimes \mathbb{I} + \mathbb{I} \otimes B)$, allows us to write

$$K = \exp \left[i \left(M \otimes \mathbb{I} - \mathbb{I} \otimes M^T \right) \right]$$

and consequently define the action to be,

$$s_{coh} \equiv \|M \otimes \mathbb{I} - \mathbb{I} \otimes M^T\| \quad (4.3)$$

The eigenvalues of M^T are equal to those of M . Note too that the eigenvectors of $M \otimes \mathbb{I} - \mathbb{I} \otimes M^T$ are of the form $x_i \otimes y_i$, where x_i are the right eigenvectors of M and y_i are the left eigenvectors. Therefore the eigenvalues of this matrix are simply given by $(\lambda_k - \lambda_j)$ where λ_i are the eigenvalues of M . It can readily be established that the eigenvalues of U are given by,

$$\lambda = 1, \quad \mathcal{Re}(X) \pm i\sqrt{1 - \mathcal{Re}(X)^2}$$

$|X|^2 + |Y|^2 = 1 \implies |\mathcal{Re}(X)| \leq 1$, so we can write these eigenvalues as $\{1, \exp(-i\theta), \exp(i\theta)\}$, where

$$\theta = \arccos \left[\cos \left(\frac{1}{2} \delta t \right) \cos \left(\frac{1}{2} \tilde{\Omega} t \right) + \frac{\delta}{\tilde{\Omega}} \sin \left(\frac{1}{2} \delta t \right) \sin \left(\frac{1}{2} \tilde{\Omega} t \right) \right],$$

Our action is then simply given by

$$s_{coh} = 2 \arccos \left[\cos \left(\frac{1}{2} \delta t_w \right) \cos \left(\frac{1}{2} \tilde{\Omega} t_w \right) + \frac{\delta}{\tilde{\Omega}} \sin \left(\frac{1}{2} \delta t_w \right) \sin \left(\frac{1}{2} \tilde{\Omega} t_w \right) \right] \quad (4.4)$$

Note that this simply reduces to Ωt_{coh} if we take $\delta = 0$ (as it should). In Fig. 4.1 and Fig. 4.2 we plot this function for parameters similar to those used in the experiment.

Fig. 4.1 shows that the action does decrease with increasing detuning, albeit slowly; in fact we see that it only changes by a few percent for the stroke durations used (10ns - 60ns) and range of detunings present in our experiment. Fig. 4.2 shows the

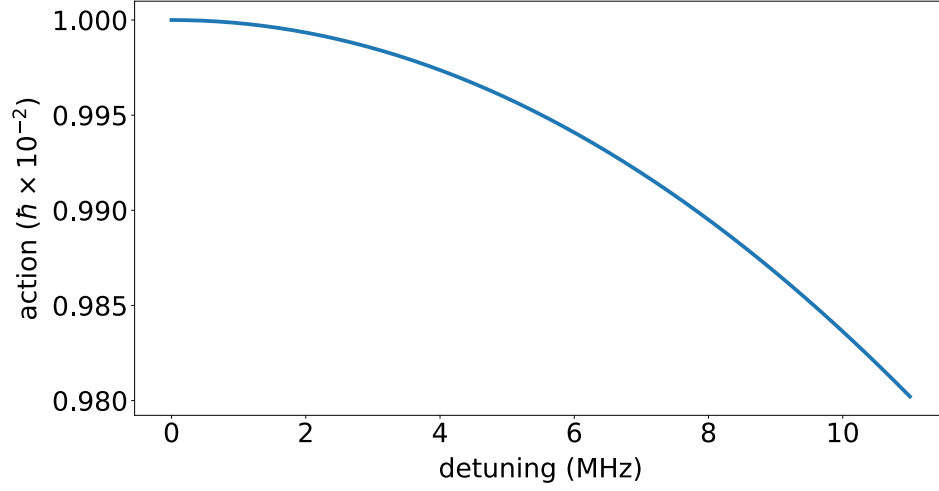


Figure 4.1: coherent action as a function of detuning for $\Omega = 1$ MHz and $t_{coh} = 20$ ns

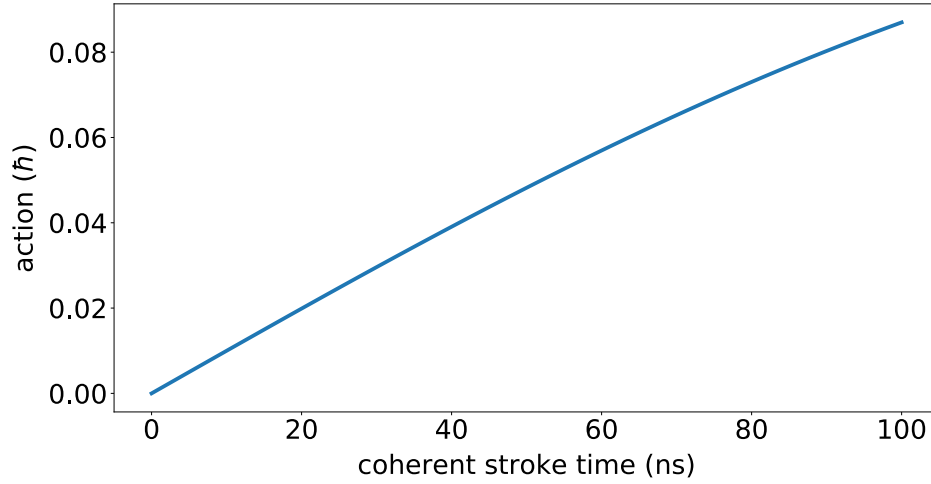


Figure 4.2: averaged coherent action as a function of coherent stroke time for $\Omega = 1$ MHz and $\sigma = 3.0$ MHz

ensemble averaged action, for an inhomogeneous broadening of $\sigma = 3$ MHz, which is linear with time for small time durations, but has non-linear additions as the cycle duration is increased. These details aren't especially important for the purposes of this experiment – all that concerns us is that the action is small across the ensemble, which can be ensured by choosing the Rabi frequency and stroke duration such that the action is small at zero detuning.

Now consider the thermal contribution to the action. Recall that the thermal evolution operator is given by 3.1. The hot reservoir has $\gamma_{13}, \gamma_{31} > 0$, with all other entries zero. Similarly so for the cold reservoir with $\gamma_{23}, \gamma_{32} > 0$. These rates determine both the thermalisation coupling strengths and the temperatures of the respective reservoirs, with the latter given in terms of the Boltzman factors, $\gamma_{31}/\gamma_{13} = \exp(-\Delta E_h/kT_h)$ and $\gamma_{32}/\gamma_{23} = \exp(-\Delta E_c/kT_c)$. Consider the hot coupling first:

$$\mathcal{L}^h = i\hbar \begin{bmatrix} -\frac{1}{2}(\gamma_{13} + \gamma_{31})\mathbb{I} & & & & \\ & -\frac{1}{2}\gamma_{31}\mathbb{I} & & & \\ & & -\frac{1}{2}\gamma_{31}\mathbb{I} & & \\ & & & -\gamma_{31} & 0 & \gamma_{13} \\ & & & 0 & 0 & 0 \\ & & & \gamma_{31} & 0 & -\gamma_{13} \end{bmatrix},$$

Neglecting the factor of $i\hbar$, this matrix has distinct eigenvalues

$$\left\{ 0, -\frac{1}{2}\gamma_{31}, -\frac{1}{2}\gamma_{31}, -\frac{1}{2}(\gamma_{13} + \gamma_{31}), -(\gamma_{13} + \gamma_{31}) \right\}$$

$$\therefore \|\mathcal{L}^h\| = \hbar(\gamma_{13} + \gamma_{31})$$

The calculation for \mathcal{L}^c is identical with the change $1 \leftrightarrow 2$, so that

$$\|\mathcal{L}^c\| = \hbar(\gamma_{23} + \gamma_{32})$$

So finally we can state that a sufficient condition for working in the small action regime is,

$$s/\hbar \leq \Omega t_w + (\gamma_{13} + \gamma_{31} + \gamma_{23} + \gamma_{32}) t_{th} \ll 1,$$

where we have used $s_{coh}(t) \leq \hbar\Omega t_w$ and $\|A + B\| \leq \|A\| + \|B\|$.

Quantum Bound

We also need to consider the effect of the detuning on the stochastic bound. Recall that the stochastic work per stroke is given by,

$$W_{stoch} = -\langle H_0 | \mathcal{D} \left[e^{-\frac{i}{\hbar} \mathcal{H}_w t_w} - \mathbb{I} \right] \mathcal{D} |\tilde{\rho}\rangle,$$

where \mathcal{H}_w is given by 4.2. Define $|\tilde{\rho}_{\text{pop}}\rangle = \mathcal{D} |\tilde{\rho}\rangle$, which is simply the projection of the steady state, $|\tilde{\rho}\rangle$, onto the population subspace (i.e just setting all the coherences to zero). Note too that $\langle H_0 | \mathcal{H}_w^n |\tilde{\rho}_{\text{pop}}\rangle = 0$ for n even, so that we can write,

$$W_{stoch} = \frac{t_w^2}{2\hbar^2} \langle H_0 | \mathcal{H}_w^2 |\tilde{\rho}_{\text{pop}}\rangle + \mathcal{O}((s/\hbar)^4) \quad (4.5)$$

We see that, by virtue of both $|\tilde{\rho}_{\text{pop}}\rangle$ and $|H_0\rangle$ consisting population terms alone, only the bottom right 3×3 block of \mathcal{H}_w^2 contributes to 4.5, and is given by:

$$\mathcal{H}_w^2 = \frac{1}{2} \hbar^2 \Omega^2 \begin{bmatrix} 1 & -1 & 0 \\ -1 & 1 & 0 \\ 0 & 0 & 0 \end{bmatrix}$$

Substituting this back into 4.5 we get

$$W_{stoch} = \frac{1}{4} t_w^2 \Omega^2 [0, \hbar\omega_{12}, \hbar\omega_{13}] \begin{bmatrix} 1 & -1 & 0 \\ -1 & 1 & 0 \\ 0 & 0 & 0 \end{bmatrix} \begin{bmatrix} \rho_{11} \\ \rho_{22} \\ \rho_{33} \end{bmatrix}$$

$$= \frac{1}{4} \hbar \omega_{12} t_w^2 \Omega^2 (\rho_{22} - \rho_{11}) \leq \frac{1}{4} \hbar \omega_{12} t_w^2 \Omega^2$$

Thus the photon emission rate of an engine with duty cycle d is bounded by:

$$R_{stoch} \leq \frac{1}{4} d |\Omega|^2 t_w \quad (4.6)$$

Therefore the addition of a detuning does not affect the bound derived previously.

This is not entirely true if we consider higher order terms – including these we obtain,

$$R_{stoch}(\delta) \leq \frac{1}{4} d |\Omega|^2 t_w \left[1 - \frac{t_w^2}{24} (\Omega^2 + 2\delta^2) + \dots \right]$$

Averaging over a normal distribution with variance σ yields,

$$R_{stoch} \leq \frac{1}{4} d |\Omega|^2 t_w \left[1 - \frac{t_w^2}{24} (\Omega^2 + 2\sigma^2) + \dots \right]$$

The additional term can become significant provided σt_w is not too small. Using physically realistic parameters from the experiment ($\Omega \sim 1$ MHz, $\sigma \sim 2\pi \times 3$ MHz and $t_w = 10$ ns), we find this expression differs from 4.6 by only 0.3%; however, if we take $t_w = 50$ ns, then it is reduced by 8%.

Detuning from resonance is not the only way in which our experiment differs from the assumptions under which the original bound was derived. First, note that the system is not decoupled from the effective thermal bath when the optical excitation is turned off – instead all three ground levels are weakly coupled to the singlet by a cold bath. In addition the pulse shapes are not perfectly square. Under these conditions we have to consider the following expression,

$$\begin{aligned}
W_{stoch} &= \frac{i}{\hbar} \int_0^T dt \langle H_0 | \mathcal{H}_w(t) U(t) | \tilde{\rho}_{\text{pop}} \rangle \\
&= \frac{i}{\hbar} \int_0^T dt \langle H_0 | \mathcal{H}_w(t) \mathcal{T} \left\{ e^{-\frac{i}{\hbar} \int_0^t d\tau (\mathcal{H}_w(\tau) + \mathcal{L}(\tau))} \right\} | \tilde{\rho}_{\text{pop}} \rangle \\
&= \frac{i}{\hbar} \int_0^T dt \langle H_0 | \mathcal{H}_w(t) \left[\mathbb{I} - \frac{i}{\hbar} \int_0^t d\tau (\mathcal{H}_w(\tau) + \mathcal{L}(\tau)) + \mathcal{O}(t^2) \right] | \tilde{\rho}_{\text{pop}} \rangle
\end{aligned}$$

The term $\langle H_0 | \mathcal{H}_w(t) | \tilde{\rho}_{\text{pop}} \rangle$ vanishes as before, as does $\langle H_0 | \mathcal{H}_w(t) \mathcal{L}(\tau) | \tilde{\rho}_{\text{pop}} \rangle$, since \mathcal{L} does not mix population and coherence terms. So we are left with,

$$W_{stoch} = \frac{1}{\hbar^2} \int_0^T dt \int_0^t d\tau \langle H_0 | \mathcal{H}_w(t) \mathcal{H}_w(\tau) | \tilde{\rho}_{\text{pop}} \rangle$$

We know that we can neglect the detuning terms for the same reasoning as used previously.

$$\therefore W_{stoch} = \frac{1}{2} \langle H_0 | \begin{bmatrix} 1 & -1 & 0 \\ -1 & 1 & 0 \\ 0 & 0 & 0 \end{bmatrix} | \tilde{\rho}_{\text{pop}} \rangle \int_0^T dt \int_0^t d\tau \Omega(t) \Omega(\tau)$$

Also note that $\int_0^T dt \int_0^t d\tau \Omega(t) \Omega(\tau) = \frac{1}{2} T^2 \langle \Omega \rangle^2$.

$$\therefore W_{stoch} \leq \frac{1}{4} \hbar \omega_{12} T^2 \langle \Omega \rangle^2$$

$$\therefore P_{stoch} \leq \frac{1}{4} \hbar \omega_{12} T \langle \Omega \rangle^2$$

We see that this is simply a slightly generalised version of the previously derived expression, reducing to it in the case of a square pulse.

4.1.2 Homogeneous dephasing

The idealised theory includes two mechanisms for decoherence. The first occurs when the reservoirs are coupled to the system, which results in loss of coherence due to incoherent population transfer. The second mechanism is the theoretical construct, \mathcal{D} , an operator which completely eliminates the coherences of the state to which it is applied. This idealised theory neglects the fact that we can never completely decouple the system from its environment, even assuming we can controllably couple the reservoirs perfectly. It also does not consider decoherence mechanisms which do not result from population transfer – these are the mechanisms which result in the coherence time, T_2 , being less than half the lifetime ($2T_2 \leq T_1$).

One of the well known features of the negative NV centre, and one of the principle reasons for the attention it has received, is the fact that it is possible to obtain very long T_2 times between the ground spin states, even at room temperature. T_2 depends on several factors related to the diamond properties and environment, including temperature and defect density. The mechanisms principally responsible for decoherence in the NV centre include it being coupled to the diamond lattice; and, more importantly for dense ensembles, coupling to other centres and paramagnetic impurities in its neighbourhood [60]. Measurements of T_2 for room temperature ensembles range from $\sim 1\mu s$ to over $600\mu s$, with a few μs being typical.[50, 49]. Measurements of T_2 as high as $600 ms$ have been measured when using low temperatures ($77K$) and dynamic decoupling techniques [51]. The characteristic timescale resulting from these spin-spin interactions between the NV and neighbouring paramagnetic impurities is

given by [74],

$$T_2 \approx 1/\alpha n,$$

where $\alpha = \mu_0 g_s^2 \mu_B^2 / 4\pi\hbar$ and n is the density of NV centres. The density of the NV^- centres in our sample is approximately $1 \times 10^{18} \text{cm}^{-3}$. Substituting this into the formula gives $T_2 = 4.4 \mu\text{s}$, which is consistent with previously measured rates.

It is relatively simple to include homogeneous dephasing in our model of the NV heat engine. We are coherently driving only one of the possible microwave transitions, which allows us to restrict our attention to the coherence between these two levels. Dephasing at a rate γ is then simply included in the form of exponential decay terms acting on these coherences. Recall that the Hamiltonian is given by 4.2, and that we may restrict our attention to $\mathcal{H}_2 \oplus 0$:

$$\mathcal{H} = \frac{1}{2}\hbar \begin{bmatrix} 2\delta & 0 & -\Omega & \Omega & 0 \\ 0 & 2\delta & \Omega & -\Omega & 0 \\ -\Omega & \Omega & 0 & 0 & 0 \\ \Omega & -\Omega & 0 & 0 & 0 \\ 0 & 0 & 0 & 0 & 0 \end{bmatrix}$$

The homogeneous dephasing is then simply included by hand through the addition of the phenomenological pure dephasing term \mathcal{L}_D ,

$$i\hbar\partial_t |\rho\rangle = \mathcal{H}(t) |\rho\rangle ,$$

where $\mathcal{H}(t) = \mathcal{H}_\omega(t) + \mathcal{L}_{th}(t) + \mathcal{L}_D$, $\mathcal{L}_{th}(t)$ is the Liouville operator describing the coupling to the thermal baths and \mathcal{L}_D is the pure dephasing operator, given by,

$$\mathcal{L}_D = i\hbar \begin{bmatrix} -\gamma & & & \\ & -\gamma & & \\ & & 0 & \\ & & & 0 \\ & & & & 0 \end{bmatrix}$$

Given the work presented in [27], it would be natural to assume that the inclusion of any homogeneous dephasing will reduce the power output of the engine. However, when I reran calculations with this addition, I found that this wasn't necessarily the case. Fig. 4.3 shows a plot of the engine power output as a function of the inhomogeneous dephasing rate for $\Omega = 2\pi \times 0.25$ MHz, $\Gamma = 0.75$ MHz, $t_w = 20$ ns, $d = 1/3$, and $\sigma = 2\pi \times 3$ MHz.

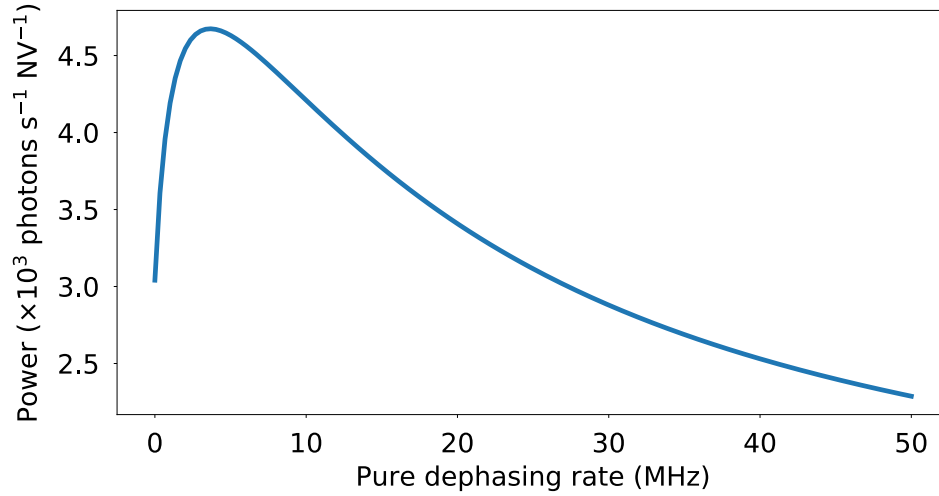


Figure 4.3: Figure illustrating the effect of pure dephasing on the power output of an inhomogeneously broadened ensemble. In particular notice the sharp initial increase in power before a turning point and gradual decrease.

We see a sharp initial increase in the power output, with a maximum occurring at ~ 3.5 MHz, followed by a more gradual decrease in the power. Fig. 4.3 uses the range 0 – 50 MHz in order to demonstrate the initial increase, followed by the turnover and

decrease with increasing dephasing. Based on the previously measured numbers, and the estimate for T_2 , this range is too large, so we restrict it such that ($1\mu s \leq T_2$) (shown in Fig. 4.4). This slightly surprising result turns out to be linked to the inhomogeneous dephasing, in that it is only apparent when $\sigma > 0$. This is shown in Fig. 4.5, which plots the power for the same parameters as before, but with $\sigma = 0$ MHz. In this we see that the power decreases monotonously in the on-resonance case; in addition, a comparison of the y-axis scale to that of Fig. 4.3, demonstrates the extent to which the inhomogeneous broadening reduces power output of the engine. The behaviour demonstrated in Fig. 4.3 begs the question as to why this does not contradict the results from [27]. This is resolved by noting that [27] does not show that coherence must always result in a power boost; rather it shows that any engine which does not carry coherence from one cycle to the next is bound in its power output, so that an engine producing more power is indicative of this coherence being preserved between cycles. Thus coherence can result in a power boost in certain circumstances, but is not guaranteed to in all circumstances.

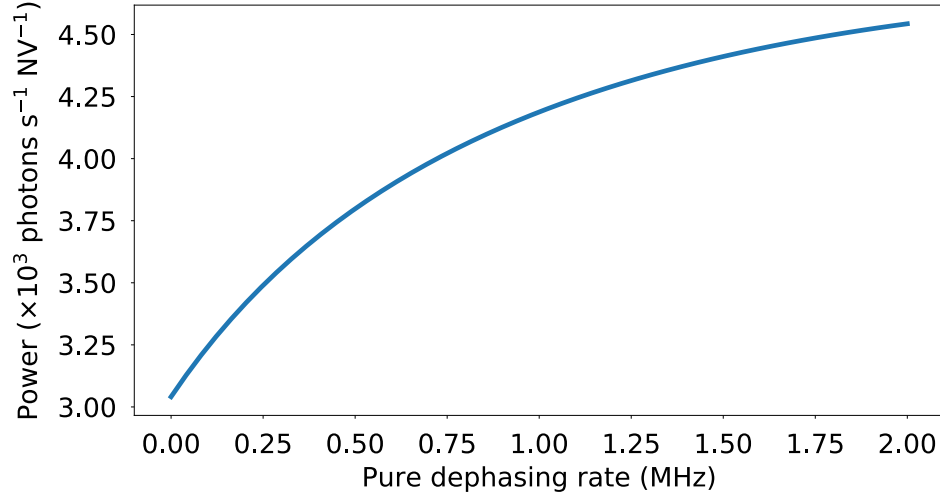


Figure 4.4: Figure showing the

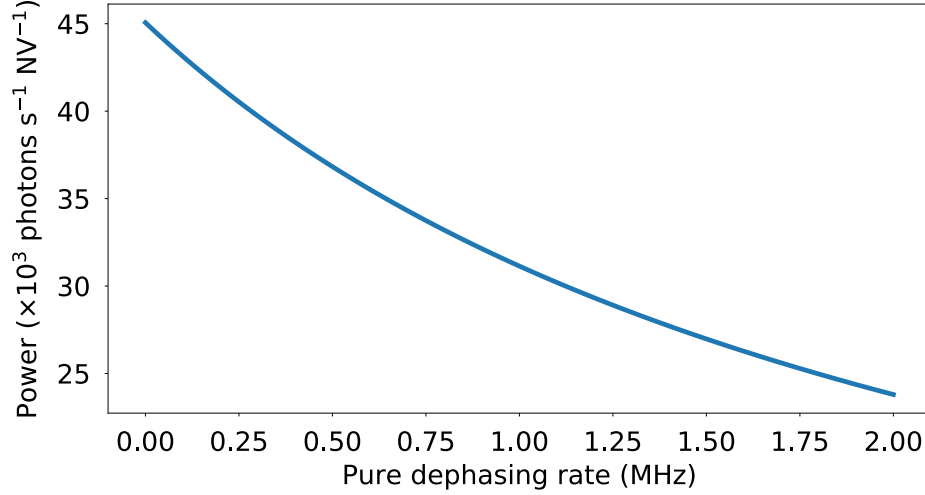


Figure 4.5: The effect of pure dephasing on a single in resonance engine. Note in this case the effect is only to decrease the power output.

4.1.3 Theoretical predictions

I now show how to use the constructs presented previously to calculate predicted power outputs, steady state cycles, heat flows and other quantities of interest. We are principally interested in the steady state power output. The procedure used to calculate this consists of two distinct steps: first the steady state of the engine needs to be determined, after which the work done on this state during the course of a single stroke can be calculated. In the section discussing the stochastic bound, the interaction Hamiltonian was presented; because the unitary Hamiltonian only couples the states $|1\rangle$ and $|2\rangle$, we can neglect the other coherence terms and restrict to $\{\rho_{12}, \rho_{21}, \rho_{11}, \rho_{22}, \rho_{33}\}$. The equation we are attempting to solve is simply the Schrodinger equation, but for the unitary evolution operator in the super-operator (Liouville) picture,

$$i\hbar \partial_t U = \mathcal{H}U; \quad U(0) = \mathbb{I}, \quad (4.7)$$

where $\mathcal{H} = \mathcal{H}_\omega + \mathcal{L}$, and where the thermal evolution operator, \mathcal{L} , is calculated as shown in 3.2 (with a factor of $i\hbar$ included). The steady state is calculated by determining the zero eigenvector of the full cycle unitary evolution operator, $U(T)$. Then, given the steady state $|\rho\rangle$, the work output is given by,

$$W = \langle H_0 | \hat{W} | \rho \rangle, \text{ where } \hat{W} = -\frac{i}{\hbar} \int_0^T \mathcal{H}_\omega(\tau) U(\tau) d\tau$$

We can also consider the heat flows in the engine. Similarly, the total flow into engine from the cold (hot) reservoir is given in terms of the operators,

$$\hat{Q}_{c(h)} = -\frac{i}{\hbar} \int_0^T \mathcal{L}_{c(h)}(\tau) U(\tau) d\tau,$$

We can check that energy conservation still holds:

$$\begin{aligned} \hat{W} + \hat{Q}_c + \hat{Q}_h &= -\frac{i}{\hbar} \int_0^T (\mathcal{H}_\omega + \mathcal{L}_c + \mathcal{L}_h)(\tau) U(\tau) d\tau \\ &= -\frac{i}{\hbar} \int_0^T \mathcal{H}(\tau) U(\tau) d\tau = \int_0^T \partial_\tau U(\tau) d\tau = 0 \end{aligned}$$

The final step has used the fact that $U(t)$ is periodic with period T . Also recall the efficiency is given by the ratio of the work done to the heat flow into the engine,

$$\eta = \frac{W}{Q_h}$$

So, in order to calculate the power output, our problem boils down to calculating U and \hat{W} . We consider three distinct cases: the ideal case (able to perfectly decouple the thermal baths during the work stroke), the perfectly square pulse case, and finally the general case. In the ideal case of perfectly square pulses and no overlap between the thermal and work couplings, these quantities can be calculated analytically. The

unitary evolution operator is simply given by,

$$U(t) = \begin{cases} e^{-\frac{i}{\hbar}t\mathcal{H}_\omega} & t \leq t_\omega \\ e^{-\frac{i}{\hbar}(t-t_\omega)\mathcal{L}}e^{-\frac{i}{\hbar}t_\omega\mathcal{H}_\omega} & t \geq t_\omega \end{cases}$$

And

$$\hat{W} = -\frac{i}{\hbar} \int_0^T \mathcal{H}_\omega(\tau) e^{-\frac{i}{\hbar}\tau\mathcal{H}_\omega} d\tau = e^{-\frac{i}{\hbar}\mathcal{H}_\omega t_\omega} - \mathbb{I}$$

In the case where we cannot completely decouple the system from the thermal reservoirs and its environment, but assume that we are still able to apply perfectly square pulses – by which I mean that the Hamiltonian is constant during each stroke – the unitary operator is given by,

$$U(t) = \begin{cases} e^{-\frac{i}{\hbar}t(\mathcal{H}_\omega + \mathcal{L}(\Gamma=0))} & t \leq t_\omega \\ e^{-\frac{i}{\hbar}(t-t_\omega)\mathcal{L}(\Gamma)}e^{-\frac{i}{\hbar}t_\omega\mathcal{H}_\omega} & t \geq t_\omega \end{cases}$$

Calculating the integral for \hat{W} ,

$$\hat{W} = -\frac{i}{\hbar} \int_0^T \mathcal{H}_\omega(\tau) e^{-\frac{i}{\hbar}\tau(\mathcal{H}_\omega + \mathcal{L}(\Gamma=0))} d\tau,$$

is no longer quite so trivial. The difficulty here lies in the fact that $\mathcal{H}_\omega + \mathcal{L}(\Gamma = 0)$ is singular. The simplest way to deal with this is to diagonalise $\mathcal{H}_\omega + \mathcal{L}(\Gamma = 0)$ and perform the integration component-wise.

Finally, consider the most general case, where the pulses are non-square and where there is overlap between the work and thermal couplings. Then the unitary is given by the time-ordered exponential:

$$U(t) = \mathcal{T} \exp \left[-\frac{i}{\hbar} \int_0^t \mathcal{H} d\tau \right],$$

which is defined in terms of Dyson series:

$$U(t) = \mathbb{I} + \int_0^t d\tau_1 \mathcal{H}(\tau_1) + \int_0^t \int_0^{\tau_1} d\tau_1 d\tau_2 \mathcal{H}(\tau_1) \mathcal{H}(\tau_2) + \dots$$

Instead of attempting to calculate this series I numerically solve equation 4.7 directly using the 4th order Runge-Kutta method. To do this, measurements of the traces for both the Rabi frequency and optical excitation are taken, and then iterated over using the following procedure:

$$\delta t \leftarrow t_n - t_{n-1}$$

$$H_1 \leftarrow H_2$$

$$H_2 \leftarrow \mathcal{H}(\Gamma_n, \Omega_n, \delta)$$

$$k_1 \leftarrow H_1 U$$

$$k_2 \leftarrow 0.5 (H_1 + H_2) (U + 0.5 k_1 \delta t)$$

$$k_3 \leftarrow 0.5 (H_1 + H_2) (U + 0.5 k_2 \delta t)$$

$$k_4 \leftarrow H_2 (U + k_3 \delta t)$$

$$U \leftarrow U + \frac{\delta t}{6} (k_1 + 2k_2 + 2k_3 + k_4)$$

$$W \leftarrow W + i \delta t k_1$$

This is a forth order technique, which is correct up to $\mathcal{O}(\delta t^5)$ for each step, and $\mathcal{O}(\delta t^4)$ for accumulated error. Identical techniques can be used to calculate the heat flows.

4.2 Experimental Results

Here the central results of this thesis are presented, namely the empirical verification of the existence of a quantum thermodynamic signature in the operation of a quantum heat engine, and a demonstration of the thermodynamics equivalence between continuous and 2-stroke variants of quantum heat engines in the small action limit.

4.2.1 Stochastic Bound

A measurement of the quantum thermodynamic signature requires not only that the power output of the two-stroke engine be measured, but also that the corresponding stochastic bound be calculated. Since the power of a fully stochastic engine is constrained to lie below this bound for small actions, any measured output exceeding the bound is indicative of quantum effects. The bound is not measured, but is calculated using Eq. 4.5 – this expression does depend on the Rabi frequency in question which is a measured quantity. Because the engine output scales roughly linearly with Rabi frequency at fixed cycle time, whilst the bound scales quadratically, we expect to be able to more easily measure QTS at the lower end of our Rabi frequency range.

This scaling resulted in the lowest Rabi frequency for which the signal to noise ratio was still sufficiently large being chosen. The Rabi frequency at which we were finally able to measure a quantum thermodynamic signature, as shown in Fig. 4.6, was $\Omega = 1.6 \pm 0.05$ Mrad/s. In our case the coherent duty cycle was fixed to be 33% due to our limited peak optical power, which allowed us to more evenly match the thermal and coherent actions. The total cycle time was scanned across the range (30 - 180)ns. Finally, the thermal bath coupling rate was determined to be $\gamma_{th} = 0.41 \pm 0.02$ MHz.

Due to the low signal at these driving strengths, each data point was obtained by integrating using a lock-in amplifier for approximately 4×10^3 cycles, and was repeated

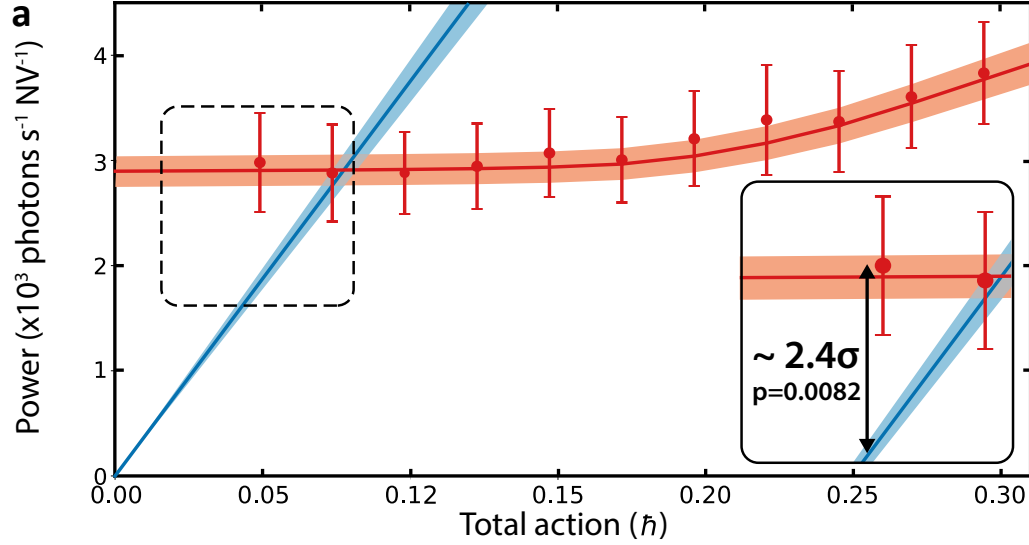


Figure 4.6: Beating the stochastic bound: Measured power output of the two-stroke engine (dots) vs. the action per cycle, theoretically predicted power (red line) and stochastic bound (solid blue line).

20 times for each point. The results are shown in Fig. 4.6. The stochastic bound corresponding to this Rabi frequency and duty cycle is given by the blue line. It is clearly seen that for the smallest action applied, corresponding to a coherent stroke time of 10ns, the bound is violated by 2.4 standard deviations, corresponding to a p value of 0.0082 (see subsec 4.2.4 for a detailed discussion of the error analysis).

4.2.2 Equivalence

The equivalence between the two-stroke and continuous engines was the first result we were able to demonstrate with the experimental setup. It can be seen that the equivalence hypothesis is equivalent to the following,

$$\lim_{s \rightarrow 0} \frac{P_{stroke}}{P_{cont}} = 1$$

This means that the proportionality constant κ does not need to be determined, and nor do exact values need to be known for the optical excitation rate Γ or Rabi

frequency Ω . This relaxation allows for the specific values of the optical excitation rates and Rabi frequencies to be ignored, but rather simply ensure that they are the correct ratios (given by the duty cycle of the stroke engine) for each of the continuous and two-stroke runs. This in turn allows for the use a multimode fibre to collect the light, which eases the coupling of light into the fibre, and results in light intensities of at least an order of magnitude greater than could be achieved with the single mode fibre, and so correspondingly higher signal strengths. Recall that for a coherent duty cycle of d , the Rabi frequencies and thermalisation rates of the continuous and two-stroke engines should be related by,

$$\Omega_{\text{cont}} = d\Omega_{\text{stroke}} \quad \text{and} \quad \gamma_{\text{cont}} = (1 - d)\gamma_{\text{stroke}} \quad (4.8)$$

Again, the duty cycle was fixed at 33% due to our limited peak optical power, and the total cycle time was scanned accross the range (30 - 180)ns. The results from these multi-mode fibre measurements are shown in Fig. 4.7. For this measurement. This was done for a number of different input microwave powers (Rabi frequencies). The corresponding continuous values were obtained by setting the light intensity and microwave driving according to Eq. 4.8. In this graph the fluorescence change is given as a percentage of the average fluorescence, $\langle F \rangle$, for the engine in question (which are close to being equal because the average optical intensities are equal). In this case the proportionality constant, which differs from that derived in Eq. 3.3 by a factor of $F_{cw}/\langle F \rangle$, is the same for each of the engines. It can clearly been seen that the value for two-stroke engine tends towards the corresponding continuous value as the cycle time (and so coherent action) tends towards zero for each of the Rabi frequencies used.

Additionally, a similar scan was taken with the multi-mode fibre was replaced with a single mode fibre (SMF), the results of which are shown in Fig. 4.8. In this case

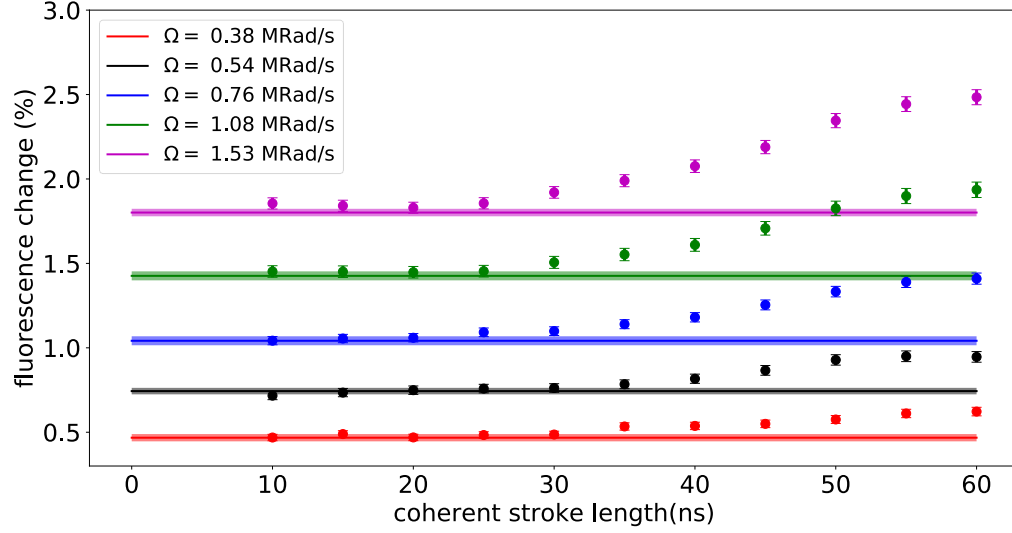


Figure 4.7: An experimental demonstration of the Quantum heat machine equivalence (QHME) collected using a single mode fibre with a laser power of 1mW. The two-stroke power outputs are given by the data points, and the continuous values by the shaded regions.

the proportionality constants linking the normalised fluorescence change and power outputs, together with the optical excitation rate, could be determined. The thermal bath coupling rates were the same as used in the stochastic run, and the duty cycle was again fixed to be $d = 1/3$. The measured values for the two-stroke engine are given by the data points, whilst those for the continuous engine are given by the shaded region, the width of which corresponds to the uncertainty in the measurement. Additionally, because the power output could be calculated in this case, the corresponding theory could be included to compare against – the two-stroke power output is given by the solid lines and the continuous engine by the dashed lines. Despite the increased signal to noise, and the higher total action, the equivalence between the continuous and two-stroke engines are still apparent for the three Rabi frequencies used. It can also be seen that the theory agrees fairly well with the data in both the two-stroke and continuous cases. In examining Fig. 4.8, it can be seen that the errorbars have been somewhat overestimated here; this is because a share of the uncertainty is contributed by the proportionality constant κ , which is equal for each of the data points – this is

discussed more fully in subsection 4.2.4.

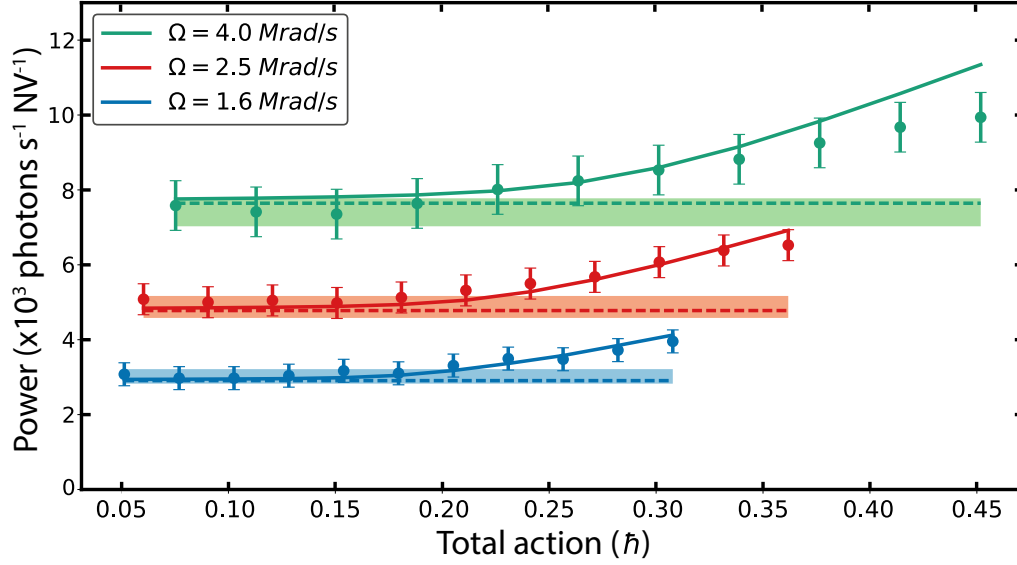


Figure 4.8: An experimental demonstration of the Quantum heat machine equivalence (QHME) collected using a single mode fibre. The two-stroke power outputs are given by the data points, and the continuous values by the shaded regions. The corresponding theoretical predictions are given by the solid and dotted lines respectively.

The results, presented in Fig. 4.7 and Fig. 4.8, showing the convergence in performance constitutes the first experimental verification of quantum heat engine equivalence.

4.2.3 Dephasing

In addition to measuring a QTS, we also sought to study the work output as the coherence of the system was reduced. This was done by fixing the work-stroke duration and Rabi frequency, whilst varying the thermal stroke duration and coupling so as to keep the thermal action constant – this was done by keeping the quantity $\gamma t_{\text{thermal}}$ constant. It is clear that the power output will drop due to increasing the cycle duration without changing either the coherent or thermal actions; to separate

the change in power due to decoherence from this intrinsic power drop, we instead consider the work output per stroke. In this case, provided the thermalisation achieved during the thermal stroke is the same in each case, a stochastic engine should produce the same work per cycle as we vary the stroke duration. Thus, by changing the length of the thermal stroke in this way, only the pure-dephasing related action is increased, enabling the examination of the dependence of the work output on the coherence of the system.

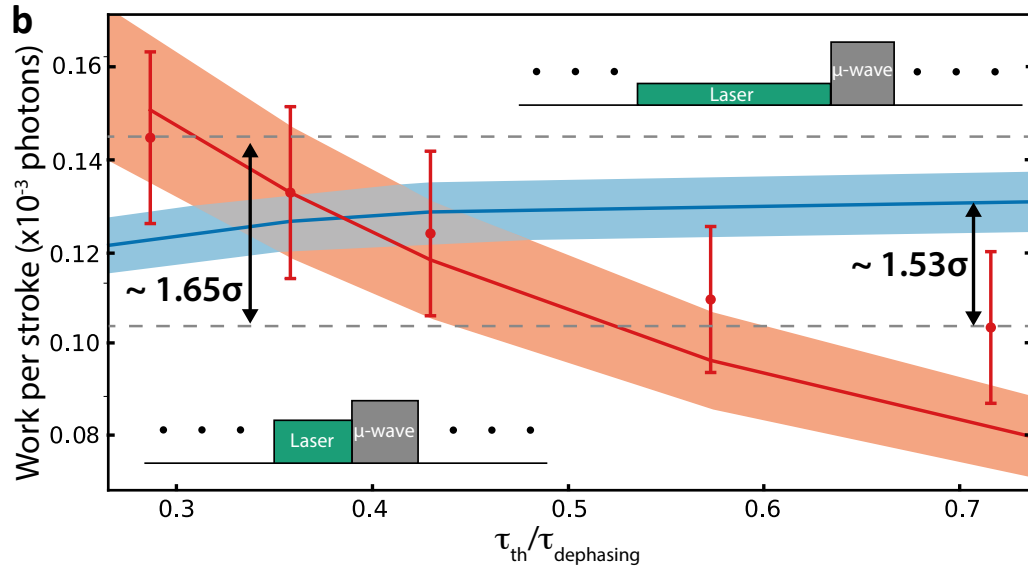


Figure 4.9: Demonstration of the drop in power output as the decoherence is increased. The decoherence was achieved by lengthening the thermal stroke whilst keeping the thermal action fixed.

Fig. 4.9 presents the work per cycle of the two-stroke engine in which the coherent stroke duration and Rabi frequencies were set to their respective minima of 10ns and 1.6MRad/s – this corresponds to a total action per cycle excluding pure dephasing was fixed at $0.05\hbar$. It can clearly be seen that the output work per cycle decreases as the thermal stroke duration is increased, and drops below the stochastic bound (the blue line). The bound increases slightly at long thermal strokes, due the slightly non-square nature of the MW driving. A discrepancy can be observed between theory and

measurement as the thermal stroke is lengthened; I have not been able to determine the exact reason for this at present, but it could possibly be due to the homogeneous dephasing effects discussed in subsec. 4.1.2.

4.2.4 Error analysis

In examining Eq. 3.6, $\langle R \rangle = \kappa \langle \Delta F \rangle / F_{cw}$, it is apparent that there are a number of contributions to the uncertainty in the final value of the rate (power). First, there is measurement variation in the value $\langle \Delta F \rangle$ from one measurement to the next, due to detector shot noise and laser intensity noise. The mean and standard error were simply calculated from the sample of individual measurements. Secondly, the value for κ depends on the parameters listed in table 2.2, together with the value calculated for Γ , which itself depends on the former parameters. I used a Monte-Carlo simulation to propagate the uncertainties in these parameters, and the calculated uncertainty for Γ , to a final uncertainty in κ . The error in the value for $\langle F_{cw} \rangle$ was determined to be negligible (relative error $< 1\%$) relative to the other errors and therefore disregarded. Finally, I also had to account for uncertainty in the value for the bound, which stems from the uncertainty in the value for the Rabi frequency.

When considering the quantum thermodynamic signature, the quantity of interest is the certainty with which we can demonstrate $P_{measured} - P_{bound} > 0$. This requires the use of a one sided normal distribution. The null hypothesis is $P_{measured} - P_{bound} \leq 0$, whilst the alternative hypothesis is that the measured power breaks the stochastic bound. In our case the test statistics for the null outcome is $t = 2.4$, which corresponds to a p-value of 0.0082. Thus we can discard our null hypothesis and adopt the alternative hypothesis, to a significance of $< 1\%$.

Limit Cycles in Quantum Heat Engines

The discussion of the thermodynamic properties of quantum heat engines relies on the engine settling to a steady state operation. Up to this point we have tacitly assumed that the system, driven by periodic external fields, will eventually settle into a steady state operation with well defined power output and dynamics. It seems fairly clear that this will be the case and is therefore perfectly acceptable to assume; however here I will take a slightly closer look at the conditions required for this to be true.

Definition 4. *A dynamical semigroup $\Lambda_t = \exp(\mathcal{L}t)$, with \mathcal{L} as in theorem 1, is said to be relaxing if there exists a density matrix $\rho_\infty \in \mathcal{B}(\mathcal{H})$ such that, for every density matrix $\rho \in \mathcal{B}(\mathcal{H})$,*

$$\lim_{t \rightarrow \infty} \Lambda_t \rho = \rho_\infty.$$

Theorem 3. *Let $\Lambda_t = \exp(t\mathcal{L})$ be a dynamical semigroup of trace preserving CP maps, with \mathcal{L} as in theorem 1 and $t \in \mathbb{R}^+$. Then $\{\Lambda_t\}$ is relaxing if either:*

1. *the algebra generated by $\{L_k | k \in I\}$ is the whole of $\mathcal{M}_d(\mathbb{C})$*
2. *$\text{span}\{L_k | k \in I\}$ is self-adjoint and $\{L_k | k \in I\}'$ contains only multiples of the identity. Here X' denotes the commutant of X .*

Proof. An algebraic condition for the approach to equilibrium of an open N-level system, Herbert Spohn [75]. \square

Definition 5. Suppose we have a $n \times n$ square matrix A_{ij} . Then we say that A is reducible if we can partition the set of indices, $I = \{1, \dots, n\}$, into two disjoint sets, $\{i_1, \dots, i_\mu\}$ and $\{j_1, \dots, j_\nu\}$ (with $\mu + \nu = n$), such that,

$$A_{i_\alpha j_\beta} = 0,$$

for $\alpha \in \{1, \dots, \mu\}$ and $\beta \in \{1, \dots, \nu\}$.

Lemma 1. A $n \times n$ matrix A is irreducible if and only if $I_m = I = \{1, \dots, n\}$ for every $m \in I$, where,

$$I_m = \{n \in I \mid \exists \text{ a sequence } \{i_1 = m, i_2, \dots, i_{k-1}, i_k = n\} \text{ s.t. } A_{i_1 i_2} A_{i_2 i_3} \cdots A_{i_{k-1} i_k} > 0\}$$

Proof.

(\implies) Suppose A is irreducible.

Consider the set $J_m = I - I_m$. Then it is clear that $j \in J_m \implies A_{ij} = 0 \forall i \in I_m$. But we know that I_m is not empty (it must contain m), and since A is irreducible, it follows that $J_m = \emptyset$.

(\impliedby). Assume the property holds and suppose that $A \cup B = I$ is a disjoint partition of the index set. Then for any $a \in A$ and $b \in B$, there exists a sequence $\{i_2, \dots, i_{k-1}\}$ such that,

$$A_{ai_2} A_{i_2 i_3} \cdots A_{i_{k-1} b} > 0.$$

If $i_2 \in B$ then we are done. If not, $i_2 \in A$, and we in turn consider i_3 . We can continue until we eventually find l such that $i_{l-1} \in A$ and $i_l \in B$, which we are assured of since the sequence terminates with $b \in B$. \square

Henceforth we will only consider generators for continuous dynamical semigroups, as in *theorem 1*, for which the operators L_i can be written as $L_{ij} = \sqrt{\gamma_{ij}} |i\rangle \langle j|$. The non-unitary part of the evolution is then characterised entirely by the $d \times d$ matrix γ . The following result (*Corollary 1*) demonstrates that a thermal generator deriving from an irreducible coupling matrix (γ) produces relaxing time evolution. The result is not unknown; however, I present the proof for completeness.

Corollary 1. *Let \mathcal{L} be the generator of a continuous dynamical semigroup with γ being irreducible. Then $\Lambda_t = \exp(t\mathcal{L})$ is relaxing.*

Proof. We show that $\{L_j\}$ generates the whole of $\mathcal{M}_d(\mathbb{C})$ by showing that we can generate a basis for $\mathcal{M}_d(\mathbb{C})$.

Let $m, n \in \{1, \dots, d\}$. Then by *lemma 1*, we can find a sequence i_1, i_2, \dots, i_k , with $i_1 = m$ and $i_k = n$, such that $\gamma_{i_1 i_2} \gamma_{i_2 i_3} \cdots \gamma_{i_{k-1} i_k} > 0$. Then, by writing $r = \gamma_{i_1 i_2} \gamma_{i_2 i_3} \cdots \gamma_{i_{k-1} i_k}$, we have,

$$|m\rangle \langle n| = \frac{1}{r} L_{i_1 i_2} L_{i_2 i_3} \cdots L_{i_{k-1} i_k}.$$

The result follows from *theorem 3*.

□

The more general case, $\partial_t \rho = \mathcal{L}_t \rho$, is more difficult to deal with. We know that, by the equivalence principle, the result should hold true for the general case as the action goes to zero. To proceed I will do away with some of the generality of the previous result and assume a form for the Hamiltonian. Specifically we assume that H only couples two of the levels, which without loss of generality we take to be $|1\rangle$ and $|2\rangle$. First I will state a theorem which we will require later.

Theorem 4. Let $\Lambda : \mathcal{M}_d(\mathbb{C}) \rightarrow \mathcal{M}_d(\mathbb{C})$ be a CPTP map. Then there exists a positive definite density matrix ρ_∞ such that $\lim_{n \rightarrow \infty} \Lambda^n(\rho) = \rho_\infty \quad \forall \rho \in \mathcal{B}(\mathcal{H}) \iff \exists n \in \mathbb{N}$ such that $\Lambda^n(\rho) > 0 \quad \forall \rho \in \mathcal{B}(\mathcal{H})$.

Proof. The Perron - Frobenius theorem [76]. □

Consider density matrices of the form,

$$\rho = \begin{bmatrix} \rho_{11} & \rho_{12} & 0 & \cdots & 0 \\ \rho_{21} & \rho_{22} & 0 & \cdots & 0 \\ 0 & 0 & \rho_{33} & & \vdots \\ \vdots & \vdots & & \ddots & \vdots \\ 0 & 0 & \cdots & \cdots & \rho_{nn} \end{bmatrix}$$

These lie in the subspace spanned by $\{\sigma_{12}, \sigma_{21}, \sigma_{11}, \dots, \sigma_{nn}\}$ – denote it by S .

Lemma 2. Let $\Lambda : \mathcal{M}_d(\mathbb{C}) \rightarrow \mathcal{M}_d(\mathbb{C})$ be a CPTP map such that $\Lambda(S) \subset S$ and $\Lambda(\rho) > 0$ for all density matrices ρ in S . Then there exists a positive definite density matrix $\rho_\infty \in S$ such that

$$\lim_{n \rightarrow \infty} \Lambda^n(\rho) = \rho_\infty \quad \forall \rho \in \mathcal{B}(\mathcal{H}) \cap S.$$

Proof. Let Λ_S be the restriction of Λ to S and let $k = \dim(S)$. Then consider an extension of Λ_S , $\Omega : \mathcal{M}_d(\mathbb{C}) \rightarrow \mathcal{M}_d(\mathbb{C})$, given by

$$\Omega = 0_k \oplus \Lambda_S.$$

It can be seen that Ω is positive and trace preserving and coincides with Λ on S : define a completely positive operator P by the Kraus decomposition $K_0 = |1\rangle\langle 1| + |2\rangle\langle 2|$ and $K_i = |i+2\rangle\langle i+2|$ for $i = 1, \dots, n-2$. Then P is a projector onto

S and $\Omega = P\Lambda$. Also note that $\Omega(\rho) \in S$ for all density matrices ρ . Then since $\Lambda(\rho) > 0 \ \forall \rho \in S \cap \mathcal{B}(\mathcal{H})$, we have $\Omega^2(\rho) > 0$ for all density matrices ρ .

By *theorem 4*, we then have that there exists a positive-definite density matrix, ρ_∞ , such that, for all density matrices ρ ,

$$\lim_{n \rightarrow \infty} \Omega^n(\rho) = \rho_\infty.$$

In particular if $\rho \in S$, then

$$\lim_{n \rightarrow \infty} \Lambda^n(\rho) = \lim_{n \rightarrow \infty} \Omega^n(\rho) = \rho_\infty.$$

Finally we must have $\rho \in S$ by virtue of S being Λ invariant and closed under the usual topology (finite dimensional subspaces must be closed).

□

From the above lemma, it follows that if Λ satisfies the properties in lemma 2 and if for every density matrix ρ there exists $n \in \mathbb{N}$ such that $\Lambda^n(\rho) \in S$, then Λ is relaxing. Working in the basis $\{\rho_{1n}, \dots, \rho_{12}, \rho_{21}, \rho_{11}, \dots, \rho_{nn}\}$ and under the assumption that $L_{ij} = \sqrt{\gamma_{ij}} |i\rangle \langle j|$ and $H = 0$, \mathcal{L} takes the form,

$$\mathcal{L} = \begin{bmatrix} \omega_{1n} & & & & & & & \\ & \ddots & & & & & & \\ & & \omega_{12} & & & & & \\ & & & \omega_{21} & & & & \\ & & & & \omega_{11} & \gamma_{12} & \cdots & \gamma_{1n} \\ & & & & \gamma_{21} & \omega_{22} & & \vdots \\ & & & & \vdots & & \ddots & \vdots \\ & & & & \gamma_{n1} & \cdots & \cdots & \omega_{nn} \end{bmatrix}, \quad (5.1)$$

where $\omega_{ij} = -\frac{1}{2} \sum_k (\gamma_{ki} + \gamma_{kj})$. It is clear, from the block diagonal form of \mathcal{L} , that S is an invariant subspace of \mathcal{L} .

Lemma 3. *Suppose γ is irreducible. Then $\exp(t\mathcal{L})(\rho) > 0$ for all density matrices $\rho \in S$ and $t > 0$*

Proof. We will approach this by considering the action of $\exp(-t\mathcal{L})$ on ρ with non-trivial kernel; so suppose $\det(\rho) = 0$. We consider two cases.

Case I:

Suppose $J = \{m \in I | \rho_{mm} = 0\} \neq \emptyset$. Then $(\mathcal{L}\rho)_{mm} = \sum_{n \in I-J} (\gamma_{mn}\rho_{nn}) > 0$ for some $m \in J$, since γ is irreducible (otherwise we would have $\gamma_{mn} = 0 \forall m \in J, n \in I - J$). So $[(\mathbb{I} - \tau\mathcal{L})\rho]_{mm} < 0$ for all $\tau > 0$. In particular, there exists a $\epsilon > 0$ such that $0 < \tau < \epsilon$ implies

$$[e^{-\tau\mathcal{L}}\rho]_{mm} < 0$$

Case II:

Suppose $\rho_{ii} > 0$ for all $i \in \{1, \dots, n\}$. Then $\rho_{11}\rho_{22} = |\rho_{12}|^2$.

$$(\mathcal{L}\rho)_{11} = \omega_{11}\rho_{11} + \gamma_{12}\rho_{22} + \dots + \gamma_{1n}\rho_{nn}$$

$$(\mathcal{L}\rho)_{22} = \omega_{22}\rho_{22} + \gamma_{21}\rho_{11} + \dots + \gamma_{2n}\rho_{nn}$$

$$(\mathcal{L}\rho)_{12} = \omega_{12}\rho_{12}$$

$$(\mathcal{L}\rho)_{21} = \omega_{21}\rho_{21}$$

$$\therefore \det[(\mathbb{I} - \epsilon\mathcal{L})\rho]_2 = [(1 - \epsilon\omega_{11})\rho_{11} - \epsilon\zeta_1][(1 - \epsilon\omega_{22})\rho_{22} - \epsilon\zeta_2] - (1 - \epsilon\omega_{12})(1 - \epsilon\omega_{21})|\rho_{12}|^2$$

$$\begin{aligned}
&= -\epsilon [(2\omega_{12} - \omega_{11} - \omega_{22}) \rho_{11}\rho_{22} + \rho_{11}\zeta_2 + \rho_{22}\zeta_1] + \mathcal{O}(\epsilon^2) \\
&= -\epsilon (\rho_{11}\zeta_2 + \rho_{22}\zeta_1) + \mathcal{O}(\epsilon^2) \\
&< 0.
\end{aligned}$$

Here I use $\det(A|_k)$ to denote the k th leading principle minor (i.e the determinant of the top left $k \times k$ block) and we have used $\zeta_1 = \gamma_{12}\rho_{22} + \dots + \gamma_{1n}\rho_{nn} > 0$ and $\zeta_2 = \gamma_{21}\rho_{11} + \dots + \gamma_{2n}\rho_{nn} > 0$ (again by the irreducibility of γ). So, again, there exists a $\epsilon > 0$ such that $0 < \tau < \epsilon$ implies

$$\det[e^{-\tau\mathcal{L}}\rho|_2] < 0.$$

Note that a matrix is positive definite iff its leading principal minors are all positive. Thus if $\det(\rho) = 0$, then for sufficiently small $\epsilon > 0$, $e^{-\tau\mathcal{L}}\rho$ is not positive semi-definite for $0 < \tau < \epsilon$. This implies the result as follows: suppose there is a density matrix σ such that $e^{t\mathcal{L}}\sigma = \rho$ for some $t > 0$. Then by taking $0 < \tau < \min(\epsilon, t)$, it follows that $e^{(t-\tau)\mathcal{L}}\sigma = e^{-\tau\mathcal{L}}\rho$ is not positive semi-definite – this is a contradiction since $e^{t\mathcal{L}}$ is a CPTP map for all $t > 0$.

□

Lemma 4. *$\exp(t\mathcal{L})(\rho) > 0$ for all positive-definite density matrices $\rho \in S$ and $t > 0$*

This lemma appears to be quite similar to the previous lemma. The previous lemma showed that, given an operator \mathcal{L} generated from an irreducible matrix, that \mathcal{L} maps every density matrix in S to a positive-definite density matrix in S . By contrast, this lemma shows that even if \mathcal{L} is not generated from an irreducible matrix, that it still maps positive definite matrices in S to other positive definite matrices in S .

Proof. The proof for this lemma is almost identical to that above, except we can't

assume the strict inequalities used; in fact we need only deal with the case where equality occurs in place of the inequality previously. For the sake of brevity I will implicitly refer to the previous proof.

Case I:

By assumption $(\mathcal{L}\rho)_{mm} = 0$ for all $m \in J$ (otherwise it reduces to the case in the previous proof). This implies $\gamma_{mn} = 0$ for every $m \in J$ and $n \in I - J$; by induction this further means that $(\mathcal{L}^k \rho)_{mm} = 0$ for every $k \in \mathbb{N}$ and $m \in J$, and so for all $t \in \mathbb{R}^+$,

$$e^{-t\mathcal{L}}\rho \leq 0.$$

Case II:

We now have $\zeta_1 = \zeta_2 = 0$ and so $\gamma_{1i} = \gamma_{2i} = 0$ for $i \in I$. Then it can easily be checked that, under the action of $e^{-t\mathcal{L}}$,

$$\begin{bmatrix} \rho_{11} & \rho_{12} \\ \rho_{21} & \rho_{22} \end{bmatrix} \rightarrow \begin{bmatrix} e^{-\omega_{11}t}\rho_{11} & e^{-\omega_{12}t}\rho_{12} \\ e^{-\omega_{21}t}\rho_{21} & e^{-\omega_{22}t}\rho_{22} \end{bmatrix},$$

$$\therefore \det(e^{-t\mathcal{L}}\rho|_2) = e^{-2\omega_{12}t}\det(\rho) = 0$$

where we have used $\omega_{12} = \omega_{21} = \frac{1}{2}(\omega_{11} + \omega_{22})$. □

It does seem to me that the above two lemmas should hold more generally – that is hold for all density matrices rather than just those lying in S – but unfortunately I have been unable to show this; it is not of too much concern since the restricted

versions will suffice for what I want to show. We are now ready to apply these results to show that a three level engine – whether it be continuous, 2-stroke or 4-stroke – with hot and cold baths coupling two of the possible transitions and a unitary interaction coupling the third, will always settle into a stationary state/limit cycle, irrespective of its initial state.

The rough idea is as follows: suppose that Λ satisfies the properties in *lemma 2*; then we can decompose the space as $\mathcal{M}_d(\mathbb{C}) = R \oplus S$ and block diagonalise Λ as $\Lambda_R \oplus \Lambda_S$ accordingly, where,

$$R = \{M \in \mathcal{M}_d(\mathbb{C}) \mid M_{12} = M_{21} = 0 \text{ \& } M_{ii} = 0 \text{ for } i = 1, \dots, d\}.$$

Further suppose that, $\lim_{n \rightarrow \infty} (\Lambda_R)^n R = 0$, then given any density matrix $\rho = \rho_S + \sigma_R$, then,

$$\lim_{n \rightarrow \infty} \Lambda^n \rho = \lim_{n \rightarrow \infty} ((\Lambda_S)^n \rho_S + (\Lambda_R)^n \sigma_R) = \rho_\infty.$$

The Lindblad operators associated with the hot reservoir are $\{\sqrt{\gamma_{13}} |1\rangle \langle 3|, \sqrt{\gamma_{31}} |3\rangle \langle 1|\}$, whilst those for the cold reservoir are $\{\sqrt{\gamma_{23}} |2\rangle \langle 3|, \sqrt{\gamma_{32}} |3\rangle \langle 2|\}$. Here $\gamma_{31}/\gamma_{13} = \exp(-\Delta E_h/kT_h)$ and $\gamma_{32}/\gamma_{23} = \exp(-\Delta E_c/kT_c)$. The interaction Hamiltonian couples levels 1 and 2, at Rabi frequency Ω and detuning δ .

Theorem 5. *A continuous engine, with couplings to hot and cold reservoirs and interaction Hamiltonian as described above, relaxes to a steady state regardless of starting state.*

Proof. It is clear that the union of the thermal Lindblad operators results in a matrix γ which is irreducible. The result then follows from *corollary 1*. \square

Theorem 6. *A 2-stroke engine, with couplings as above, relaxes to a limit cycle regardless of starting state.*

Proof. Note that

$$e^{t\mathcal{L}}S \subseteq S \quad \text{and} \quad e^{i\mathcal{H}t}S \subseteq S.$$

Then by *lemma 3* we have $\exp(t\mathcal{L})(\rho) > 0$ for all density matrices $\rho \in S$ and $t > 0$; finally by *lemma 2*, there exists a positive definite density matrix $\rho_\infty \in S$ such that for every density matrix $\rho_S \in S$,

$$\lim_{n \rightarrow \infty} (e^{t\mathcal{L}}e^{i\mathcal{H}t})^n(\rho_S) = \rho_\infty.$$

The only thing that remains for us to show is that

$$\lim_{n \rightarrow \infty} (e^{t\mathcal{L}}e^{i\mathcal{H}t})^n(R) = \{0\}.$$

The respective restrictions of \mathcal{L} and \mathcal{H} to R , in the basis $\{\sigma_{13}, \sigma_{23}, \sigma_{31}, \sigma_{32}\}$, are,

$$\mathcal{L}_R = \begin{bmatrix} \omega_{13} & & & \\ & \omega_{23} & & \\ & & \omega_{13} & \\ & & & \omega_{23} \end{bmatrix} \quad \& \quad \mathcal{H}_R = \begin{bmatrix} 0 & \Omega & & \\ \Omega & 0 & & \\ & & 0 & -\Omega \\ & & -\Omega & 0 \end{bmatrix}$$

Calculating the eigenvalues of $e^{t\mathcal{L}_R}e^{i\mathcal{H}_R t}$, we find them to be bounded by $e^{\omega t} < 1$, where $\omega = \max(\omega_{13}, \omega_{23})$. Therefore,

$$\lim_{n \rightarrow \infty} (e^{t\mathcal{L}_R}e^{i\mathcal{H}_R t})^n = 0_{4 \times 4}$$

□

The four stroke engine provides a more interesting case. We can't prove the case in general – in fact we can easily find a counter example. Take $\gamma_{13} = \gamma_{31} = \gamma_{23} = \gamma_{32} = 1$; further take the limit of complete thermalisation ($t_{th} \rightarrow \infty$) and $\Omega t_{coh} = \pi$. Then

$$e^{i\mathcal{H}_{St_{coh}}} e^{\mathcal{L}_S^c t_{th}} e^{i\mathcal{H}_{St_{coh}}} e^{\mathcal{L}_S^h t_{th}} = \begin{bmatrix} 0 & & & \\ & 0 & & \\ & & 0.5 & 0 & 0.5 \\ & & 0 & 1 & 0 \\ & & 0.5 & 0 & 0.5 \end{bmatrix}$$

This has 2 distinct density matrices with eigenvalue one: $[0, 0, 0, 1, 0]^T$ and $[0, 0, \frac{1}{2}, 0, \frac{1}{2}]^T$. We will see that this rests on the unitary being a π pulse. Under the reasonable assumption that the unitary does not completely swap the populations (either taking $\Omega t_{coh} < \pi$ or simply if there is any detuning).

Theorem 7. *Suppose either $t_1, t_2 < \pi/\Omega$ or $\delta \neq 0$. Then $\Lambda = e^{i\mathcal{H}_{St_1}} e^{\mathcal{L}_S^c t_2} e^{i\mathcal{H}_{St_3}} e^{\mathcal{L}_S^h t_4}$ is relaxing.*

Proof. We first show that $\Lambda\rho > 0$ for all density matrices $\rho \in S$:

Let $\rho \in S$. If the starting state is positive definite then we are done. Otherwise we consider what density matrices $e^{\mathcal{L}_S^h t}$ is able to map to density matrices with non-trivial kernel (in a similar manner to the proof for *lemma 3*). It can be established that the only two forms can be:

$$[0, 0, \rho_{11}, 0, \rho_{33}]^T \quad \text{and} \quad [0, 0, 0, 1, 0]^T.$$

We proceed by considering these two cases. First, suppose our starting state, $\rho^{(0)}$, is the first of the two. Then under the action of $e^{\mathcal{L}_S^h t}$, followed by that of the unitary,

U_1 , we have,

$$\rho^{(0)} \xrightarrow{h} \left[0, 0, \rho_{11}^{(1)}, 0, \rho_{33}^{(1)}\right]^T \xrightarrow{U_1} \left[\rho_{12}^{(2)}, \rho_{21}^{(2)}, \rho_{11}^{(2)}, \rho_{22}^{(2)}, \rho_{33}^{(1)}\right]^T,$$

where $\rho_{11}^{(1)}$ & $\rho_{33}^{(1)} > 0$ and therefore $\rho_{11}^{(2)} > 0$ by assumption. Note that the corresponding states for $e^{\mathcal{L}_S^c t}$ are $[0, 0, 0, \rho_{22}, \rho_{33}]^T$ and $[0, 0, 1, 0, 0]^T$. Since $\rho^{(2)}$ doesn't correspond to either of these, the result of the full sequence on $\rho^{(0)}$ is positive definite. Now consider the second of the two initial states,

$$\rho^{(0)} \xrightarrow{h} [0, 0, 0, 1, 0]^T \xrightarrow{U_1} \left[\rho_{12}^{(2)}, \rho_{21}^{(2)}, \rho_{11}^{(2)}, \rho_{22}^{(2)}, 0\right]^T,$$

where, again by the assumption on the unitary, $\rho_{22}^{(2)} > 0$. Then under the action of $e^{\mathcal{L}_S^c t}$ and U_2 ,

$$\rho^{(2)} \xrightarrow{c} \left[\rho_{12}^{(3)}, \rho_{21}^{(3)}, \rho_{11}^{(3)}, \rho_{22}^{(3)}, \rho_{33}^{(3)}\right]^T \xrightarrow{U_2} \left[\rho_{12}^{(4)}, \rho_{21}^{(4)}, \rho_{11}^{(4)}, \rho_{22}^{(4)}, \rho_{33}^{(3)}\right]^T,$$

where $\rho_{22}^{(4)}$ & $\rho_{33}^{(3)} > 0$. This doesn't correspond to either of the two possible initial states, so the application of two full sets of the sequence will result in a positive definite matrix (i.e $n = 2$ in *theorem 4*).

Finally it can be shown that $\lim_{n \rightarrow \infty} (\Lambda_R)^n = 0_{4 \times 4}$, much as in the *theorem 6*. \square

From this section we can conclude that a quantum heat engine will settle down to a unique steady state operating cycle (post transient), irrespective of the details of the work stroke (including parameters such as detuning), and irrespective of the engine type.

Chapter 6

Conclusion

This thesis has been concerned with examining quantum coherent effects in the operation of microscopic heat engines. To this end I first described how a heat engine could be implemented using NV-centres in diamond. Following this, the extensions to the theory, first presented in [27], required to account for experimental conditions found in NV centres in the diamond sample were derived. The principal work conducted for this thesis was the building and running of the experimental setup in order to test for the existence of the quantum thermodynamic signature and heat engine equivalence. In the remainder of this section I give a brief summary of the contents of this thesis, and then discuss some possible future directions that might be made beyond the results that have been presented.

6.1 Summary

To summarise, this thesis can be divided into three parts. First in chapter 2, some of the prerequisite background material for quantum thermodynamics, and more specifically the dynamical description of quantum heat engines, as well as the negative NV-centre are described. In chapter 3, I use the material in chapter 2 to show how

a heat engine can be implemented using the NV centre; this includes showing how the thermal action can be emulated, how the power can be determined by measuring fluorescence change, how the experiment was constructed, and how the data was collected. Chapter 4 describes both theoretical and experimental results obtained during this thesis. The theoretical results involve extending the theory originally derived in the paper by Uzdin et al [27], including effects such as dephasing and inhomogeneous broadening, including the emulated thermal action, and the numerics to predict the power output. They also include results on the limit cycles of quantum heat engines, showing that both the continuous and two-stroke engines always converge to a limit point. Finally, in the second part of chapter 4, the experimental results are presented. The two major experimental results, both of which manifest themselves in the small action regime, were the demonstration of the equivalence between the continuous and two-stroke engines, and the measurement of power outputs from the two-stroke engine which exceed the stochastic bound and constitutes a quantum thermodynamic measurement. To the best of my knowledge this is the first demonstration of such quantum effects within the operation of microscopic heat engines when operating between thermal baths.

6.2 Outlook

Experimental quantum thermodynamics is still very much in its infancy, as to a certain extent, is the field itself. One of the open problems remains to determine whether there are features of quantum thermodynamics which are distinctly quantum and interesting. This thesis has demonstrated that thermodynamic engines can indeed behave differently to their corresponding classical engines when operating in the quantum regime; however, this behaviour only manifests itself in a very specific para-

meter range (the small action regime), where quantum coherence is able to provide a very marginal advantage. A great deal more work remains to be done on the subject of quantum heat engines, both theoretically and experimentally. In particular, there should be more work done to search for different quantum thermodynamic signatures in heat engines; or more generally, ways in which quantum effects, different than those shown in this thesis, may be used to provide a thermodynamic advantage.

First we consider what could be done to improve upon and extend this experiment with relatively little modification to the current setup. To begin with, a substantial improvement in the results presented in this thesis could be obtained by simply replacing the diamond sample with a new sample which has lower inhomogeneous broadening (lower strain and lower density) and is thinner – the lower broadening should increase the power output per NV-centre, whilst the thinner sample should allow for us to be able to focus near the micro-strip line (where the field is more homogeneous) without losing too much light through absorption in the diamond. Taking this even further would be to potentially go down to a single centre experiment; this is commonplace in the NV community, although it will obviously be made more difficult by working in the small action regime – placing the centre in an optical cavity could perhaps be used to enhance the coupling strengths and collection efficiencies. Such a cavity need not have an exceptionally high Q-factor, so a first attempt might be fabricated by simply constructing it out of the diamond itself – two of the sides might simply be polished, and mirrors attached to these facets to form a rudimentary cavity. There have also been numerous efforts to increase the collection efficiency from single NV centres for magnetometry purposes using structures carved into the surface such as solid immersion lenses, bullseye gratings and nanopillars [70, 71, 44].

More work can also be done to more thoroughly investigate the role of decoherence in the inhomogeneously broadened sample. This will require a more involved theoretical

investigation, as well as a better experimental efforts than we were able to do up to this point; despite giving it a good deal of thought, we were unable to think of a better way of measuring the effect of decoherence on the power output. Ideally this would require some means of controlably introducing decoherence in the engine without affecting the lifetime (T_1), potentially through introducing noise at the driving resonance frequency.

Going beyond this experiment, there is the potential to use the NV setup to test for quantum thermal signatures in heat machines based on other quantum agents, such as entanglement and quantum discord. There have been theoretical results relating to entanglement, indicating that it can be used to increase the amount of extractable work from a collection of two-level batteries; more specifically, the work that can be extracted from N two-level systems can be maximised if the initial state is entangled [77]. It has also been predicted that being able to perform global unitary operations on an ensemble of N qubits allows for a N -fold increase in charging power per qubit [21]. There have also been several experiments demonstrating entanglement between individual NV-centres [78]. Therefore an ensemble of NV centres might make an appropriate system in which to test there claims. This would require quite a lot more work, as we would have to figure out a means of performing the genral N -dimensional unitary operations ($U(N)$) required for these experiments, which would also constitute a full N -qubit quantum computer.

Bibliography

- [1] T. D. Ladd, F. Jelezko, R. Laflamme, Y. Nakamura, C. Monroe, and J. L. O’Brien. Quantum computers. *Nature*, 464:45 EP –, 03 2010.
- [2] C. H. Bennett and G. Brassard. Quantum cryptography: Public-key distribution and coin tossing. Proceedings of IEEE International Conference on Computers, Systems and Signal Processing, 1985.
- [3] Vittorio Giovannetti, Seth Lloyd, and Lorenzo Maccone. Advances in quantum metrology. *Nature Photonics*, 5:222 EP –, 03 2011.
- [4] I. M. Georgescu, S. Ashhab, and Franco Nori. Quantum simulation. *Rev. Mod. Phys.*, 86:153–185, Mar 2014.
- [5] R. Alicki and R. Kosloff. Introduction to quantum thermodynamics: History and prospects. *ArXiv*, 2018.
- [6] S. Vinjanampathy and J. Anders. Quantum thermodynamics. *Contemporary Physics*, 57, 2015.
- [7] J. Zou, Z. Marcet, A. W. Rodriguez, M. T. H. Reid, A. P. McCauley, I. I. Kravchenko, T. Lu, Y. Bao, S. G. Johnson, and H. B. Chan. Casimir forces on a silicon micromechanical chip. *Nature Communications*, 4:1845 EP –, 05 2013.

-
- [8] Wenqi Zhu, Ruben Esteban, Andrei G. Borisov, Jeremy J. Baumberg, Peter Nordlander, Henri J. Lezec, Javier Aizpurua, and Kenneth B. Crozier. Quantum mechanical effects in plasmonic structures with subnanometre gaps. *Nature Communications*, 7:11495 EP –, 06 2016.
- [9] Richard P Feynman. There’s plenty of room at the bottom. engineering and science. *Caltech Magazine*, 23(5):22–36, 1960.
- [10] H. E. D. Scovil and E. O. Schulz-DuBois. Three-level masers as heat engines. *Phys. Rev. Lett.*, 2:262–263, Mar 1959.
- [11] J Robnagel, S Dawkins, K Tolazzi, O Abah, E Lutz, F Schmidt-Kaler, and K Singer. A single-atom heat engine. *Science*, 352(6283):325–329, 2016.
- [12] Keye Zhang, Francesco Bariani, and Pierre Meystre. Quantum optomechanical heat engine. *Physical review letters*, 112(15):150602, 2014.
- [13] David Gelbwaser-Klimovsky and Gershon Kurizki. Work extraction from heat-powered quantized optomechanical setups. *Scientific reports*, 5, 2015.
- [14] Michele Campisi, Jukka Pekola, and Rosario Fazio. Nonequilibrium fluctuations in quantum heat engines: theory, example, and possible solid state experiments. *New Journal of Physics*, 17(3):035012, 2015.
- [15] A. O. Niskanen, Y. Nakamura, and J. P. Pekola. Information entropic superconducting microcooler. *Physical review B*, 76(174523), 2007.
- [16] Valentin Blickle and Clemens Bechinger. Realisation of a micrometre-sized stochastic heat engine. *Nature Physics*, 8:143–146, 2011.
- [17] Frederick Reif. *Fundamentals of Statistical and Thermal Physics*. MacGraw-Hill International Editions, 1965.

-
- [18] T. Feldmann and R. Kosloff. Quantum four-stroke heat engine: Thermodynamic observables in a model with intrinsic friction. *Physical Review E*, 68, 2003.
 - [19] R. Kosloff and T. Feldmann. Discrete four-stroke quantum engine exploring the origin of friction. *Physical Review E*, 65, 2002.
 - [20] Y. Rezek and R. Kosloff. Irreversible performance of a quantum harmonic heat engine. *New Journal of Physics*, 8, 2006.
 - [21] Felix C Binder, Sai Vinjanampathy, Kavan Modi, and John Goold. Quantacell: powerful charging of quantum batteries. *New Journal of Physics*, 17(7):075015, 2015.
 - [22] Obinna Abah and Eric Lutz. Efficiency of heat engines coupled to nonequilibrium reservoirs. *EPL (Europhysics Letters)*, 106(2):20001, 2014.
 - [23] J. RoBnagel, O. Abah, F. Schmidt-Kaler, K. Singer, and E. Lutz. Nanoscale heat engine beyond the carnot limit. *Phys. Rev. Lett.*, 112:030602, Jan 2014.
 - [24] Jan Klaers, Stefan Faelt, Atac Imamoglu, and Emre Togan. Squeezed thermal reservoirs as a resource for a nanomechanical engine beyond the carnot limit. *Phys. Rev. X*, 7:031044, Sep 2017.
 - [25] Gonzalo Manzano, Fernando Galve, Roberta Zambrini, and Juan M. R. Parrondo. Entropy production and thermodynamic power of the squeezed thermal reservoir. *Phys. Rev. E*, 93:052120, May 2016.
 - [26] Marlan O. Scully, M. Suhail Zubairy, Girish S. Agarwal, and Herbert Walther. Extracting work from a single heat bath via vanishing quantum coherence. *Science*, 299(5608):862–864, 2003.

-
- [27] Raam Uzdin, Amikam Levy, and Ronnie Kosloff. Equivalence of quantum heat machines, and quantum-thermodynamic signatures. *Physical review X*, 5(031044), 2015.
- [28] R. Kosloff. Quantum thermodynamics: A dynamical viewpoint. *Entropy*, 15:2100–2128, 2013.
- [29] Patrick P Hofer, Mart Perarnau-Llobet, L David M Miranda, Graldine Haack, Ralph Silva, Jonatan Bohr Brask, and Nicolas Brunner. Markovian master equations for quantum thermal machines: local versus global approach. *New Journal of Physics*, 19(12):123037, 2017.
- [30] R. Kosloff and Y. Rezek. The quantum harmonic otto cycle. *Entropy*, 19, 2017.
- [31] R. Alicki. The quantum open system as a model of the heat engine. *J Phys A: Math*, 12(5), 1979.
- [32] M. A. Nielsen and I. L. Chuang. *Quantum Computation and Quantum Information*. Cambridge University Press, Cambridge, 2000.
- [33] G. Lindblad. On the generators of quantum dynamical semigroups. *Communications in Mathematical Physics*, 48(2):119–130, 1976.
- [34] Vittorio Gorini, Andrzej Kossakowski, and E. C. G. Sudarshan. Completely positive dynamical semigroups of n -level systems. *Journal of Mathematical Physics*, 17(5):821–825, 1976.
- [35] E.B. Davies. Markovian master equations. *Commun Math Phys*, 39:91–110, 1974.
- [36] A. Levey and R. Kosloff. On the local and global approaches to quantum transport and violation of the second law of thermodynamics. *Europhysics letters*, 107(2), 2014.

-
- [37] Angel Rivas, A Douglas K Plato, Susana F Huelga, and Martin B Plenio. Markovian master equations: a critical study. *New Journal of Physics*, 12(11):113032, 2010.
- [38] R. Kosloff. Quantum heat engines and refrigerators: Continuous devices. *Review of Physical Chemistry*, 65:365–393, 2014.
- [39] M. J. Henrich, F. Rempp, and G. Mahlerk. Quantum thermodynamic otto machines: A spin-system approach. *The European Physical Journal, Special edition*, 151:157–165, 2007.
- [40] F.L. Curzon and B. Ahlborn. Efficiency of a carnot engine at maximum power output. *American Journal of Physics*, 43, 1975.
- [41] T. Jahnke and C. Lubich. Error bounds for exponential operator splittings. *BIT Numerical Mathematics*, 40(4):735–744, 2000.
- [42] V. M. Acosta, A. Jarmola, E. Bauch, and D. Budker. Optical properties of the nitrogen-vacancy singlet levels in diamond. *Physical review B*, 82(201202), 2010.
- [43]
- [44] L Rondin, J-P Tetienne, T Hingant, J-F Roch, P Maletinsky, and V Jacques. Magnetometry with nitrogen-vacancy defects in diamond. *Reports on Progress in Physics*, 77(5):056503, 2014.
- [45] Junfeng Wang, Fupan Feng, Jian Zhang, Jihong Chen, Zhongcheng Zheng, Liping Guo, Wenlong Zhang, Xuerui Song, Guoping Guo, Lele Fan, Chongwen Zou, Liren Lou, Wei Zhu, and Guanzhong Wang. High-sensitivity temperature sensing using an implanted single nitrogen-vacancy center array in diamond. *Phys. Rev. B*, 91:155404, Apr 2015.

-
- [46] P. Neumann, I. Jakobi, F. Dolde, C. Burk, R. Reuter, G. Waldherr, J. Honert, T. Wolf, A. Brunner, J. H. Shim, D. Suter, H. Sumiya, J. Isoya, and J. Wrachtrup. High-precision nanoscale temperature sensing using single defects in diamond. *Nano Letters*, 13(6):2738–2742, 2013. PMID: 23721106.
- [47] Rinat Akhmedzhanov, Lev Gushchin, Nikolay Nizov, Vladimir Nizov, Dmitry Sobgayda, Ilya Zelensky, and Philip Hemmer. Microwave-free magnetometry based on cross-relaxation resonances in diamond nitrogen-vacancy centers. *Phys. Rev. A*, 96:013806, Jul 2017.
- [48] L. M. Pham, N. Bar-Gill, D. Le Sage, C. Belthangady, A. Stacey, M. Markham, D. J. Twitchen, M. D. Lukin, and R. L. Walsworth. Enhanced metrology using preferential orientation of nitrogen-vacancy centers in diamond. *Phys. Rev. B*, 86:121202, Sep 2012.
- [49] M.W. Doherty, N.B. Manson, P. Delaney, F. Jelezko, J. Wrachtrup, and L.C.L. Hollenberg. The nitrogen-vacancy colour centre in diamond. *Physics Reports*, 528:1–45, 2013.
- [50] P.L. Stanwix, L.M. Pham, J.R. Maze, D. Le Sage, T.K. Yeung, P. Cappellaro, P.R. Hemmer, A. Yacoby, M.D. Lukin, and R.L. Walsworth. Coherence of nitrogen-vacancy electronic spin ensembles in diamond. *Physical review B*, 82, 2010.
- [51] N. Bar-Gill, L.M. Pham, A. Jarmola, D. Budker, and R.L. Walsworth. Solid-state electronic spin coherence time approaching one second. *Nature Communications*, 4, 2013.

-
- [52] D. A. Redman, S. Brown, R. H. Sands, and S. C. Rand. Spin dynamics and electronic states of n-v centers in diamond by epr and four-wave-mixing spectroscopy. *Phys. Rev. Lett.*, 67:3420–3423, Dec 1991.
- [53] M.L. Goldman, M.W. Doherty, A. Sipahigil, N.Y. Yao, S.D. Bennett, N.B. Manson, A. Kubanek, and M.D. Lukin. State-selective intersystem crossing in nitrogen-vacancy centers. *Physical review B*, 91(165201), 2015.
- [54] Steven H. Simon. *The Oxford Solid State Basics*. Oxford University Press, 2013.
- [55] J. R. Maze, A. Gali, E. Togan, Y. Chu, A. Trifonov, E. Kaxiras, and M. D. Lukin. Properties of nitrogen-vacancy centers in diamond: the group theoretic approach. *New Journal of Physics*, 13(025025), 2011.
- [56] M.W. Doherty, N.B. Manson, P. Delaney, and L.C.L. Hollenberg. The negatively charged nitrogen-vacancy centre in diamond: the electronic solution. *New Journal of Physics*, 13(025019), 2011.
- [57] L.J. Rogers, R.L. McMurtrie, M.J. Sellars, and N.B. Manson. Time-averaging within the excited state of the nitrogen-vacancy centre in diamond. *New Journal of Physics*, 11(063007), 2009.
- [58] R. J. Epstein, F. M. Mendoza, Y. K. Kato, and D. D. Awschalom. Anisotropic interactions of a single spin and dark-spin spectroscopy in diamond. *Nature Physics*, 1:94 EP –, 2005.
- [59] L J Rogers, R L McMurtrie, M J Sellars, and N B Manson. Time-averaging within the excited state of the nitrogen-vacancy centre in diamond. *New Journal of Physics*, 11(6):063007, 2009.

-
- [60] J.P. Tetienne, R. W. de Gille, D. A. Broadway, T. Teraji, S. E. Lillie, J. M. McCoe, N. Donschuk, L. T. Hall, A. Stacey, D. A. Simpson, and L. C. L. Hollenberg. Spin properties of dense near-surface ensembles of nitrogen-vacancy centers in diamond. *Physical review B*, 97(085402), 2018.
- [61] T. van der Sar L. Robledo, H. Bernien and R. Hanson. Spin dynamics in the optical cycle of single nitrogen-vacancy centres in diamond. *New Journal of Physics*, 13(025025), 2010.
- [62] J.P. Tetienne, L. Rondin, P. Spinicelli, M. Chipaux, T. Debuisschert, J.F. Roch, and V. Jacques. Magnetic-field-dependent photodynamics of single nv defects in diamond: an application to qualitative all-optical magnetic imaging. *New Journal of Physics*, 14(103033), 2012.
- [63] Susumu Takahashi, Ronald Hanson, Johan van Tol, Mark S. Sherwin, and David D. Awschalom. Quenching spin decoherence in diamond through spin bath polarization. *Phys. Rev. Lett.*, 101:047601, Jul 2008.
- [64] T. A. Kennedy, J. S. Colton, J. E. Butler, R. C. Linares, and P. J. Doering. Long coherence times at 300 k for nitrogen-vacancy center spins in diamond grown by chemical vapor deposition. *Applied Physics Letters*, 83(20):4190–4192, 2003.
- [65] T. A. Kennedy, F. Charnock, J. S. Colton, J. E. Butler, R. C. Linares, and P. J. Doering. Single-qubit operations with the nitrogen-vacancy center in diamond. *phys. stat. sol.*, 233:416–426, 2002.
- [66] F. Jelezko, T. Gaebel, I. Popa, M. Domhan, A. Gruber, and J. Wrachtrup. Observation of coherent oscillation of a single nuclear spin and realization of a two-qubit conditional quantum gate. *Phys. Rev. Lett.*, 93:130501, Sep 2004.

-
- [67] F. Jelezko, T. Gaebel, I. Popa, A. Gruber, and J. Wrachtrup. Observation of coherent oscillations in a single electron spin. *Phys. Rev. Lett.*, 92:076401, Feb 2004.
- [68] Gopalakrishnan Balasubramanian, Philipp Neumann, Daniel Twitchen, Matthew Markham, Roman Kolesov, Norikazu Mizuochi, Junichi Isoya, Jocelyn Achard, Johannes Beck, Julia Tissler, Vincent Jacques, Philip R. Hemmer, Fedor Jelezko, and Jörg Wrachtrup. Ultralong spin coherence time in isotopically engineered diamond. *Nature Materials*, 8:383 EP –, 04 2009.
- [69] Eric van Oort and Max Glasbeek. Cross-relaxation dynamics of optically excited n-v centers in diamond. *Phys. Rev. B*, 40:6509–6517, Oct 1989.
- [70] Rishi N Patel, Tim Schröder, Noel Wan, Luozhou Li, Sara L Mouradian, Edward H Chen, and Dirk R Englund. Efficient photon coupling from a diamond nitrogen vacancy center by integration with silica fiber. *Light: Science & Applications*, 5:e16032 EP –, 02 2016.
- [71] Luozhou Li, Edward H. Chen, Jiabao Zheng, Sara L. Mouradian, Florian Dolde, Tim Schrder, Sinan Karaveli, Matthew L. Markham, Daniel J. Twitchen, and Dirk Englund. Efficient photon collection from a nitrogen vacancy center in a circular bullseye grating. *Nano Letters*, 15(3):1493–1497, 2015. PMID: 25714414.
- [72] David M. Pozar. *Microwave Engineering*. John Wiley and Sons Inc, 1998.
- [73] R.J.P. Douville and D.S. James. Experimental study of symmetric microstrip bends and their compensation. *IEEE Transactions on Microwave Theory and Techniques*, 26:175–182, 1978.

-
- [74] J. M. Taylor, P. Cappellaro, L. Childress, L. Jiang, D. Budker, P. R. Hemmer, A. Yacoby, R. Walsworth, and M. D. Lukin. High-sensitivity diamond magnetometer with nanoscale resolution. *Nature*, 4:810 – 816, 2008.
- [75] Herbert Spohn. An algebraic condition for the approach to equilibrium of an open n-level system. *Letters in Mathematical Physics*, 2:33–38, 1977.
- [76] Roger A. Horn and Charles R. Johnson. *Matrix Analysis*. Cambridge University Press, 2012.
- [77] Robert Alicki and Mark Fannes. Entanglement boost for extractable work from ensembles of quantum batteries. *Phys. Rev. E*, 87:042123, Apr 2013.
- [78] H. Bernien, B. Hensen, W. Pfaff, G. Koolstra, M. S. Blok, L. Robledo, T. H. Taminiau, M. Markham, D. J. Twitchen, L. Childress, and R. Hanson. Heralded entanglement between solid-state qubits separated by three metres. *Nature*, 497:86 EP –, 04 2013.